NOTE TO USERS

Radar Observations of Orographic Precipitation

Curtis Neal James

A dissertation submitted in partial fulfillment
of the requirements for the degree of

Doctor of Philosophy

University of Washington

2004

Program Authorized to Offer Degree:
Department of Atmospheric Sciences

INFORMATION TO USERS

The quality of this reproduction is dependent upon the quality of the copy submitted. Broken or indistinct print, colored or poor quality illustrations and photographs, print bleed-through, substandard margins, and improper alignment can adversely affect reproduction.

In the unlikely event that the author did not send a complete manuscript and there are missing pages, these will be noted. Also, if unauthorized copyright material had to be removed, a note will indicate the deletion.

ProQuest Information and Learning Company
300 North Zeeb Road
P.O. Box 1346
Ann Arbor, MI 48106-1346

University of Washington
Graduate School

This is to certify that I have examined this copy of a doctoral dissertation by

Curtis Neal James

and have found that it is complete and satisfactory in all respects,
and that any and all revisions required by the final
examining committee have been made.

Chair of Supervisory Committee:

Robert A. Houze, Jr.

Robert A. Houze, Jr.

Reading Committee:

Robert A. Houze, Jr.

Robert A. Houze, Jr.

Clifford F. Mass

Sandra E. Yuter

Date: 21 May 2004

In presenting this dissertation in partial fulfillment of the requirements for the doctoral degree at the University of Washington, I agree that the Library shall make its copies freely available for inspection. I further agree that extensive copying of the dissertation is allowable only for scholarly purposes, consistent with "fair use" as prescribed in the U.S. Copyright Law. Requests for copying or reproduction of this dissertation may be referred to Proquest Information and Learning, 300 North Zeeb Road, Ann Arbor, MI 48106-1346, to whom the author has granted "the right to reproduce and sell (a) copies of the manuscript in microform and/or (b) printed copies of the manuscript made from microform."

Signature Curtis Neal Jones

Date 21 May 2004

University of Washington

Abstract

Radar Observations of Orographic Precipitation

Curtis Neal James

Chair of the Supervisory Committee:
Professor Robert A. Houze, Jr.
Department of Atmospheric Sciences

Operational Doppler radar archives provide insight into the structure and airflow within precipitating systems in two different mountain climates: the Mediterranean side of the European Alps and the coastal terrain of Northern California. Time-averaged reflectivity measurements reveal that climatological precipitation in both locations is the result of broad-scale upslope enhancement, upstream enhancement, and small-scale enhancement of precipitation. Within approximately a Rossby radius of each barrier's crest, precipitation amounts were greater than farther upstream. Over the broad windward slopes of each barrier, precipitation amounts were further enhanced and maximum over the first steep terrain rise of both ranges.

Time-averaged radial velocity measurements during precipitation events revealed prevailing low-level flow that was perpendicular to the axis of each barrier and veered with height, indicating the presence of warm advection. Variations in the thermodynamic and dynamic properties of the impinging large-scale flow modulated the flow patterns and resulting rainfall. Precipitation was greatest when

the direction of the impinging low-level flow (900 – 800 mb) brought copious low-level moisture and was perpendicular to the windward slopes. In the Alps, strong high Froude-number flow produced the greatest upslope enhancement over the lower windward slopes. In California, where high Froude-number flow was the norm, more rainfall occurred on the windward slopes and upstream when the flow was more stable. Likely in response to diurnal stability and humidity fluctuations, rainfall was more pronounced in the morning hours in both locations. Stronger, more humid airflow at mid levels (700 – 500 mb) also produced dramatically heavier precipitation over California.

To facilitate this work, various software tools were developed to correct, process and display radar data, laying the groundwork for real-time radar data analysis during MAP. Techniques were configured for converting, interpolating, and finally displaying the radar data over terrain. In addition, a skillful yet efficient algorithm was designed to correct aliased Doppler velocity patterns over complex terrain.

TABLE OF CONTENTS

LIST OF FIGURES

LIST OF TABLES

ACKNOWLEDGMENTS

The author expresses sincere gratitude to Professor Robert A. Houze, Jr., for his scientific insight and careful readings of this dissertation and other manuscripts. His patient and flexible mentoring style have allowed me to adapt to extenuating life circumstances.

Thanks are extended to Professors Cliff Mass and Sandra Yuter for serving on the reading committee and Supervisory Committee; and to Dale Durran, for his kind mentorship and membership on the committee. Peter Hobbs, James Riley, and Robert Edmonds also served on the supervisory committee at certain times.

Mel Nordquist (NWS) and Gianmario Galli (SMA) spent countless hours compiling the immense radar data archives used in this study. Others who contributed data, figures, and/or technical expertise include: Stacy Brodzik, Harry Edmon, Socorro Medina, Brian Colle, Mark Sinclair, Jürg Joss, Urs Germann, Ernie Recker, Ken Westrick, Zhaoxia Zeng, Peter Binder, Christoph Frei, Paul Neiman, Brad Colman, Chris Hill, and Dennis Hartman. Kathryn Stout and Tülay Bayburt provided invaluable administrative assistance. Candace Gudmundson skillfully edited much of this dissertation manuscript, while Kate Dewar and Jill Campbell prepared figures.

I especially appreciate my parents, Mary and Floyd James, for their love and undying support; and my three children, Vincent, Daniela, and Kevin, for their sacrifices to make this work possible.

DEDICATION

To my parents.

CHAPTER 1

INTRODUCTION

1.1 Orographic precipitation

1.1.1 Background

Since early last century, it has been thought that precipitation generally increases with topographic elevation (Henry 1919, Douglas and Glasspoole 1947, Longley 1975). This climatological terrain-height relationship is often referred to as the "orographic effect." Statistical studies of orographic precipitation have linearly regressed precipitation measurements with terrain elevation to produce climatological precipitation maps (Smith 1979). However, the regression slopes obtained by these studies are highly variable. Smith attributes this variability to factors such as prevailing wind speed and direction relative to the slope of the terrain, effects of surrounding terrain, climate of the region, and the thermodynamics and humidity of the flow.

The PRISM model (Daly et al. 1994) accounts for some of this variability by dividing digital topographical information into "facets" based on terrain orientation and calculating a linear regression slope between height and precipitation on each facet. Such regressions are applied at each facet to interpolate climatological precipitation to a Cartesian grid. However, the PRISM model constrains the regression slope on a given facet must be greater than or equal to zero, and therefore predicts local precipitation maxima over mountain peaks, regardless of their width or

height. Figure 1.1a contains the PRISM model analysis of annual precipitation over coastal Northern California for the period 1971 – 2000, with the underlying terrain in Figure 1.1b. A comparison of Figs. 1.1a and 1.1b indicates that the PRISM model captures broad-scale precipitation maxima over the windward slopes of the Coastal Range that are large enough to be resolved by existing rain-gauge networks. However, fine-scale precipitation amounts are forced by the PRISM model to increase with elevation. Of particular note is the circular rainfall pattern centered over Mount Shasta (just northeast of the town Mount Shasta), which extends to an altitude that is well above 3 km MSL and dominates the landscape of Northern California (Figs. 1.1a and 1.1b).

Frei and Schär (1998) incorporated a more sophisticated distance-weighting scheme (Shepard 1984), to create climatological precipitation maps for the European Alps. Using a very dense Alpine rain-gauge network, they found that precipitation was maximum over the steep north and south rims of the range, and less over the highest terrain (Fig. 1.2). This result was attributed to large-scale upslope lifting (Smith 1979) and the general decrease of absolute humidity with height in the atmosphere (Alpert 1986). Furthermore, Frei and Schär (1998) showed that climatological precipitation maxima were spatially connected with mesoscale indentations in the terrain (Fig. 1.3) and therefore could not be represented by simple elevation regressions.

The mapping techniques of Daly et al. (1994) and Frei and Schär (1998) are both based on rain-gauge data, and do not present the three-dimensional structure of precipitation in a highly resolved spatial pattern. Moreover, the statistical methodologies applied to the gauge data in the two studies lead to different conclusions regarding where the most precipitation occurs in mountains. Daly et al. (1994) suggest the maximum is at mountain top, while Frei and Schär (1998) indicate that the maximum is on the steep windward slopes, below the highest terrain.

1.1.2 Orographic precipitation mechanisms

The motivation for this dissertation is to examine orographic precipitation in greater detail and to improve scientific understanding of how precipitation is enhanced and spatially distributed by terrain. It is well known that terrain influences precipitation through a number of mechanisms (Smith 1979, Houze 1993). Upstream enhancement of precipitation can occur upwind of orography when the flow is at least partially blocked or the phase lines of vertically propagating mountain waves tilt upstream with height (e.g., Queney 1948; Durran 1990). Theory predicts that blocking occurs within a Rossby radius of the barrier crest when flow at low Froude numbers (i.e. less than unity) geostrophically adjusts to terrain-induced pressure perturbations[1]. Under these conditions, the airflow converges and lifts, enhancing rainfall. Deep convection may be triggered upstream from a barrier when the atmosphere is conditionally unstable (e.g., Grossman and Durran 1984).

Furthermore, turbulent updrafts associated with wind shear zones over blocked upstream flow can enhance hydrometeor growth (Houze and Medina 2004).

Upslope enhancement of upward air motion is caused by forced lifting over broad terrain. The magnitude and spatial distribution of this enhancement depends on factors such as the strength and direction of the flow, width and height of the terrain, static stability, and humidity (Smith 1979; Cotton and Anthes 1989). Upslope enhancement is typically maximum near the steepest windward slope where the strongest lifting occurs (Smith 1979; Houze 1993). However, the strength and direction of the impinging flow, barrier height, and vertical moisture distribution affect the intensity and spatial distribution of precipitation, as well as the extent of hydrometeor drift before precipitation reaches the ground (e.g., Hobbs et al. 1973; Sinclair et al. 1997; Ralph et al. 2003).

At smaller horizontal scales (e.g., on the order of a few kilometers), stable mountain-wave lifting and unstable convective influences may enhance hydrometeor growth. Factors that influence small-scale rainfall patterns in stable airflow are wind speed, the fall speeds and concentrations of various hydrometeor species, and the width and height of the mountain (Carruthers and Choularton 1983). Ample low-level moisture is required to achieve small-scale enhancement, although it is possible that too much humidity would reduce the moist Brunt-Väisälä frequency

[1] The Rossby radius and Froude number are defined as $L_R = NH/f$ and $F=U/HN$, respectively, where N is the Brunt-Väisälä frequency, H is the height of the barrier, and U is the speed scale of the wind.

and actually result in lower amplitude mountain waves and lessen the enhancement (Richard et al. 1987).

One example of small-scale enhancement of stratiform precipitation that has received wide attention in the literature is the seeder-feeder mechanism (Bergeron 1968), where stratiform precipitation is enhanced by accretion or vapor deposition inside low-altitude clouds that develop over small hills. The seeder-feeder mechanism favors dendritic snow formation when low-level air is previously moistened by precipitation (Choularton and Perry 1986; Hill and Browning 1979). Seeder-feeder enhancement is typically maximized near hillcrest, and depends on the precipitation rate of the seeder cloud and the accretion efficiency, condensation rate, depth, and water content of the feeder cloud (Bergeron 1968; Browning 1979; Cotton and Anthes 1989).

Convective enhancement or triggering in potentially unstable air is another important contributor to orographic rainfall, beginning at small spatial scales (e.g. Houze 1993). Mountain convection may range from shallow cells that produce mainly low-level liquid coalescence growth (e.g. White et al. 2003) to deep convective storms with intense precipitation rates (e.g. Caracena et al. 1979). Embedded convection may develop in potentially unstable airflow and strongly increase rainfall, especially over the first steep rise of the terrain (Medina and Houze 2003; Yuter and Houze 2003).

To the lee of large barriers, precipitation is typically suppressed by subsidence warming (Smith 1979; Mass and Ferber 1990). This effect, often referred to as rain shadowing, is most pronounced when the airflow is strong (Holmboe and Klieforth 1957). However, lee enhancement can occur as well. We have seen that in the presence of strong cross-barrier flow, precipitation can spill to the lee side (e.g., Sinclair et al. 1997). Some studies have further documented that lifting and orogenic convection occur when the low-level wind is directed upslope on the lee side (e.g. Lilly and Durran 1983; Tripoli and Cotton 1989). Others have shown that convergence of weakly stable low-level flow around three-dimensional terrain can generate lee-side showers and thunderstorms (Mass 1981; Goldreich and Freundlich 1997).

Finally, orographic modification of atmospheric waves and storm systems occurs at a variety of spatial scales, thus influencing precipitation (e.g., Parsons and Hobbs 1983; Davis 1997). On the windward side of a barrier, flow deceleration and convergence modifies cyclones, alters frontal structure and intensity, and decelerates frontal progression (e.g., Hobbs et al. 1975; Smith 1982; Braun et al. 1997; Neiman et al. 2004). Cyclogenesis may occur to the lee of a synoptic-scale or mesoscale barrier (e.g., Tibaldi et al.1990; Aebischer and Schär 1998).

1.2 Operational Doppler radar

Doppler radar provides reasonable spatial coverage and resolution of precipitation and wind to resolve precipitation processes over fine-scale orography,

except where severe clutter and shadowing occur (Georgis et al. 1999; Westrick et al. 1999). Automated rain-gauge and surface observation measurements are usually too sparse and infrequent to resolve fine-scale precipitation patterns over complex terrain. Moreover, Austin (1987) argues that a single rain gauge measurement is insufficient to sample the precipitation over *any* area because of its high spatial variability.

Operational Doppler radars now in place across the U.S. and other countries provide surveillance of orographic precipitation in some regions. They can be used to analyze a variety of precipitating systems (Wilson et al. 1980), and are particularly useful because of their three-dimensional scanning and fixed frame of reference in relation to terrain features. Operational radar design typically employs a small sampling volume (typically $1° \times 1° \times 1$ km) and rapid multiple-tilt volume scanning sequences (~5 min). Moreover, ground-based operational radars usually transmit at longer wavelengths (≥ 5 cm), minimizing attenuation of the radar beam by precipitation particles (Doviak and Zrnić 1993).

Nevertheless, radar has limitations. Because there is no unique relationship between radar reflectivity (Z) and rainfall rate (R), individual radar precipitation estimates generally have an uncertainty factor of 2 or more (e.g. Houze et al. 2004). Reflectivity depends on the particle diameter to the sixth power, summed over the sample volume, but the precipitation rate is approximately proportional to the diameter to the fourth power. Thus, Z-R relationships depend on particle types and

size distributions (Joss and Waldvogel 1990). Reflectivity also depends on the index of refraction of the scatterers and whether or not the cross-sectional area of airborne particles is small enough relative to the radar wavelength to produce Rayleigh scattering (e.g., Doviak and Zrnić 1993). Still other ambiguities exist, such as terrain clutter and shadowing, increasing sample volume size with range, beam refraction, and second trip echoes (Joss and Waldvogel 1990, Houze 1993). Doppler velocities are also susceptible to ambiguity such as aliasing (Chapter 2; James and Houze 2001). In the climatological mean, however, radar estimates become more reliable. It has been shown that larger temporal sampling greatly improves radar estimates by removing the scatter of individual measurements (Joss and Waldvogel 1990, Cain and Smith 1976).

1.3 Scientific objectives

This dissertation presents a body of work on orographic precipitation using long-term archives of operational Doppler radar data. The accuracy of radars over long time periods, as well as the high four-dimensional resolution of the data, are exploited and used to compute detailed precipitation and airflow climatologies. Two operational radars are used, one located on the Mediterranean side of the European Alps (Chapter 3) and the other in coastal Northern California (Chapter 4). These two locations were selected because of their relevance to field projects with precipitation objectives (i.e. the Mesoscale Alpine Programme [MAP], the Coastal Observation and Simulation with Topography [COAST] experiment, and the Cali-

fornia Land Falling Jets [CALJET] experiment) and because of their contrasting climates. The California coast generally represents a more statically stable atmospheric regime than the European Alps.

The main objectives of this research are as follows:

(1) To examine the detailed, climatological, three-dimensional structure of orographic precipitation and airflow corresponding to the rain-gauge studies by Daly et al. (1994) in Northern California (Fig. 1.1) and Frei and Schär (1998) in the European Alps (Figs. 1.2 and 1.3).

(2) To investigate the sensitivity of orographic precipitation to variations in the dynamics and thermodynamics of the impinging flow in both climates (Northern California and the Alps). Superposed epoch analyses (e.g. Reed and Recker 1971; Appendix) are performed on data from both radars to achieve this objective. Key variables to be analyzed are the wind direction, wind speed, static stability, and Froude number.

In order to accomplish these objectives, it was first necessary to develop a visualization tool capable of displaying three-dimensional radar volumes in relation to the underlying terrain (i.e. MountainZebra; James et al. 2000). In addition, the vast number of radar volumes in both studies required the development of quality-control algorithms to remove errors and ambiguities, including an efficient but highly effective Doppler dealiasing scheme (4DD; James and Houze 2001). Chapter

2 describes these research tools in detail. Chapter 3 presents radar observations of Alpine precipitation and summarizes the author's contributions to the 1999 MAP project. Then, Chapter 4 confirms and extends the findings of the Alpine study in the more stable climate of coastal Northern California. Finally, in Chapter 5, the results of this entire work are generalized and summarized.

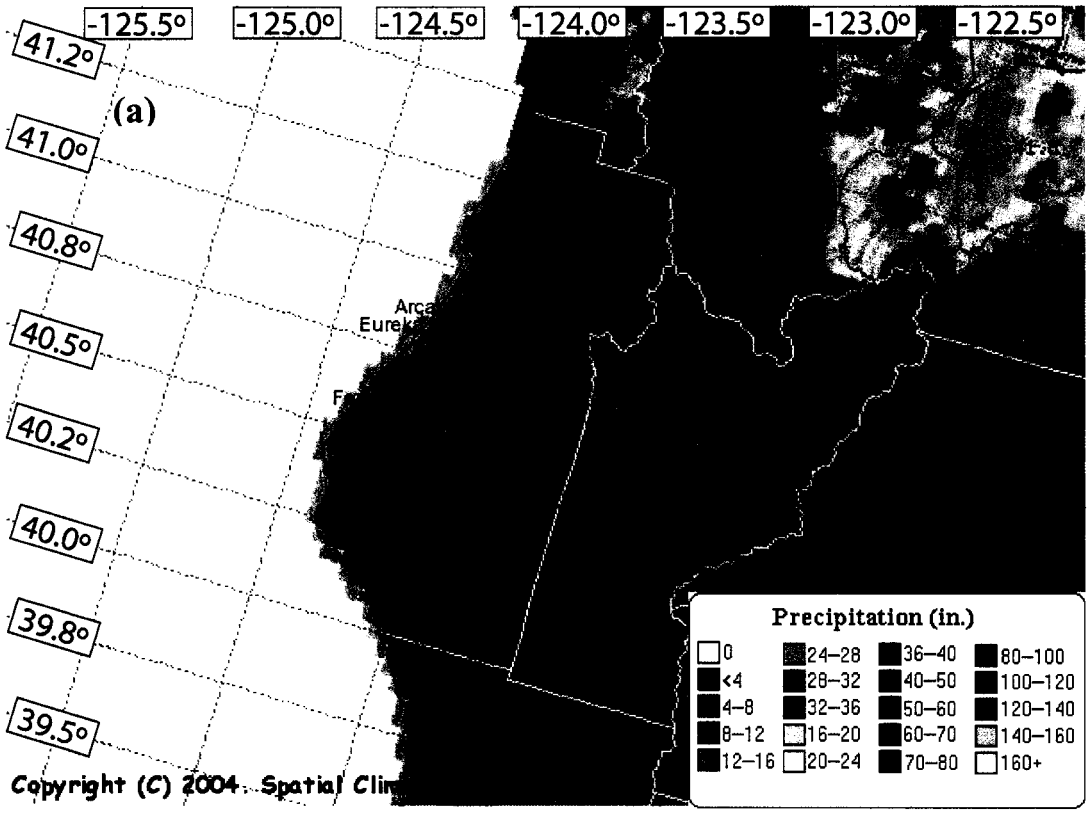

Figure 1.1. PRISM Model map of (a) average annual precipitation (1971-2000) and (b) underlying topography over Northern California (Source: Spatial Climate Analysis Service, Oregon State University, http://www.ocs.oregonstate.edu/prism/, created 31 Mar 2004).

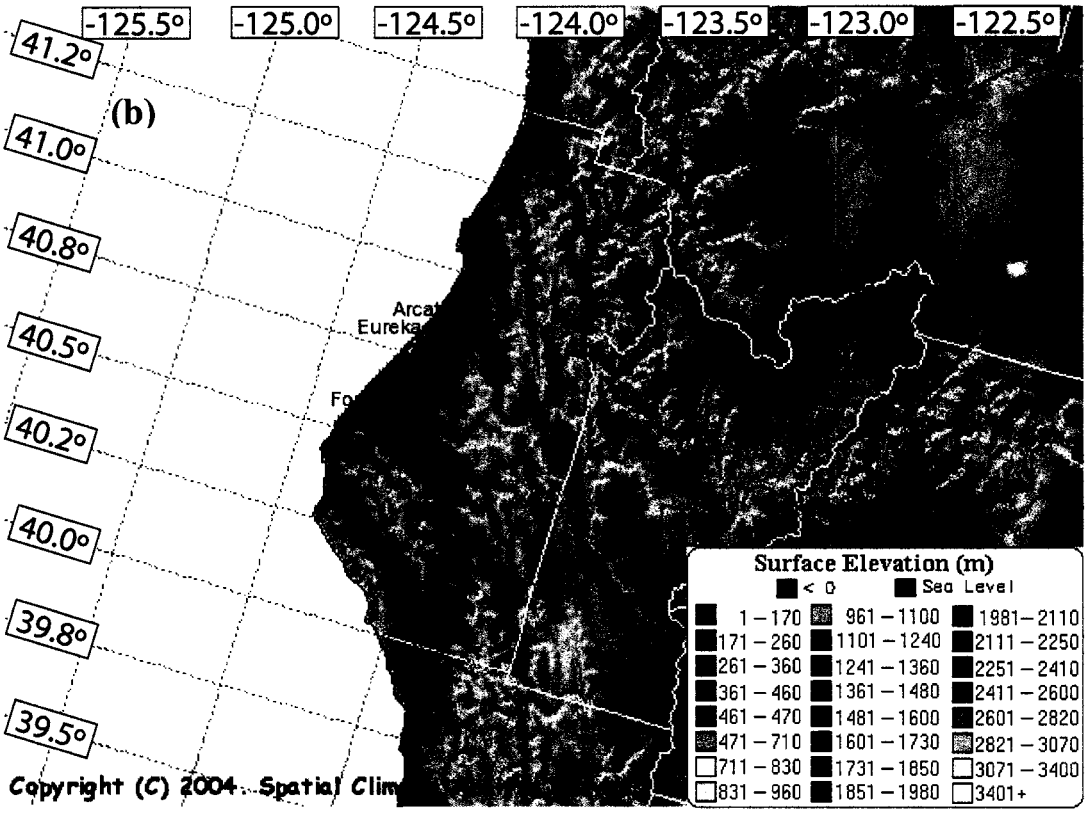

Figure 1.1. (continued)

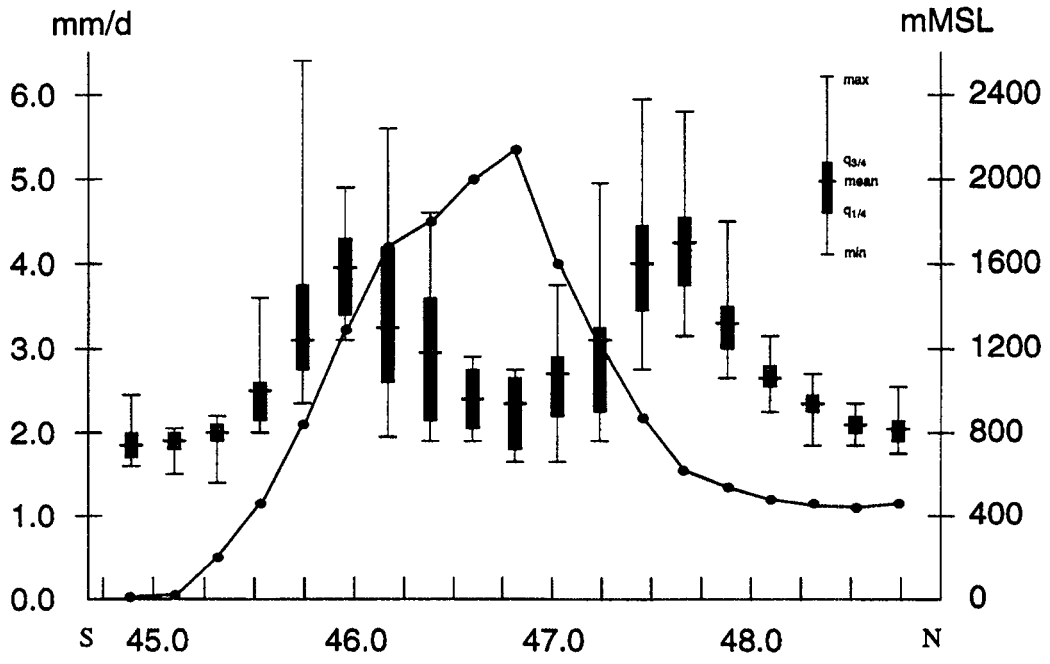

Figure 1.2. Average annual precipitation during the period 1971 – 1990 along a south–north section of the European Alps. The solid contour represents the zonally averaged terrain elevation between 10.2°E and 12.6°E longitude. The symbols indicate the mean, interquartile range, minimum, and maximum in the distribution of annual precipitation at rain gauge stations in each latitude belt. North (south) of 47°N, between 45 and 80 (10 and 30) stations were used to create each symbol (after Frei and Schär 1998).

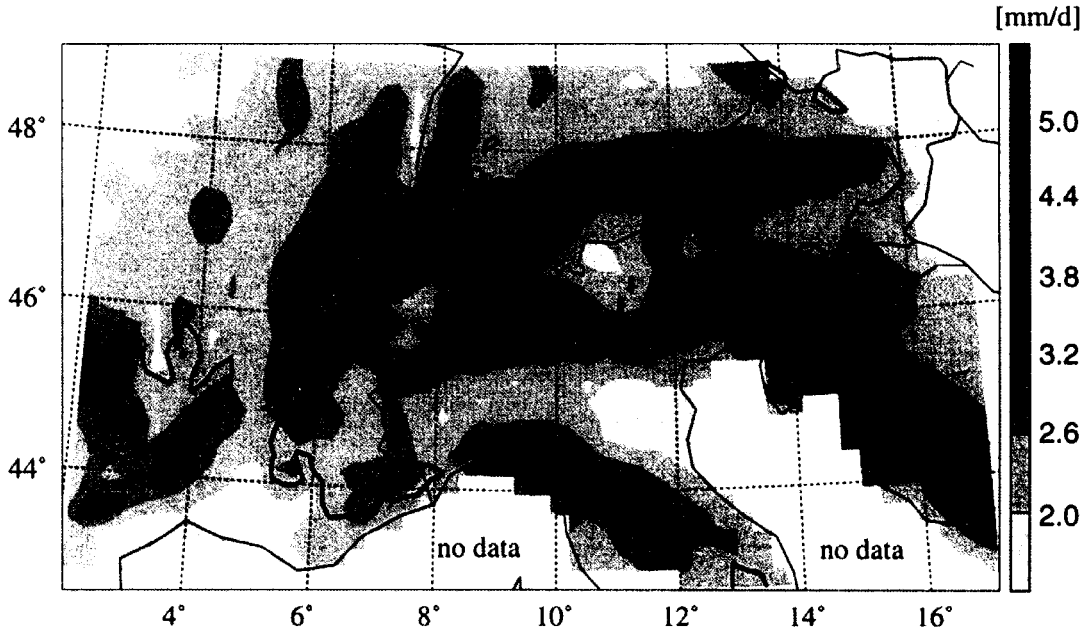

Figure 1.3. Average annual precipitation mapped using a distance-weighting scheme over the European Alps (1971 – 1990). The thick black contour represents 800-m MSL terrain elevation (after Frei and Schär 1998).

CHAPTER 2

RADAR DATA PROCESSING AND VISUALIZATION TOOLS

2.1 Motivation

To avoid contaminating the results of this research and ensure data quality, it was first necessary to correct or remove errors and artifacts from the radar archives. Optimum radar data quality control is achieved using software that requires considerable time and user intervention. However, in this dissertation research, manual editing would have been too time consuming, given the quantity of radar archives involved. Efficient and reliable software tools were implemented for automatically correcting full-volume radar data.

Other programs were used to interpolate, format, and display three-dimensional radar volumes with terrain. Together, these programs were arranged into a dataflow configuration called MountainZebra, which was developed by the Mesoscale Group at the University of Washington and was used to prepare and plot the radar data archives described in Chapters 3 and 4. MountainZebra operated on live data streams from ground-based radar data during the MAP Special Observing Period (Bougeault et al. 2001). The real-time efficiency of the software and the capability to display radar data with terrain in real time helped guide research operations in MAP. The author's contributions to MountainZebra are twofold: (1) the conception and implementation of terrain-based radar displays in MountainZebra and (2) the design and development of the Four-Dimensional Dealiasing

(4DD) algorithm, which was specially engineered to unfold radial velocities over complex terrain. These tools laid necessary groundwork for obtaining the results in Chapters 3 and 4 and for facilitating ongoing radar-data analysis by the UW Meso-scale Group and others. Sections 2.2 and 2.3 describe these tools in detail.

2.2 MountainZebra[2]

2.2.1 Radar and terrain

Mountainous terrain affects radar echo patterns by interfering with the radar beam and modifying precipitation processes and patterns. When the radar beam is intercepted by terrain, clutter and shadowing result (Joss and Lee 1995; Lin and Reilly 1997). Terrain modification of the airflow affects precipitation (Smith 1979; Houze 1993, Chapter 12). The spatial coverage and severity of clutter and shadowing depend on characteristics of the radar, the geometry of the terrain, and the refractivity of the atmosphere which varies with low-level stability and moisture stratification (Doviak and Zrnic 1993). In orographic regimes, the variability of the index of refraction is often greater than over flat terrain as a result of frequent low-level inversions (e.g., Gustavsson et al. 1998; Bell and Bosart 1988).

Since the 1970s, ray propagation models have been used to simulate terrain backscatter and shadowing. Recently, Lin and Reilly (1997) developed a technique that successfully reproduces terrain clutter patterns observed by shipboard radars near coastal mountains given the three-dimensional temperature and humidity of

the environment and the radar characteristics and location. However, for the purpose of visually identifying terrain clutter and shadowing operationally, it is not necessary to quantify terrain backscatter. One needs only to overlay the 3-D terrain on the 3-D echo pattern at comparable spatial resolution.

The Mesoscale Group configured a system that allows radar data and terrain to be displayed simultaneously in an operational environment. This system, called MountainZebra, consists of three elements: a data stream from an operational radar that is processed for analysis, a 3-D topography database, and NCAR's Zebra software (Corbet et al. 1994), which has the ability to display multiple real-time data sets. The purpose of this section is to describe the MountainZebra system and show how the incorporation of a terrain height field into a data visualization system aids the interpretation of radar data. First, overview of a proof-of-concept operation of MountainZebra on real-time data from the National Weather Service WSR-88D (Weather Surveillance Radar-88D) at Camano Island, located approximately 50 km north-northwest of Seattle, Washington. Then, the utility of superposed radar and terrain visualization is illustrated in the analysis of two examples of orographic precipitation.

2.2.2 The automated data flow

Figure 2.1 contains a schematic of MountainZebra's automated data flow for the Camano Island radar. Raw analog radar returns (Level I data) obtained by

---

[2] The text and figures in this section are adapted from James et al. (2000).

the WSR-88D propagate through the wave guide to the radar processor at the Radar Data Acquisition (RDA) site. The processor converts raw data to reflectivity, radial velocity, and spectral width in polar coordinates, applies clutter removal, and archives these data to exabyte tapes. The polar data format is hereafter referred to as "Level II" (Crum and Alberty 1993). The Level II data are then transmitted to the Radar Product Generator (RPG) at the National Weather Service Forecast Office (NWSFO), where various graphical (Level III) products are produced for display at the Principal User Processor (PUP) and disseminated to commercial data providers via the NEXRAD Information Dissemination System (NIDS). The Radar Interface and Data Distribution System (RIDDS; Rhue and Jain 1995) accesses the Level II data in parallel with Level III product generation within the RPG.

Via RIDDS, Level II data from Camano Island go to an on-site workstation where each ray is stored in a circular buffer. Once 100 rays (i.e., 5/18 of a radar sweep) are received, they are packaged, compressed, and queued for transmission to the Department of Atmospheric Sciences at the University of Washington. The data are sent via a nondedicated communication link to the department server at rates of up to 70 kbps. The rays are then uncompressed and reassembled into full Level II volumes. Each volume contains anywhere from 5 to 14 radar sweeps, depending on the volume coverage pattern (or scan strategy) used by the radar at that time. The Level II volumes are written to disk, where they remain for about a week before they are archived to tape. Meanwhile, a workstation dedicated to

MountainZebra processing and display immediately reads each reassembled Level II volume and converts it to Universal Format (UF; Barnes 1980; this process is not shown in Fig. 2.1). Then, algorithms may be applied to the UF file to remove non-precipitation echoes and correct aliased radial velocity. Finally, the data are bilinearly interpolated to a Cartesian grid using NCAR's SPRINT software (Mohr and Vaughan 1979).

Data storage limitations constrain us to use a 150 km · 150 km · 10.5 km interpolation grid with 2 km · 2 km resolution in the horizontal and 0.5 km resolution in the vertical. Figure 2.2 shows a vertical cross section of the elevation angle sequence typically employed by the Camano Island WSR-88D in precipitation mode. Figure 2.3 projects a small portion of the 0.5° elevation base scan onto a horizontal plane. In these figures, a 4/3 earth radius assumption[3] is used to approximate standard atmospheric refraction (Doviak and Zrnic 1993), and the Cartesian grid- point locations after interpolation are indicated by '+'. At low levels (< 2 km MSL) and close range (< 20 km), the interpolation grid reduces the vertical resolution of the tilt sequence (Fig. 2.2). Elsewhere, the interpolation grid is comparable to or at a finer resolution than the vertical resolution of the tilt sequence. At low levels, the WSR-88D provides 1 km resolution for reflectivity and 0.25 km resolution for radial velocity along each radial. Thus, the along-radial resolution is

[3] The current version of SPRINT makes this assumption during interpolation to approximate ray propagation. For the purpose of visually identifying terrain clutter, shadowing, and anomalous propagation, this assumption may not be adequate. Ideally, the interpolation routine should use a nearby sounding to better approximate ray propagation.

reduced by the 2 km horizontal interpolation everywhere in the domain. The azimuthal resolution is reduced at ranges less than 120 km, and especially at ranges less than 40 km (Fig. 2.3). The loss of resolution could easily be remedied by interpolating on a finer grid with the side effects of larger volume size, longer computation time for the interpolation, and greater oversampling of the grid versus the polar radar data at farther ranges. Another problem is that many of the grid points are located in data-void regions as a result of the NEXRAD scan strategy (e.g., between 4.3°, 6.0°, 9.9°,14.6°, and 19.5° elevation scans in Fig. 2.2). This limitation of the scan strategy can produce concentric rings of missing data in horizontal cross sections.

Interpolating the data to a Cartesian grid facilitates the computation and display of arbitrary horizontal and vertical cross sections and makes analysis more intuitive, without the "saw tooth" effect seen in Constant Altitude Plan Position Indicator (CAPPI)[4] displays. The Cartesian-interpolated fields further facilitate statistical and diagnostic computations with the data, especially those that involve spatial derivatives.

After interpolation by Sprint is complete, each volume is converted to Unidata's Network Common Data Format (NetCDF) for display. The NetCDF files are written to disk and transmitted back to the NWSFO (Fig. 2.1). Once the files are available on disk, dedicated workstations at both the Department of Atmos-

pheric Sciences and the NWSFO automatically ingest the data for display. Within one to two weeks, each NetCDF volume that is deemed meteorologically significant is moved to mass storage for future reference. Radar volumes in UF format are UNIX compressed, copied to tape, and deleted from disk.

2.2.3 Terrain-based visualization in Zebra

The automated data flow, which includes the acquisition, processing, and archival of each radar volume, is finished within 2 -4 min of the completion of a volume scan. MountainZebra then provides terrain-based visualization. Dedicated Zebra displays are located at both the NWSFO and the Department of Atmospheric Sciences. The displays update automatically when the processing of each new volume is complete. As described by Corbet et al. (1994), Zebra is highly interactive, allowing the user to synthesize multiple real-time data sets, overlay diverse fields, zoom in and out, specify any arbitrary horizontal or vertical cross section, change contouring options, and make time-lapse movies. MountainZebra includes topographical information on less than 1-km horizontal resolution, which can be displayed along with radar fields or other data sets in any arbitrary horizontal or vertical cross section selected by the user. Thus, four-dimensional interpretation of precipitation system structure and dynamics in relation to terrain geometry can be achieved.

---

[4] CAPPI displays are traditionally produced by assigning the value of the nearest data bin in the polar-coordinate tilt sequence to each grid point of a Cartesian array. Interpolation schemes use multiple gates and multiple sweeps in the vicinity of each Cartesian grid point to estimate its value.

The terrain contours in the horizontal and vertical cross sections were created using 30-sec digital elevation data from the Defense Mapping Agency (DMA) and NASA, but any high-resolution elevation field on a latitude-longitude grid is acceptable. In horizontal displays, a raster image of the terrain provides a backdrop for radar and other fields. Zebra contouring options allow the foreground fields to be displayed either as color contour, filled contour, or raster plots. The extent to which the underlying terrain is visible depends on the contouring option that is used (filled contour and raster plots obscure the terrain more than contour plots).

For each vertical cross section selected by the user, a terrain profile is plotted along the horizontal axis. To achieve this terrain profile, a bi-level terrain grid was computed from the digital elevation data, with vertical levels located at 0 and 10 km and a horizontal resolution of 30 sec. Each grid point was assigned the value of its altitude above ground level, with negative values indicating depth below the surface. The zero contour of this terrain grid, when bilinearly contoured in Zebra's vertical cross section windows, produces a high-resolution terrain profile for analysis with the other fields.

There have been other attempts to overlay radar data and topography. Doick and Holt (1995) created three-dimensional displays of radar and terrain and suggested that this would improve radar data interpretation and lead to new observational insights. MountainZebra accomplishes this goal particularly well by inter-

polating radar fields to a three-dimensional Cartesian grid (as opposed to vertically stacking CAPPI displays) and automatically updating. Zebra also allows the user to overlay any other relevant field (e.g., satellite data, mesoscale model fields, station data, etc.) with the radar data and terrain.

Archived radar data from other sources can also be converted to UF format, interpolated, and converted to NetCDF for analysis and display in customized versions of MountainZebra containing the appropriate topographic data. This method has been used to analyze data sets from several other radars in mountainous regions, including WSR-88D Level II archives from Eureka, CA, and encoded Graphical Image Format (GIF) archives from the Monte Lema radar of the Swiss Meteorological Institute, near Locarno, Switzerland. The latter configuration for Switzerland is part of a MountainZebra system customized for the European Alps which was the prototype for the near real-time system used in the 1999 Mesoscale Alpine Programme (Bougeault et al. 2001).

The sample displays that follow illustrate the utility of terrain-based radar data visualization for investigating orographic precipitation. All of the radial velocity cross sections are oriented radially to facilitate interpretation. The samples include stable orographic precipitation in western Washington and a squall line to the lee of the Alps.

2.2.3.1 Orographic precipitation in western Washington

At 0931 UTC 23 January 1998, widespread precipitation fell over western Washington in the moist, stable flow ahead of an approaching trough. The 1200 UTC sounding taken from the coastal town of Quillayute (UIL) exhibited a freezing level of 2.3 km MSL and a stable layer that extended from 700 to 500 mb. Horizontal cross sections of Camano Island radar reflectivity (Fig. 2.4a) and radial velocity (Fig. 2.4b) at 1.5 km MSL altitude show widespread precipitation and south-southwesterly flow. Precipitation was suppressed between 80 km west and 40 km south-east of the radar site as a result of subsidence to the lee of the Olympic Mountains. Just to the northeast of this "rain shadow," upslope enhancement of the precip-itation was occurring over the windward slopes of the Cascade Mountains.

A vertical cross section of reflectivity (Fig. 2.5a) extending from the radar toward the northeast (red line segment in Fig. 2.4a and 2.4b) reveals the enhanced precipitation over the lower windward slopes of the Cascades. The horizontal alignment of the reflectivity contours and the enhanced reflectivity associated with a bright band between 1.5 and 3 km altitude MSL indicate that the precipitation was strat-iform in nature. Orographic lifting was not destabilizing the thermodynamic profile enough to produce convection. The heaviest precipitation was occurring 50 – 65 km from the radar, where the reflectivity approached 40 dBZ. The radial velocity field along the same cross section (Fig. 2.5b) exhibited strong radial convergence in this region of maximum enhancement.

The vertical velocity w in the convergent region can be roughly estimated in two ways. Assuming incompressibility, and neglecting cross-radial divergence, the continuity equation can be approximated as

$$\Delta w \sim -\frac{\Delta u}{\Delta x}(\Delta z). \tag{2.1}$$

From Fig. 2.5a, it may be estimatedthat the convergence extended over an estimated 2-km depth Δz, with a deceleration $\Delta u \sim$ -10 m/s in the region x = 50 – 60 km along the cross section. Assuming that the vertical velocity at the ground was zero just upstream of the barrier, 2 m/s is obtained. Another way is to use the imper-meability boundary condition for a flow U impinging on a mean slope $\Delta h/\Delta x$,

$$w \sim U\frac{\Delta h}{\Delta x}. \tag{2.2}$$

Since $U \sim$ 20 m/s upstream of the barrier, and the slope 50 - 60 km from the radar is approximately 0.1, the same vertical velocity estimate is obtained. Thus, the radar fields appear to be consistent with the topographical forcing.

Overlaying radar fields with the topography in vertical cross sections allowed us to identify where orographic enhancement was occurring. It was greatest on the lower slopes—not at the crest of the Cascade Range (which is east of Mt. Baker). This characteristic was noted by Hobbs et al. (1975) in a case study of a front passing over the crest of the Cascades. Since the Camano Island radar data are being processed and archived routinely, it will be possible to determine if

enhancement of the precipitation on the lower slopes is typical or just a feature of certain types of cases.

Overlaying radar volumes with topography is also advantageous when assessing data quality. In this example, it may be noted in both Fig. 2.5a and 2.5b that the lowest scan was partially blocked by Mt. Baker (the tallest peak in the terrain profile). In this region, clutter suppression has removed data where mountain slopes were exposed to the radar signals. In Mt. Baker's shadow (x = 80 to 100 km), the returned power was less than immediately uprange.

A layer of maximum radial velocity (~ 25 m/s) spanned most of the vertical cross section (Fig. 2.5b). The radial velocity field oscillated with an apparent horizontal wavelength of 15 km. These oscillations could have been trapped internal gravity waves in the stable 700 - 500 mb (2.9 - 5.5 km) layer excited by flow over the Olympic Mountains just upstream. Although an exact quantitative assessment is not within the scope of this study, the nearest sounding available indicated a stratification that would support trapped waves. Also evident in the cross section is stronger downslope flow to the lee of Mt. Baker. This enhancement was immediately evident from the topography profile that is provided in every Zebra cross section.

2.2.3.2 A squall line to the lee of the European Alps

On 7-8 July 1996, a squall line formed to the lee of the European Alps and was well sampled by the Swiss operational C-band Doppler radar at Monte Lema in

Southern Switzerland (Fig. 2.6). Joss et al. (1998) describe this radar system in detail. The Swiss Meteorological Institute provided full-volume reflectivity and radial velocity data which were processed and interpolated to a Cartesian grid for terrain-based display. The squall line was associated with a surface meso-cyclone that formed to the lee of the European Alps and then moved eastward across Northern Italy under the influence of an upper-level trough. An analysis of the 14-km resolution Swiss Model (SM; Majewski 1991) simulation of this case indicates that the mesocyclone was similar to one simulated by Aebischer and Schär (1998), in terms of location, horizontal scale, and propagation. Such lee cyclones in Northern Italy are known to occur in two stages (Buzzi and Tibaldi 1978; McGinley 1982). In the first stage, the progression of a surface cold front is slowed by the terrain. Cold air invades the Mediterranean region and low-level vorticity is rapidly generated over the Gulf of Genoa and northwestern Italy. Dur-ing the second stage, the rate of cyclone development decreases to that of typical baroclinic systems as the upper-level trough interacts with the low-level cyclone.

Figure 2.6 shows the mesoscale SM forecast of sea level pressure for 0000 UTC 8 July 1996, initialized at 1200 UTC 7 July and integrated to 12 h. The 12-h integration is commonly regarded by the Swiss Meteorological Institute as the best estimate of the actual meteorological conditions. By 12 h the flow has not yet deviated much from the initial conditions, but it has had time to become dynamically balanced. The balanced conditions are essential for physically consistent inferences

about flow in relation to complex terrain. The SM output showed the approximate location of the mesocyclone at this time. Subsequent to 0000 UTC, the model produced northerly downslope flow (Fig. 2.7), with speeds of over 30 m s^{-1} by 1200 UTC.

Monte Lema radar data and terrain overlays indicated that prior to the development of downslope flow, thunderstorms were initiated by the upslope flow of moist, conditionally unstable air in the northeast quadrant of the mesocyclone. The convective activity extended from near the center of the mesocyclone toward the northeast, but exhibited very little convective organization in the weakly sheared environment. The Monte Lema radial velocity field (Fig. 2.8a) indicated that the downslope flow predicted by the SM converged with the flow around the mesocyclone. The convective cells intensified and became organized into a broken line (Fig. 2.8b), which propagated slowly to the southeast along the southeastern edge of a comma-shaped precipitation pattern in the reflectivity field (Fig. 2.9). The radial velocity field (not shown) indicated possible mesoscale rotation.

Vertical cross sections of radial velocity and reflectivity through the Alpine squall line exhibit structures that are common to midlatitude squalls (e.g., Skamarock et al. 1994). A convective cell is observed between x = 120 and x = 140 km (Fig. 2.10a), characterized by high reflectivity and deep vertical development. A trailing stratiform region is identified between x = 40 and x = 120 km, characterized by weaker reflectivity and horizontally aligned reflectivity contours. In the radial

velocity field (Fig. 2.8a), there is evidence of strong low-level convergence at the base of the convective line over the foothills of the Alps (x = 140 km; see Fig. 2.10b). Other structures that can be identified are front-to-rear flow at altitudes above 6 km in the trailing stratiform region, low- level rear inflow, and evidence of strong storm-top divergence.

Despite its prototypical structure, terrain-based radar displays together with forecast model output suggest that the squall line was influenced by orography. Analysis of the evolution of the radial velocity field indicates that between 0100 - 0200 UTC, a surge of downslope flow converged with the upslope flow around the lee cyclone. It was during this time that the convection became organized into a squall line. This downslope flow was observed by radar, in radial velocity cross sections in Fig. 2.8a and 2.10b, with the most intense radial inflow immediately above the Alpine slopes. It is believed that the downslope flow enhanced the rear inflow into the squall line, contributing to its development and organization.

2.2.4 Summary of MountainZebra

Terrain-based visualization improves radar data analysis over complex terrain, both in the identification of topographically induced errors and the investigation of orographic precipitation mechanisms. For this purpose, MountainZebra has been developed to acquire, process, archive, and display radar data in precise relation to the underlying terrain. Real-time WSR-88D Level II data from Camano Island, Washington are accessed via the National Severe Storm Laboratory's

RIDDS system and used as input to a chain of programs that reformats and interpolates radar data for display and analysis in NCAR's Zebra data visualization system. A high-resolution topography field was implemented by the author in Zebra so that the radar data are displayed in precise relation to the terrain height in any arbitrary horizontal or vertical cross section.

The sample cases in this section demonstrate the utility of terrain-based radar data visualization. In a stable precipitation event over western Washington, this technique aided in the identification of a rain shadow to the lee of the Olympic Mountains and stable orographic enhancement over the windward slopes of the Cascade Range. Evidence of gravity waves was also found in vertical cross sections through the radial velocity field.

Radar data from a squall line on the southern side of the European Alps were also examined in relation to the terrain. The squall line exhibited flow structures common to midlatitude squall lines. In addition there is evidence that orographic forcing contributed to its development. SM simulations and radar observations displayed and analyzed with topography in Zebra indicate that a lee mesocyclone produced upslope flow to trigger the convection. Later, synoptically forced downslope flow converged with the flow around the mesocyclone, further contributing to the organization of the squall line.

These cases demonstrate that by interpolating radar volumes to a Cartesian grid and overlaying them with the terrain in any horizontal or vertical cross section,

effective terrain-based visualization is achieved. Since Zebra can display any regularly or irregularly gridded geophysical field, this visualization technique can be expanded to include mesoscale model fields, satellite imagery, and other geophysical fields, and can be applied to both operational applications and research in mountain meteorology.

2.3 Four-Dimensional Dealiasing[5] (4DD)

During the 1999 Mesoscale Alpine Programme (MAP, Binder et al. 1995; www.map.ethz.ch, Bougeault et al. 2001), a ground-based Doppler radar array was configured to deduce the microphysical structure and three-dimensional wind field of precipitating systems over the southern slopes of the European Alps. According to Georgis et al. (1999), it was the third meteorological experiment ever conducted in complex terrain that provided multiple-Doppler observations, and only the second to focus on the evolution of the three-dimensional wind field over topography. More importantly, it was the first project of this type to produce three-dimensional Doppler radar syntheses of the mesoscale wind in real time (Chong et al. 2000; www.joss.ucar.edu/map/catalog/). These syntheses could not have been achieved without first removing aliasing error from the radial velocity fields by efficient, automatic dealiasing algorithms. This section describes 4DD, which was an important component of MountainZebra during MAP and made real-time syntheses possible.

2.3.1 Doppler aliasing

Aliasing occurs when the radar's pulse-repetition frequency (PRF) is too low to resolve the phase shift $\Delta\phi$ that occurs between successive pulses reflected by moving precipitation particles. This phase shift may be expressed as

$$\Delta\phi = \frac{4\pi V_r}{\lambda PRF}, \tag{2.3}$$

in which λ is the radar wavelength and V_r is the radial component of the target's velocity (see Houze 1993 for further discussion). The discrete sampling of the phase of reflected waves at a fixed time interval (or PRF) means that the true phase shift $\Delta\phi$ can never be known with certainty. The apparent phase shift detected by the radar may differ from the true $\Delta\phi$ by plus or minus some integer multiple of 2π. This circumstance is called aliasing. The maximum target velocity that will produce no aliasing is called the Nyquist velocity and is given by

$$V_n = \frac{\lambda PRF}{4}. \tag{2.4}$$

The apparent radial velocity V_a (assuming no aliasing) depends on V_r and V_n as

$$V_a = V_r + 2nV_n \tag{2.5}$$

where n is an unknown integer (positive or negative).

Dealiasing (often called unfolding) is the process of determining n at each radar gate such that the true radial velocity field (V_r) is retrieved from the apparent radial velocity field (V_a). In operational meteorology and in field research, dealias-

---

[5] The text and figures in this section are adapted from James and Houze (2001).

ing must be achieved automatically because of the vast quantity of radar data received in a given time interval. Dealiasing algorithms developed prior to this study have used either one-dimensional (radial) or two-dimensional (radial and azimuthal) continuity constraints to remove folds. Provided that an initial value of V_r is obtained at one of the gates in each contiguous data region, these schemes adjust V_a at the remaining gates by multiples of $2V_n$ to minimize gate-to-gate shear and retrieve V_r. Thus, dealiasing is similar to solving an initial value problem, where first-order derivatives are integrated over some interval and added to a specified initial value.

The efficacy of a dealiasing algorithm depends on radar characteristics and environmental conditions. In high wind events, and at low V_n, multiple folds lead to poor performance of the algorithm. When the gate-to-gate shear is poorly resolved by V_n, it is difficult and sometimes impossible to retrieve V_r. Stratiform precipitation echoes are more continuous and therefore easier to dealias than are convective echoes.

In orographic precipitation, dealiasing is particularly difficult. Convective initiation is common over orography (Banta 1990). The influence of mountains on the atmosphere results in a myriad of complex flow phenomena such as flow blocking, barrier jets, downslope flow, vorticity generation, and local wind systems (Smith 1979; Durran 1986; Schär and Durran 1997; Whiteman 1990). These effects produce horizontal and vertical shears that complicate dealiasing. When radar

beams encounter mountains, low-valued velocities result, which, if not removed, can be misinterpreted by dealiasing algorithms during strong wind events. Beam blockage also splits single precipitation systems into multiple radar echoes, further complicating the dealiasing problem.

An algorithm's performance also strongly depends on its design and the characteristics of the radar to which it is applied. Two important features that differentiate the existing dealiasing algorithms are the method used to produce initial values in each contiguous data region and the algorithm's ability to remove aliasing within that region in spite of strong shear, noise, and clutter. In preparing for MAP, the existing dealiasing schemes did not work well for the Swiss Meteorological Agency's Monte Lema radar (Joss et al. 1998). This radar operates with a particularly small Nyquist velocity of 8.27 m s^{-1} in the lowest tilts over the mountainous terrain. The resulting severe aliasing problems led us to develop a more comprehensive dealiasing scheme, which uses the full four dimensionality of an operational Doppler-radar data stream to remove aliasing error. The purpose of this section is to describe this powerful new dealiasing method and present the four-dimensional dealiasing algorithm.

2.3.2 Previous dealiasing algorithms

The first dealiasing algorithms were one-dimensional schemes using only radial information to diagnose and remove folds. Ray and Ziegler (1977) required that the gates in all or part of a radial be normally distributed about their mean.

They adjusted outlying gates by multiples of n. This technique can only be effective when the data are well approximated by a Gaussian distribution and only minor aliasing occurs.

Bargen and Brown's (1980) one-dimensional scheme used spatial continuity along each radial to remove local folds. They assumed that the first gate in each radial was free of error. They compare successive gates in the radial with averages of previously dealiased gates in the radial to evaluate the number of folds at each gate. However, strong wind events tend to violate the first-gate assumption. Their scheme therefore permits user intervention such as specifying an initial velocity, the number of preceding gates to include in the running average, or the dealiasing direction (i.e., radially away from or towards the radar and azimuthally clockwise or counterclockwise). The user is also permitted to edit the data. Nevertheless, user intervention is not feasible for real-time applications or very large data sets. In addition, Eilts and Smith (1990) suggest that one-dimensional continuity schemes cannot unambiguously dealias shear zones without incorporating other data dimensions.

Hennington's (1981) algorithm incorporated a vertical wind profile from a nearby sounding to calculate the radial component of the environmental wind field, V_{env}. In this approach, n is determined using the expression

$$n = \text{nint}\left(\frac{V_{env} - V_a}{2V_n}\right), \tag{2.6}$$

in which nint is a function that returns the nearest integer. However, this equation assumes that V_r falls within the range $\pm 2V_n$, which is unreasonable for radars with low V_n or during high wind events. Hennington's use of an environmental sounding neglects horizontal shear and requires the availability of a nearby sounding or wind profile. In addition, it fails to incorporate data continuity between adjacent radar gates to diagnose and remove aliasing.

Most dealiasing algorithms developed since the early 1980s have implemented spatial continuity constraints as well as some general information about the wind field. Thus they have combined the approaches of Bargen and Brown (1980), Hennington (1981), and others. The operational WSR-88D (Weather-Surveillance Radar 88D) algorithm (Eilts and Smith 1990) uses a vertical wind profile from an environmental sounding to produce initial values for each elevation scan and for isolated echoes. Otherwise, the scheme applies radial continuity constraints to remove local aliasing error and azimuthal continuity checks to mitigate error. The scheme also incorporates radial averages to determine n when continuity thresholds are not met. Thus, the scheme incorporates both supplemental wind information and two-dimensional continuity. It is efficient and has proven highly effective over the Great Plains for V_n values between 20 and 35 m s^{-1}.

Merritt (1984) developed a wind-field model technique that uses the radial velocity field around an azimuth circle to determine the wind direction. The wind model, which is allowed to vary with height while neglecting horizontal shear,

helped to interpret isolated echoes. Bergen and Albers (1988) expanded Merritt's scheme using WSR-88D VAD wind profiles (Browning and Wexler 1968) to include the magnitude of the wind as well as the direction. They found that VADs were adequate to resolve isolated data; however, their algorithm tests were performed for weak horizontal shear and with Nyquist velocities greater than or equal to 17 m s^{-1}. Bergen and Albers also experimented with a three-dimensional dealiasing approach. They tested several volume scans using vertical continuity from tilt to tilt to provide additional information to dealias isolated areas. They found that the three-dimensional technique performed just as well as the two-dimensional technique, and it reduced the need for auxiliary wind information from a VAD.

Jing and Wiener (1993) developed a sophisticated two-dimensional algorithm that solved a linear system that minimized gate-to-gate shear in each isolated echo. This technique assumes a smooth environmental wind field with weak shear and compares each locally dealiased echo to an environmental wind field estimate or VAD wind profile. The calculated average is then minimized by incrementing n equally over the entire echo. Jing and Wiener also assume that the average local wind observed by radar is less than V_n.

Yamada and Chong (1999) produced an algorithm that first locates the azimuth circle in each tilt that contains the largest number of valid velocity gates. Azimuthal continuity-based dealiasing is then applied, and the VAD from the single

azimuth circle is fitted to a second-order Fourier series. The zero-order Fourier coefficient is incremented by Nyquist intervals (i.e., multiples of $2V_n$) to retrieve V_r over the entire azimuth circle, which can subsequently be used to correct adjacent gates in the tilt. Unfortunately, this approach is only satisfactory when the available data coverage is high, the noise level is low, nonlinear wind components are negligible, and the Nyquist velocity is high.

Although dealiasing schemes have progressed significantly, none prior to the present study utilizes the full four dimensionality now available in most operational Doppler data streams. Instead, they rely heavily on auxiliary wind information such as soundings, wind models, or VADs. In various degrees, the schemes therefore fail to capture the full complexity of the wind field. They neglect horizontal wind shear, which is an important consideration during severe events and in complex terrain. Furthermore, few of these algorithms have been tested at low V_n (i.e., less than 15 m s^{-1}) where the dealiasing problem is particularly challenging, or over complex orography.

2.3.3 Description of 4DD

2.3.3.1 General philosophy and approach

Bergen and Albers (1988) suggested that adding the vertical dimension to a two-dimensional dealiasing scheme more accurately interprets the environmental wind field and diminishes an algorithm's requirements for auxiliary wind information. This reasoning can be extended to include the fourth dimension: *time*. Four-

Dimensional Dealiasing (4DD) is a scheme that utilizes the four dimensionality currently available with most operational Doppler data streams. 4DD was developed for and successfully used in real-time operation during MAP. It performed well in a highly sheared orographic regime at low V_n.

4DD also requires auxiliary wind information, but its dependence on this information is greatly reduced using the time dimension. In a series of radar volumes, the best approximation to the radial velocity field in a given volume is probably the velocity field of the previous radar volume as long as that field has been properly dealiased. Using the vertical dimension can also greatly improve dealiasing algorithm performance. Since operational radars usually employ higher PRFs at higher tilt angles, dealiasing is less difficult in the higher tilts. Noise, clutter, and wind shear also typically diminish with height, and higher tilts are therefore a valuable resource for dealiasing adjoining lower tilts. In addition to vertical and temporal continuity, 4DD uses both radial and azimuthal dimensions to interpret shear zones. Continuity constraints are also applied between gates that share the same corner, i.e., that are *diagonally* adjacent, thus further removing ambiguities caused by environmental shear.

Although 4DD uses all available data dimensions plus auxiliary wind information, the algorithm's construction is simple and straightforward (Fig. 2.11). Processing begins by reading into memory both the current radial velocity volume (CVR) and, if available, the previously dealiased radial velocity volume (PDVR).

Other algorithm inputs include the reflectivity field (DZ) and an environmental wind profile from a VAD analysis or sounding. The environmental wind data are loaded one height level at a time, beginning at low levels where VAD winds are typically more reliable. Then, as each level is loaded in succession, a vertical shear check is performed between the previous level and the current level. The current wind vector is deleted if the magnitude of the shear exceeds a user-specified threshold (default > 0.05 s^{-1}). The removal of strong vertical shear removes potentially erroneous winds and strong small-scale variability in the environmental wind profile. Once all levels are loaded that fall within the required shear threshold, the wind is linearly interpolated and the radial velocity field is estimated for each radar gate assuming standard atmospheric refraction (e.g., Doviak and Zrnić 1993) and negligible horizontal shear. The result is a smoothed, synthetic radial velocity field (hereafter EWVR).

After loading PDVR, EWVR, and CVR into memory, the algorithm examines CVR tilt by tilt, starting at the highest elevation where clutter is minimal and gate-to-gate differences in radial velocity are typically small compared to the Nyquist velocity. It then dealiases the lower tilts in descending order until the entire radial velocity volume is corrected. The algorithm performs six basic steps in each tilt: thresholding, filtering, initial dealiasing, spatial dealiasing, window dealiasing, and auxiliary dealiasing. A description of these six steps follows.

2.3.3.2 Thresholding

When the signal-to-noise ratio (SNR) is low, radar measurements are more affected by clutter, second-trip echoes, and other errors. Bergen and Albers (1988) note that low SNR gates should be removed prior to dealiasing to improve an algorithm's efficiency and to remove artificial gradients that can be misinterpreted as aliasing error. Bargen and Brown (1980) suggest thresholding as one possible way to remove noise. Prior to dealiasing, 4DD deletes all radial velocity gates in which the reflectivity falls outside of a user-specified valid range (default 0 to 80 dBZ). Another input parameter allows the user to delete a radial velocity gate when the corresponding reflectivity value is missing. As a result of the dBZ thresholding, many of the low SNR returns are removed. A more robust approach would be to threshold on raw power, spectral width (SW), and/or normalized coherent power (NCP) measurements; however, these fields are often not available in real-time operational data streams.

2.3.3.3 Filtering

Following data thresholding, a simple and computationally efficient Bergen and Albers (1988) filter is applied to remove isolated gates. Depending on the dealiasing algorithm, Bergen and Albers claim that the 3 × 3 filter can improve algorithm efficiency by a factor of 5 or more. Each gate within the radar tilt that contains a valid radial velocity value is considered. If more than three of its eight neighboring gates are missing, it is assigned a missing value flag and eventually

deleted. A second pass through the tilt then deletes any remaining gates in which all of the neighboring gates have been removed. This technique removes isolated points as well as questionable velocities in "speckled" regions (usually between 2 and 4% of the velocity gates are deleted). In good data regions, the filter effectively preserves echo boundaries and shapes, although a few of the gates that form sharp echo boundaries are removed (see Bergen and Albers 1988 for more details).

2.3.3.4 Initial dealiasing

Following thresholding and filtering, initial dealiasing is performed in each tilt using temporal and vertical continuity. This step assumes that local changes in the true radial velocity (ΔV_r) between two successive volumes (typically ~ 5 min) are small compared to V_n. In most cases this assumption holds true, and it is possible to dealias CVR against the PDVR. Unfortunately, such a simple time continuity constraint, when used alone, allows errors in the previous volume to pass into the current volume and propagate indefinitely through the data stream. In addition, measurement error, noise, strong wind shear, and strong accelerations can produce large ΔV_r values that are not well resolved by V_n and generate new errors. This problem is particularly apparent for radars with low V_n.

To mitigate the development and propagation of error, 4DD uses the vertical dimension along with the time dimension to constrain initial dealiasing. Only those gates in CVR that can be dealiased to within $0.25V_n$ of the same gate in PDVR *and* $0.25V_n$ of the nearest gate in the previous tilt above are considered

correctly dealiased. These gates are saved and assigned a "good" flag; all others are left unaltered. This routine produces a number of gates scattered throughout the tilt that are dealiased to a high degree of confidence and that serve as initial-value gates for spatial dealiasing.

If PDVR is unavailable (i.e., dealiasing is being initialized on the first of a series of volumes), EWVR is used in its place. Since EWVR is generated using a VAD or sounding (neglecting horizontal shear), dealiasing is typically more problematic in the first few volumes in a sequence. Ordinarily it should not be necessary to reinitialize dealiasing as long as the data flow is uninterrupted by radar outages or communication problems.

2.3.3.5 Spatial dealiasing

In spatial dealiasing, good initial-value gates are used to dealias adjacent gates spatially within the tilt. Each gate that borders a good gate is adjusted by an integer n such that it agrees with all of its neighboring good gates (maximum eight) within a gate-to-gate shear threshold[7] of $0.4V_n$. If this procedure is successful, the value of the current gate in question is saved, flagged as "good," and used to dealias other gates. Otherwise, it is assumed that noise or shear has been encountered and the algorithm saves the gate for future passes, thus allowing the algorithm to postpone problem gates until more good gates are available to interpret them. Postponing these difficult gates makes dealiasing more robust in high-shear

regions. In addition, errors that more commonly originate in high-shear regions are confined to smaller areas since the surrounding gates are dealiased first.

During the first spatial dealiasing pass, 4DD scans outward along each radial and progresses radial-by-radial in a clockwise direction. During each successive pass, 4DD alternates between clockwise and counterclockwise progression while continuing to scan radially outward. The purpose for employing alternating directions is to improve algorithm efficiency and to allow 4DD to dealias around shear zones and problem areas during the first two passes. During the third pass, the threshold is relaxed to $1.0V_n$ and each gate must now agree with only a majority of the neighboring good gates, rather than all of them, for dealiasing to be considered successful. Thus, spatial dealiasing begins to interpret the more difficult regions during its third pass through each tilt and continues until completing a total of ten passes or until the number of remaining gates with adjacent good gates decreases to zero.

Figure 2.12 illustrates the behavior of the spatial dealiasing routine in a hypothetical range-azimuth sector. In this example, it is assumed that the gate-to-gate shear is less than $0.4V_n$ over the entire sector except between the two thick dashed lines. The initial-value gates (i.e., those that were dealiased by the initial dealiasing routine) are labeled "I" in the figure. During the first spatial dealiasing pass, 4DD scans outward along each radial in clockwise order (left to right in Fig.

[7] The threshold value 0.4 was obtained through preliminary tests of 4DD. Threshold values greater than 0.4 produced more frequent errors, while lower values decreased algorithm efficiency.

2.12), incrementing each available uncorrected gate by Nyquist intervals until its value falls within $0.4V_n$ of any adjacent initial-value gate or previously corrected gate. If successful, the value is saved and used to dealias other gates. If unsuccessful, the gate is left unchanged and is examined during subsequent spatial dealiasing passes. In the sample range-azimuth sector (Fig. 2.12), a number of gates are successfully corrected during the first pass (labeled "A"). However, it is important to note that some gates within the first four radials remain uncorrected after the first pass simply because the radials are examined in clockwise succession. Other gates remain because they lie within the shear zone (between the dashed lines) where the gate-to-gate shear exceeds the $0.4V_n$ threshold.

4DD then performs a second spatial dealiasing pass in a manner identical to the first, except that the radials are examined in counterclockwise succession. By alternating the order in which the radials are examined, most of the remaining gates (labeled "B" in Fig. 2.12) are successfully dealiased during the second pass. Without alternating from clockwise to counterclockwise between successive passes, additional spatial dealiasing passes would be required to achieve the same result, and the algorithm's efficiency would be significantly less.

After the second pass, only those gates located within the shear zone remain uncorrected (labeled "C"). These remaining gates are more easily dealiased during the third and subsequent passes, now that corrected gates are available on both sides of the shear zone and the gate-to-gate shear threshold is relaxed to $1.0V_n$. This

example demonstrates how 4DD is more forgiving of strong gate-to-gate shear than other algorithms and approaches problem-dealiasing regions from all sides. This ability of the algorithm to save the most difficult dealiasing until the end reduces the areal extent of errors when they occur and is analogous to the way a trained observer would treat a difficult dealiasing problem.

Figure 2.13 illustrates 4DD performance in more detail. Figure 2.13a and b, respectively, depict the radial velocity field within a hypothetical 3 × 3 gate radar echo before and after spatial dealiasing. In this example, it is assumed that the Nyquist velocity is 8 m s^{-1} and that only two of the nine gates have passed initial de-aliasing as initial-value gates (shaded gates, Fig. 2.13a). During the first pass of the spatial dealiasing routine, 4DD first examines the left radial. The second and third gates are considered "good" because the gate-to-gate shear between successive gates is less than $0.4V_n$ (or 3.2 m s^{-1}). However, the middle radial is left uncorrected during the first pass because none of the three gates in the radial can be adjusted by Nyquist intervals (16 m s^{-1}) such that their values fall within 3.2 m s^{-1} of their adja-cent "good" gates. In the third radial, the second gate is corrected by adjusting its value by -16 m s^{-1} such that it differs from the adjacent initial-value gate by only 1 m s^{-1}. Thus three gates are corrected during the first pass (medium shading, Fig. 2.13b).

The algorithm then proceeds into the second spatial dealiasing pass, which examines the right radial first. It is found that by adjusting the first gate in that

radial by one Nyquist interval, its value becomes -15 m s^{-1} (pinstripe, Fig. 2.13b), which falls within $0.4V_n$ of the adjacent gate that was corrected during the previous pass (-18 m s^{-1}). The algorithm then scans the middle radial, but leaves all three gates in the radial uncorrected since none of them can be adjusted to agree with all their adjacent "good" gates within $0.4V_n$. Only during the third pass is the middle radial dealiased, because now the threshold is relaxed to $1.0V_n$ (8 m s^{-1}), and each gate is required to agree with only a majority of its adjacent gates. In Fig. 2.13b, it appears that dealiasing was properly achieved, yet ambiguities result when the magnitude of the gate-to-gate shear exceeds the Nyquist velocity, such as between the left and middle radials. In some high-shear cases, the true radial velocity field becomes impossible to retrieve, despite the fact that 4DD's use of multiple data dimensions is forgiving of strong shear.

2.3.3.6 Window dealiasing

Following spatial dealiasing, many gates may remain uncorrected because they are not directly adjacent to groups of corrected gates. Prior to incorporating auxiliary wind information from a VAD or sounding, a windowing step is performed because a local average of good velocity gates is likely to be a better estimate of the wind at a given gate than EWVR. During window dealiasing, 4DD scans through the gates that still remain to be corrected. Each gate is compared to

the average value of all good gates within a centered azimuth-range window[7] of dimensions 11 × 11. If the population of good gates within the window equals or exceeds 5, then their collective mean and standard deviation are computed; otherwise the window is expanded to 21 × 21. If the population of the enlarged window is still too small, the central gate is saved for the auxiliary dealiasing routine. Otherwise, the central gate is adjusted by increments of $2V_n$ until its value falls within $\pm V_n$ of the population mean. If the standard deviation is less than a specified threshold and the gate in question can be adjusted to within $0.7V_n$ of the mean, then the value is returned; otherwise it is deleted because of the data scatter in the vicinity of the gate. Gates with low scatter and in close agreement (within $0.4V_n$) with the population mean are flagged as "good" and used to dealias other gates. 4DD tests indicate that a standard deviation threshold of about $0.8V_n$ generally works well.

2.3.3.7 Auxiliary dealiasing

After windowing, isolated echoes within the tilt may remain uncorrected. If new echoes have developed or moved within the range of the radar, initial dealiasing fails to interpret them using temporal and vertical continuity. In regions where valid data are unavailable in the adjoining tilt above, initial dealiasing also fails. Some echoes may fail the initial dealiasing step simply because the radial velocity values deviate from corresponding gates in the previous volume and the adjacent

[7] In order to maintain algorithm simplicity and efficiency, window dealiasing considers azimuth-range windows rather than geographic areas.

tilt. As a last resort, these echoes must therefore be initialized using auxiliary wind information.

If auxiliary wind information (EWVR) is unavailable, auxiliary deliasing obviously cannot be performed. If PDVR is unavailable, EWVR is used as a substitute for PDVR during initial dealiasing, and it is therefore not necessary to use EWVR again during auxiliary dealiasing. Therefore, the auxiliary dealiasing routine is performed only if both PDVR and EWVR are available. During auxiliary dealiasing, an attempt is made to initialize each gate within the remaining uncorrected echoes by comparing it with the corresponding gate in EWVR. If its value can be adjusted by Nyquist intervals such that it agrees to within $0.5V_n$ of EWVR, the velocity gate is saved, and a "good" flag is assigned. After the isolated echoes are initialized using EWVR, spatial dealiasing ensues within each echo.

Following a maximum of ten alternating clockwise and counterclockwise passes through the tilt, those gates that cannot be dealiased are deleted and dealiasing is then complete for that tilt. Occasionally, isolated echoes are encountered in which none of the gates can be dealiased to within $0.5V_n$ of the auxiliary wind information. 4DD makes no attempt to interpret these echoes further, and they are deleted to prevent error propagation into later volumes.

2.3.4 Algorithm performance

4DD operated in real time on C-band Doppler velocity measurements from the Swiss Monte Lema radar throughout the entire two-month duration of MAP.

The time required to process the 20-tilt volumes on a Sun Ultra 10 workstation (300MHz UltraSPARC-IIi, 4.3GB HDD, 128MB DRAM) ranged from approximately 5 to 20 s, depending on the quantity of valid gates contained in the volume. This efficiency could have been greatly improved by reading/writing a more compact radar format than Universal Format (UF; Barnes 1980).

The Monte Lema radar is located at 1.6 km MSL elevation on the southern side of the European Alps where the flow and climatological precipitation are strongly influenced by orography. Monte Lema velocities pose a challenge to any dealiasing algorithm because the lowest tilts are largely attenuated by terrain clutter and fragmented by shadowing. Furthermore, with a wavelength (λ) of 5.515 cm and a pulse repetition frequency (f) of 600 s^{-1}, V_n equals just 8.27 m s^{-1} in the four lowest tilts (see Joss et al. 1998 for more details).

4DD nevertheless produced consistent and reliable results during both convective and stratiform precipitation events. This success could be attributed, in part, to the availability of wind profile estimates from an operational VAD algorithm (Germann 1999). Because the VAD algorithm is capable of producing VADs from an uncorrected radial velocity field, the wind profiles were available for nearly every volume and provided an excellent source for auxiliary wind information. However, as stated before, the VAD winds were only used when initializing the dealiasing chain and during auxiliary dealiasing. Figure 2.14 shows a sample 0.5° tilt dealiased by 4DD on 20 September 1999. On that day, wind speeds exceeded

30 m s^{-1} with considerable embedded convection and turbulence apparent in the radar fields. Even to the trained observer, manual dealiasing of this radial velocity tilt appears nearly impossible without some knowledge of the velocity field (see Fig. 2.14a). However, as exhibited in Fig. 2.14b, it appears that 4DD correctly dealiased the noisy, doubly folded radial velocity field.

Prior to MAP, 4DD was rigorously tested on 241 volumes obtained during two complex events observed by the Monte Lema radar. The first case (3 September 1998) exhibited embedded convection and considerable data scatter near the Alpine crest that appeared to be associated with strong turbulence. In the second case (5 September 1998), strong horizontal and vertical shear was observed in conjunction with a squall line similar to the one documented in Section 2.2. By locating discontinuities in the radial velocity field, errors were identified and the source of error in each volume was investigated. The areal extent of the error in each tilt was also estimated and documented. Table 2.1 summarizes the test performance of 4DD during the two events, with a total of 241 volumes examined. Results indicate that over half (134) of the volumes contained at least one erroneous gate. On the other hand, an impressive 3993 or 93% of the 4300 tilts containing valid data were correctly interpreted by 4DD. The average number of tilts per volume containing errors was therefore 1.27 (usually in one of the lowest four sweeps where V_n was lowest). To illustrate the areal extent of these errors, the erroneous gates in the most problematic tilt in each volume covered an average of just 3% of the geographical

area covered by the tilt. These statistics indicate that though the errors produced by 4DD were frequent, they were typically very localized. It should also be kept in mind that these were highly turbulent, sheared events at very low V_n and that these statistics are a pessimistic representation of the algorithm's overall performance.

Table 2.1 also indicates that a number of isolated radar echoes were deleted during auxiliary dealiasing (an average of one echo in every four volumes). As stated earlier, the auxiliary dealiasing routine is designed to delete echoes if none of the gates can be dealiased to within $0.5V_n$ of the corresponding gates in EWVR. The fact that so many echoes were deleted by auxiliary dealiasing is an indication that the velocity field during these high-shear events was not well approximated by a one-dimensional environmental wind profile. These results justify the need for four-dimensional dealiasing algorithms that minimize the use of auxiliary wind information.

Table 2.2 tallies the leading source of dealiasing error within all of the problematic radar volumes during both events (134 volumes total). The errors originated from a number of causes, the most common (54%) being strong gate-to-gate shear that was poorly resolved by V_n. In some cases, the gate-to-gate shear approached magnitudes of $2V_n$ or more, making proper dealiasing impossible by almost any means. The other major source of error (36%) was the occurrence of isolated echoes that were incorrectly interpreted by EWVR during auxiliary de-aliasing. One surprising result implied from the results in Table 2.2 is that error

propagation between successive volumes was *not* a significant source of error. Once sources of error disappeared from the radial velocity field (e.g., strong shear subsided or isolated echoes became connected with other echoes), the errors went away. Thus, the use of both vertical and temporal continuity constraints during initial dealiasing effectively mitigated error propagation.

2.3.5 Summary of 4DD

A review of existing radial velocity dealiasing algorithms indicates that each neglects environmental wind shear in one way or another. Early dealiasing algorithms made simple assumptions about the character of the wind field (e.g., Bargen and Brown 1980). More recent schemes have relied on auxiliary information from a nearby sounding (e.g., Eilts and Smith 1990), a VAD wind profile (e.g., Bergen and Albers 1988), or a radar-generated wind model (e.g., Yamada and Chong 1999). These approaches are too simplified to operate in high-shear orographic regimes and/or at low Nyquist velocity. The extensive use of auxiliary wind information arises from the fact that these algorithms fail to incorporate the full four dimensionality available in modern operational radar data streams.

Scaling arguments indicate that for typical mesoscale flow resolved by operational Doppler radars, the previous radar volume adequately approximates the current radial velocity field, if it is properly dealiased. Bergen and Albers (1988) produced promising test results indicating that the addition of the vertical dimension reduced the need for auxiliary wind information. Our study shows that incor-

porating the vertical dimension together with the time dimension helps mitigate the propagation of errors between successive volumes and effectively initializes dealiasing while minimizing the need for other wind information.

Following initial dealiasing, based on time continuity, 4DD applies azimuthal, radial, and diagonal continuity to remove local folds. The use of multiple dimensions during spatial dealiasing makes 4DD less susceptible to errors caused by strong shear and noise. The spatial dealiasing scheme in the algorithm is designed to postpone dealiasing difficult regions until the first two passes are complete. These passes are performed in alternating directions, improving the algorithm's efficiency and allowing shear zones to be approached from less complex regions on all sides. These steps make 4DD forgiving of strong shear, although excessive gate-to-gate shear approaching magnitudes of $2V_n$ may be impossible to dealias properly. Following spatial dealiasing, the algorithm then applies area averaging to evaluate remaining disconnected gates and problem areas. Because auxiliary wind information from a sounding or VAD neglects horizontal shear, it is incorporated in the final dealiasing step as a last resort when isolated echoes cannot be interpreted otherwise.

Like all dealiasing algorithms, 4DD has limitations. As a new algorithm, the sensitivities of its shear parameters are not well understood. Its performance could be improved by further testing these sensitivities and fine-tuning the parameters for a given Nyquist velocity and/or climatic regime. Another limitation is the interpre-

tation of distant isolated cells that develop or move within range of the radar, or when fast-moving highly sheared features are observed. Though vertical and temporal continuity constraints are used to mitigate errors during initial dealiasing, these scenarios sometimes prove problematic for 4DD. Further testing of 4DD's performance, especially in comparison to other dealiasing algorithms at various Nyquist velocities, is therefore warranted.

There are also a few logistical limitations associated with 4DD. The algorithm uses four-dimensional information to dealias each sweep, and therefore should operate on a continuous full-volume data stream. Whenever there are breaks in the data transmission, it relies heavily on auxiliary wind information, thus increasing the likelihood of errors in the first volume or volumes thereafter. In addition, 4DD must operate on a regular tilt sequence, beginning with the highest tilt and proceeding on down to the lowest. Otherwise, it must wait until the volume scan is complete before beginning the dealiasing sequence, resulting in a time lag that could be unfavorable for some real-time applications. 4DD also requires more memory than most algorithms because it refers to the previous radar volume and previous tilt, though this latter limitation could be remedied somewhat by storing only a fraction of the good radar gates from the previous volume and tilt in memory.

Nevertheless, 4DD performed efficiently and consistently in real time during MAP. Typical clock times per volume on a Sun Ultra10 workstation ranged

from 5 - 20 s, depending on the number of valid gates contained in the volume, the number of tilts, and the radar gate geometry. 4DD bench tests using WSR-88D volumes are less time efficient because the azimuth angles of WSR-88D radials vary between successive volumes and adjacent tilts, and a significant amount of processing time is spent locating the correct radial. In addition, WSR-88D radial velocity gate spacing is 0.25 km, which gives four times the resolution available in Monte Lema data.

4DD was further tested during two precipitation events over complex terrain observed by the Swiss Monte Lema radar at Nyquist velocities as low as 8.27 m s^{-1}. A total of 93% of the 4300 tilts containing valid data sustained no error. When errors occurred, they were usually very localized, resulting mainly from excessive shear and incorrect VAD-based echo interpretation. Although further research is needed to assess 4DD's effectiveness in other climatic regimes, the scheme produced promising results in a variety of meteorological conditions during MAP.

4DD is gradually gaining acceptance by the scientific community and being tested on an ongoing basis. In addition to being tested operationally by the Swiss Meteorological Agency (MeteoSwiss), the scheme has been ported to the Thunderstorm Auto-Nowcasting environment by the University Corporation for Atmospheric Research (UCAR) Research Applications Program (RAP). This system integrates a variety of data and software tools for short-term thunderstorm forecasting

(http://www.rap.ucar.edu/projects/nowcast/). It is currently being tested operationally by RAP at the National Weather Service Forecast Office at Dallas, TX, in preparation for deployment to the 2008 Summer Olympics in Beijing, China (personal communication, Susan Dettling).

Table 2.1. 4DD's test performance (3 and 5 September 1998).

Statistic	**Result**
Total volumes dealiased	241
Number of volumes returned with error	134
Average number of tilts per volume with error	1.27
Average number of isolated echoes deleted per volume	0.25
Total number of tilts containing valid data	4300
Number of tilts with aliasing	2414
Number of tilts containing valid data returned without error	3993
Number of tilts containing valid data returned with error	307
For the most problematic tilt in each volume:	
• Average percentage of tilt area with error	3%
• Average percentage of valid data area with error	10%

Table 2.2. Leading causes of error by volume (3 and 5 September 1998).

Leading Cause of Improper Dealiasing	**No. of Volumes**	**% of Total (134)**
Unresolved shear:	73	54%
• Horizontal shear	40	30%
• Strong turbulence	25	19%
• Vertical shear	8	6%
Echoes incorrectly interpreted (using EWVR)	48	36%
Noise	8	6%
Unknown	5	4%

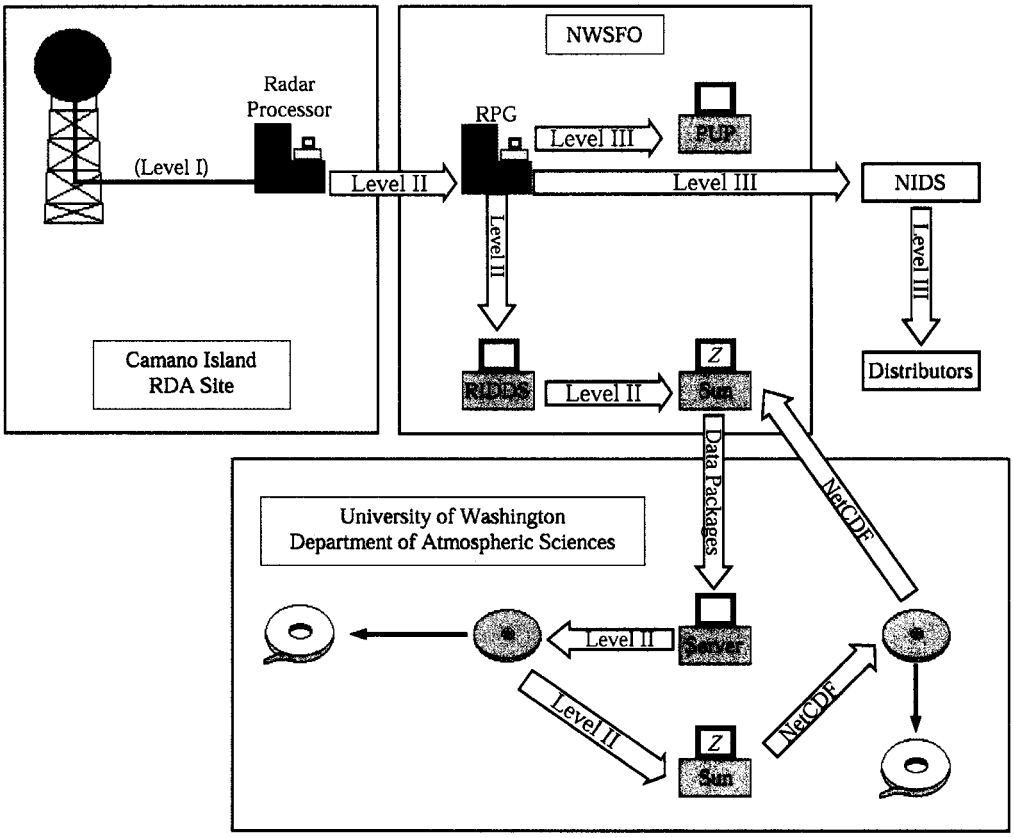

Figure 2.1. Schematic of the Camano Island WSR-88D data flow. Enclosed in large rectangles are the Radar Data Acquisition (RDA) site (top left), the Seattle National Weather Service Forecast Office (NWSFO; top right), and the University of Washington Department of Atmospheric Sciences (bottom). Workstations equipped with the Zebra software are indicated with a "Z". Conversion to UF is not shown, but takes place at the University of Washington.

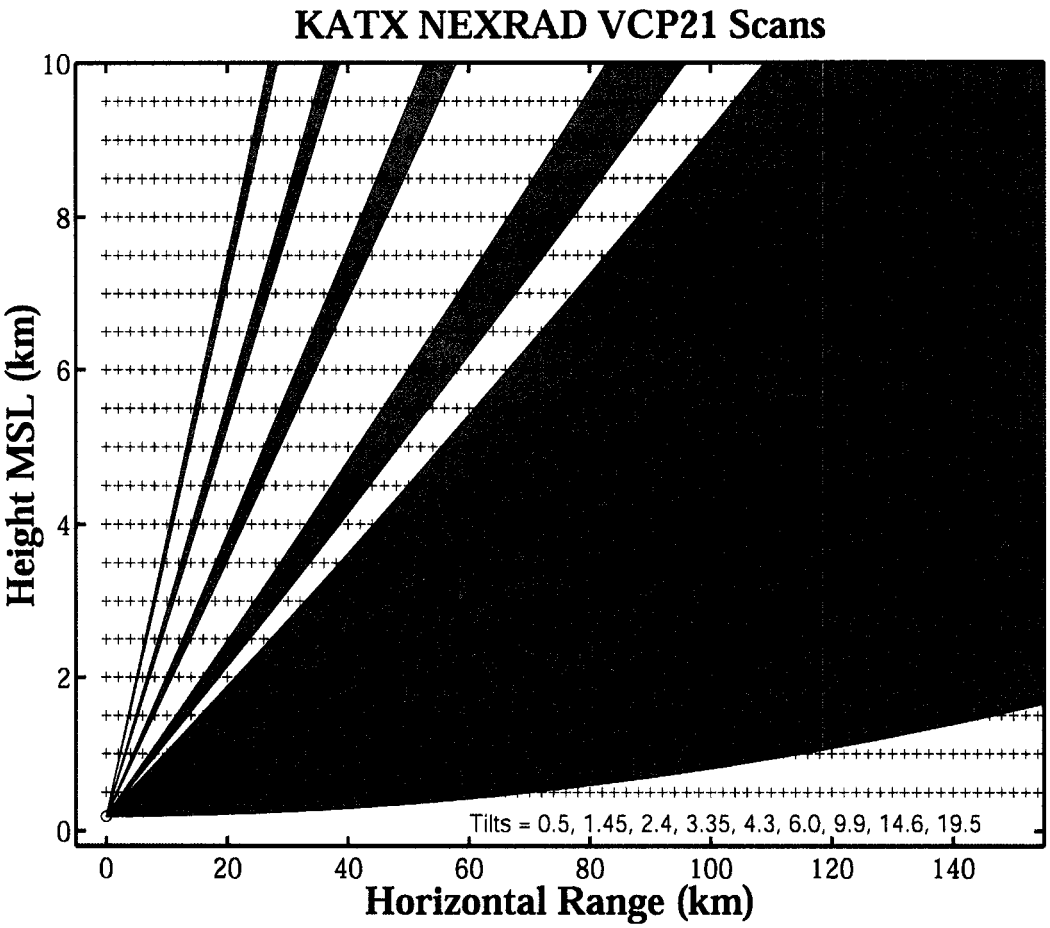

Figure 2.2. WSR-88D tilt sequence using Volume Coverage Pattern 21 and assuming standard atmospheric refraction. The location of the radar dish is indicated by the open circle at 0.0 km horizontal range. The Cartesian grid-point locations are indicated by '+', and the gray regions represent the cross-sectional area spanned by the radar's beamwidth.

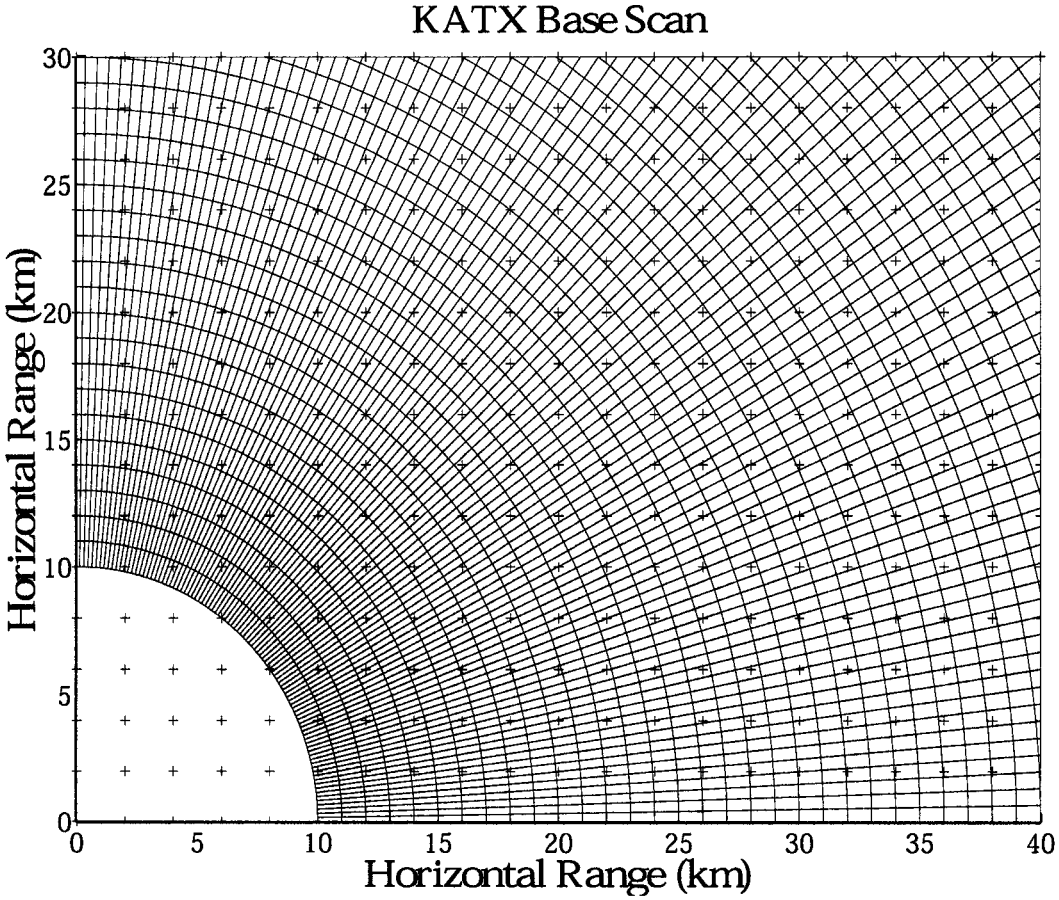

Figure 2.3. The bin geometry of the northeast quadrant of the WSR-88D base reflectivity scan (0.5°) at close range, projected onto a horizontal plane. The Cartesian grid point locations are indicated by '+'. The bins at range less than 10 km are not shown.

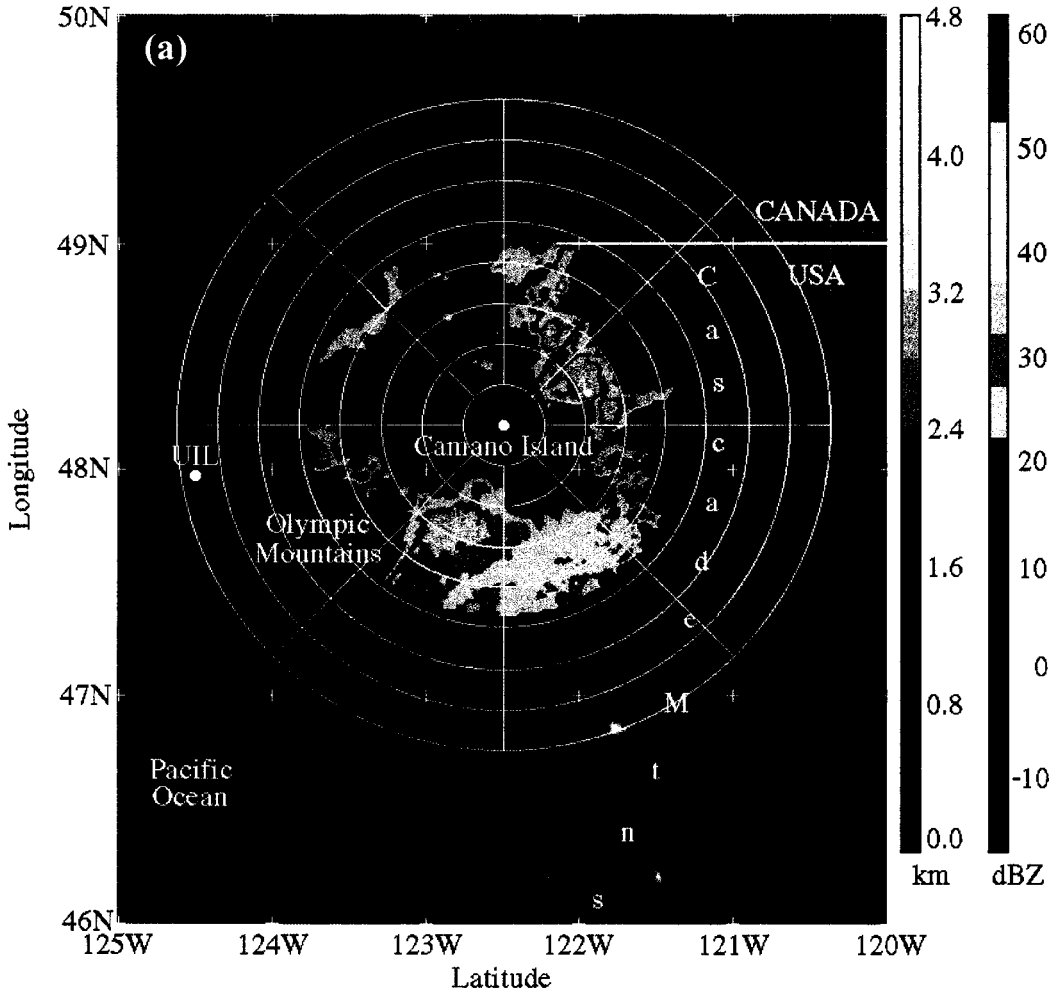

Figure 2.4. Constant altitude plots at 1.5 km MSL using Camano Island WSR-88D (a) reflectivity and (b) radial velocity data from 0931 UTC 23 January 1998. The background topography is shown in gray-scale increments of 0.4 km MSL, with altitudes ≤ 0.0 km shown in steelblue. Range ring spacing is 20 km. Negative radial velocity is used to indicate inbound wind. The red line indicates the direction of the vertical cross section in Fig. 2.5.

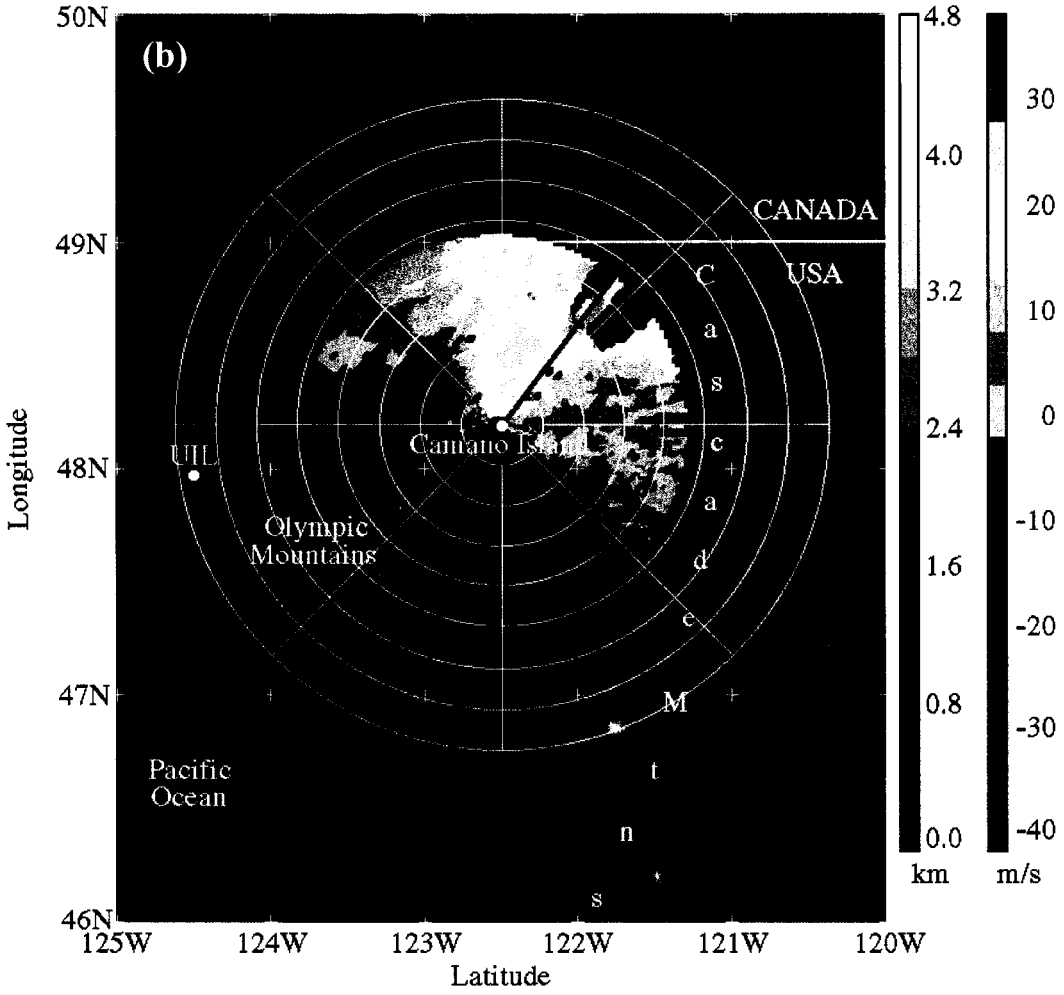

Figure 2.4. (continued)

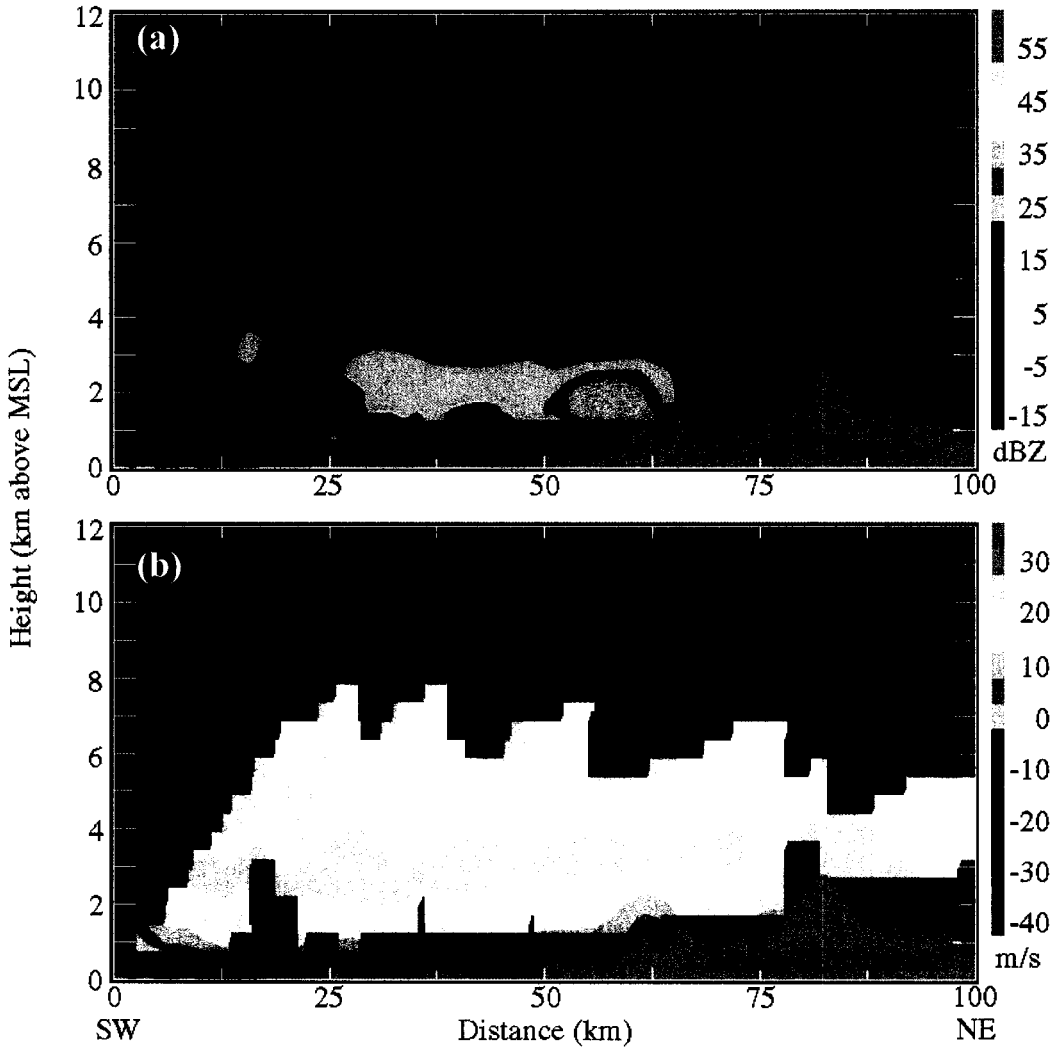

Figure 2.5. Vertical cross sections of (a) reflectivity and (b) radial velocity from southwest to northeast along the red line segment in Fig. 2.4. The vertical profile of the underlying topography is shown in gray.

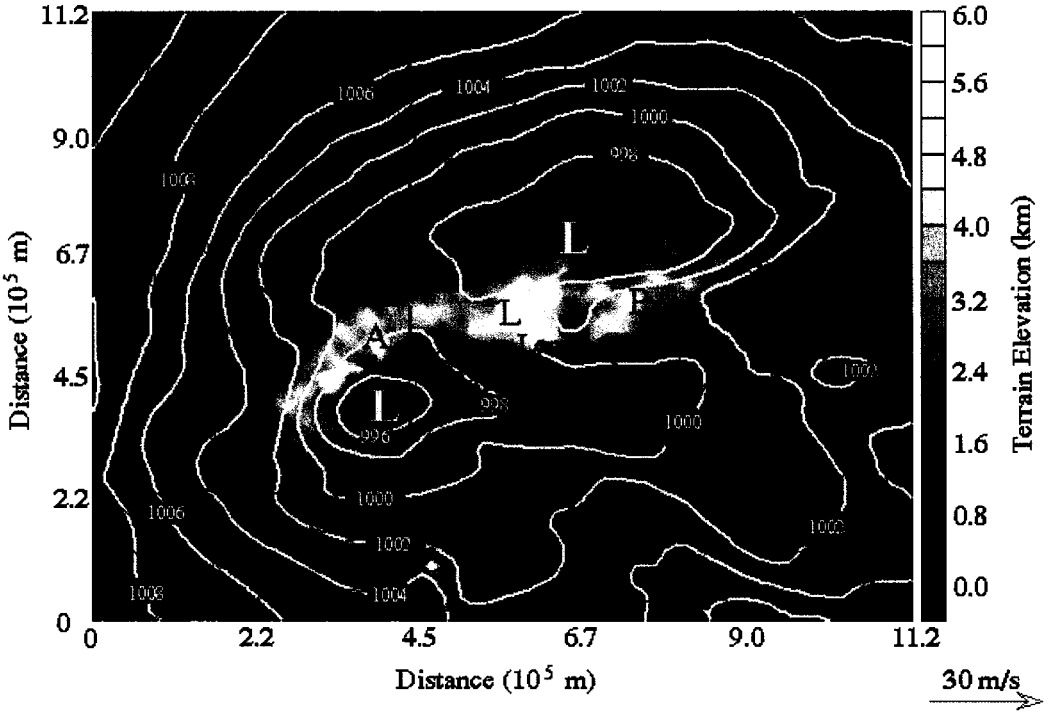

Figure 2.6. The SM forecast of sea level pressure (contours) and 950 mb wind (vectors) valid at 0000 UTC 8 July 1996 (initialized 1200 UTC 7 July). The locations of the Monte Lema radar and Milan, Italy, are shown. The dashed red line indicates the location of the vertical profiles shown in Fig. 2.7.

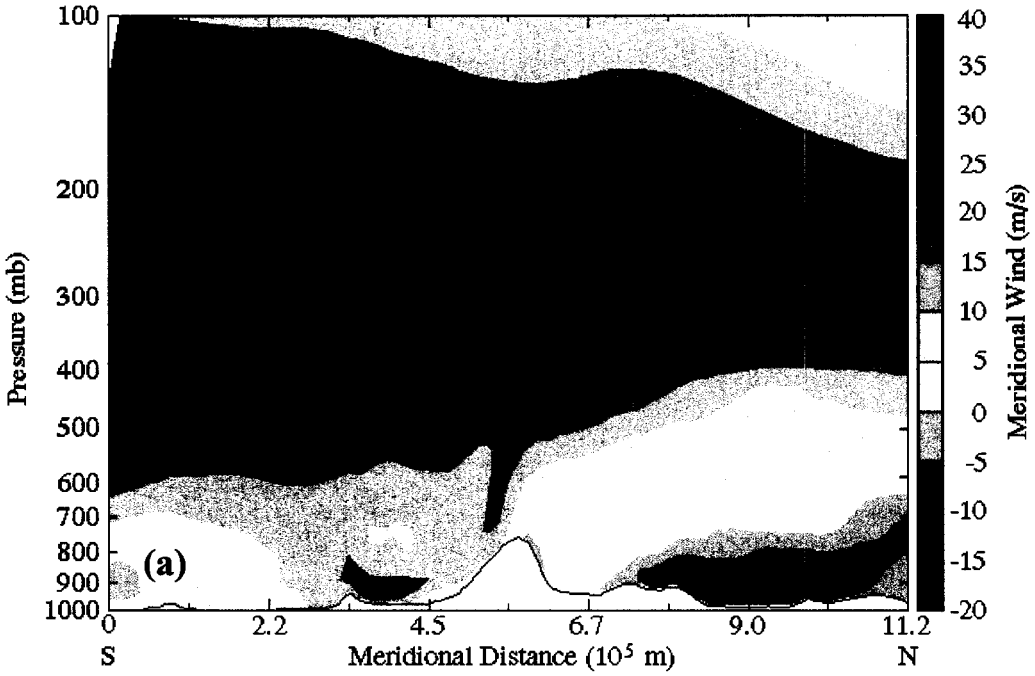

Figure 2.7. Vertical cross section of the SM-simulated meridional wind along the dashed line in Fig. 2.6. Model fields are valid (a) 0000 UTC (initialized 1200 UTC 7 July), (b) 0600 UTC (initialized 0000 UTC 8 July), and (c) 1200 UTC 8 July (initialized 0000 UTC 8 July). Positive (negative) values indicate southerly (northerly) flow.

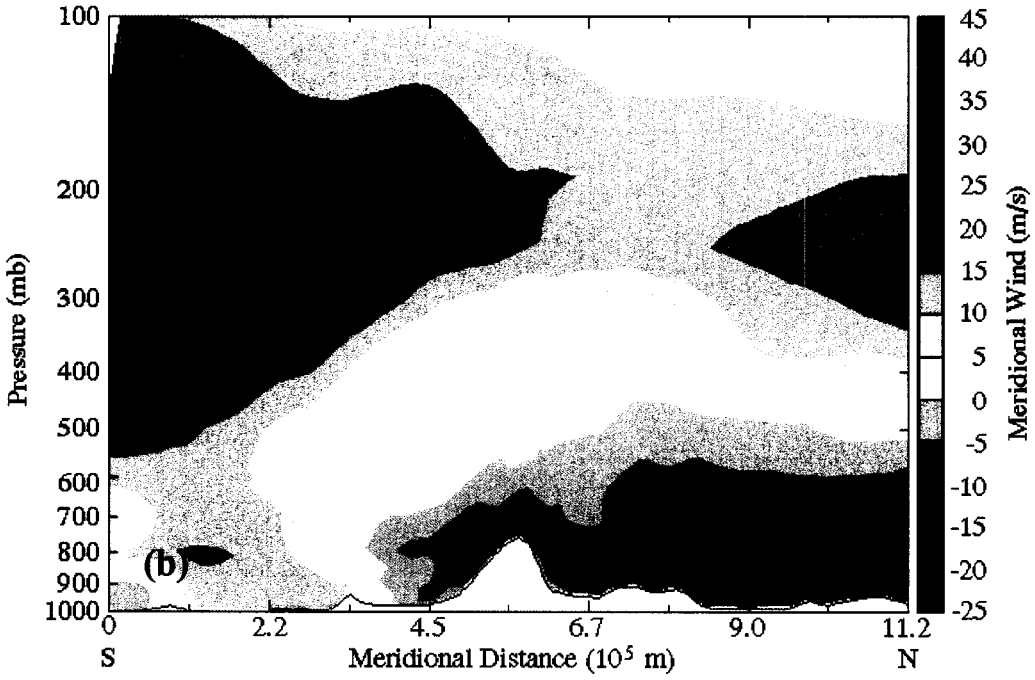

Figure 2.7. (continued)

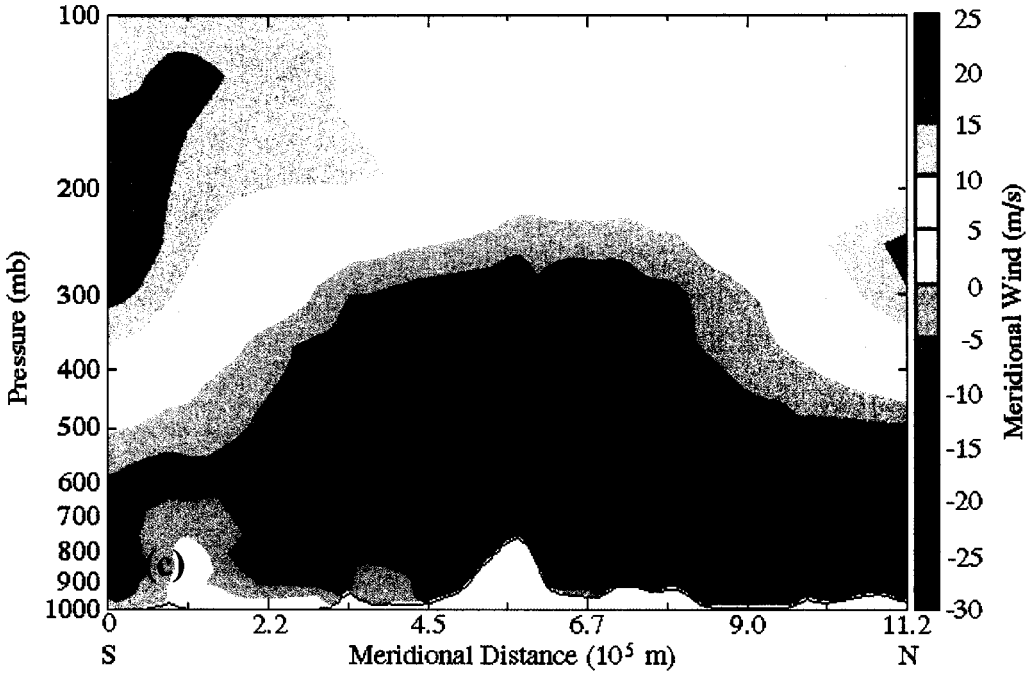

Figure 2.7. (continued)

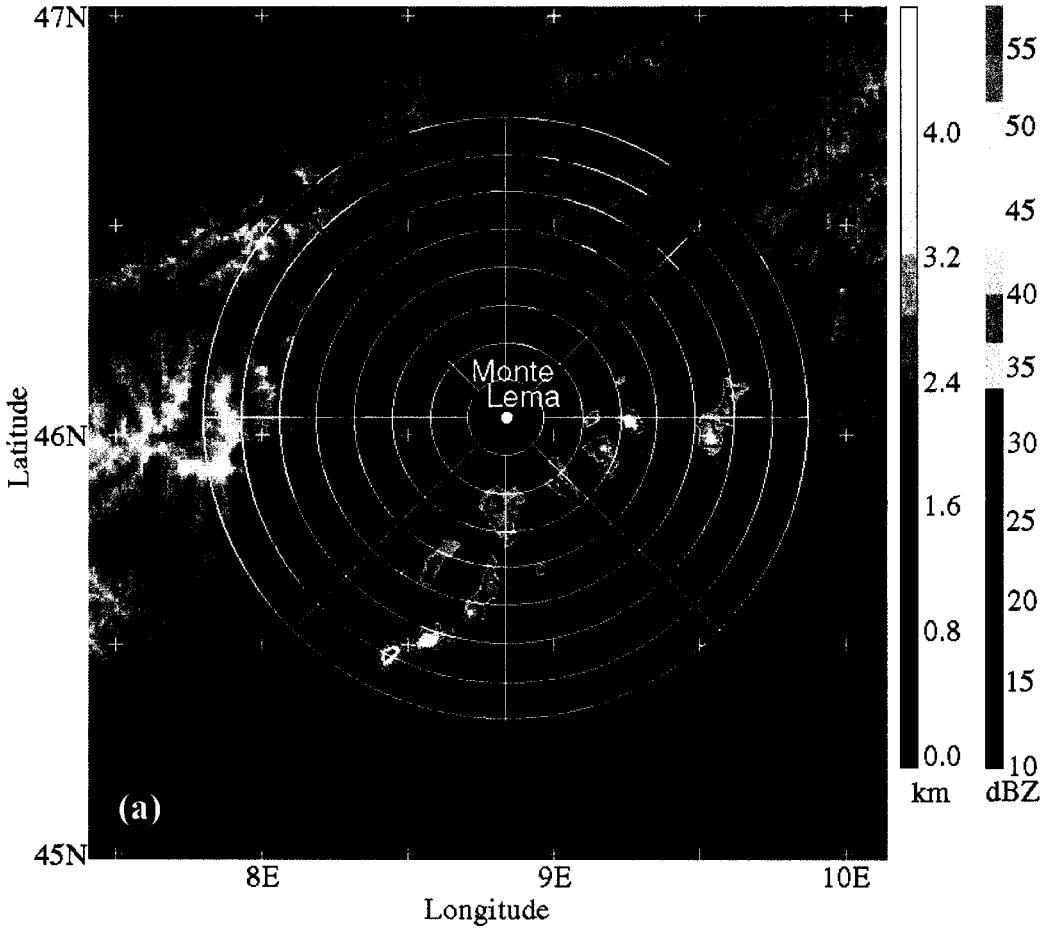

Figure 2.8. MountainZebra horizontal cross sections of (a) radial velocity at 1.5 km MSL and (b) reflectivity at 3.0 km MSL from Monte Lema at 0450 UTC 8 July 1996. The red segment indicates the location of the vertical cross sections in Fig. 10. The range ring spacing is 10 km.

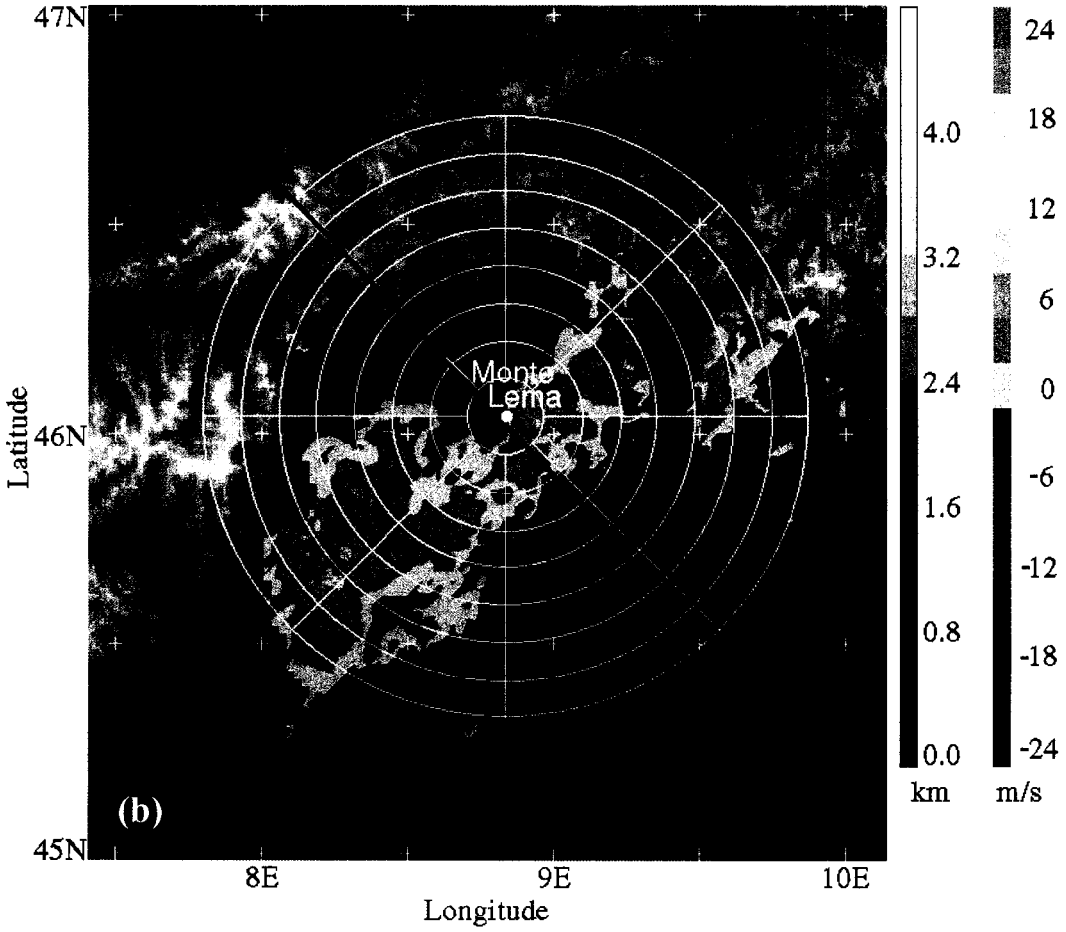

Figure 2.8. (continued)

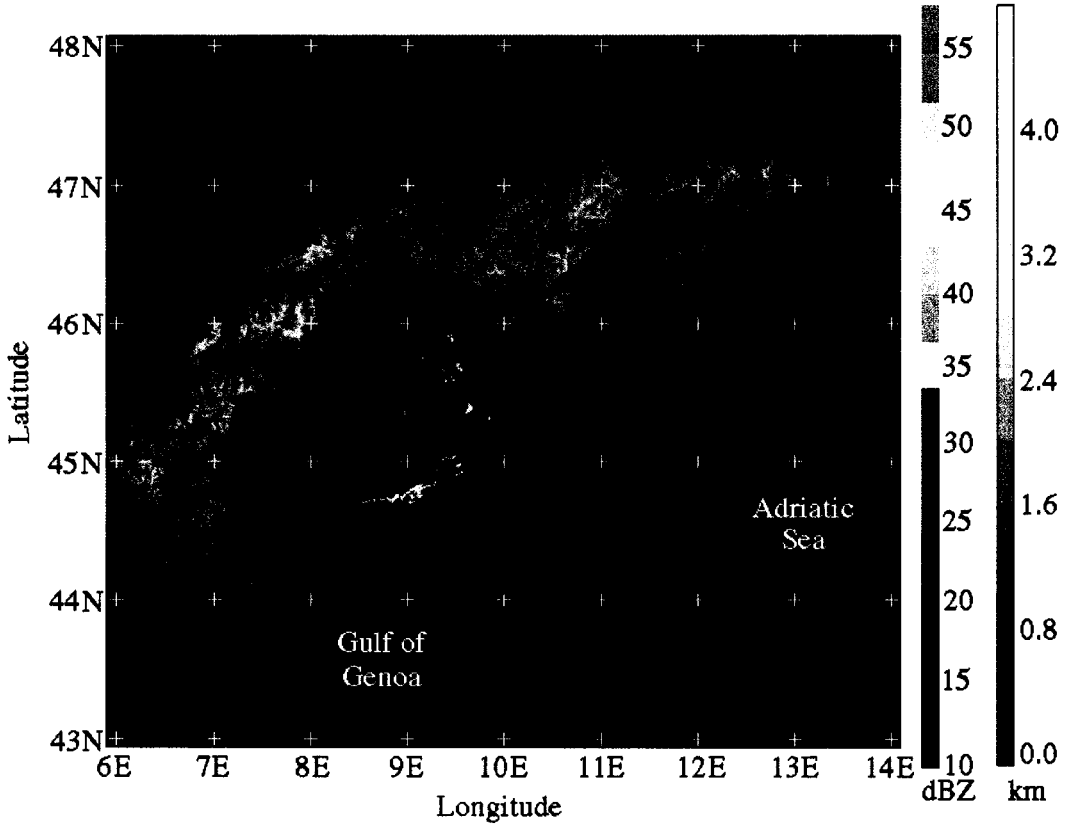

Figure 2.9. MountainZebra horizontal cross section of reflectivity at 3.0 km MSL, 0750 UTC 8 July 1996, indicating the size and position of the lee cyclone in the context of the Alpine topography.

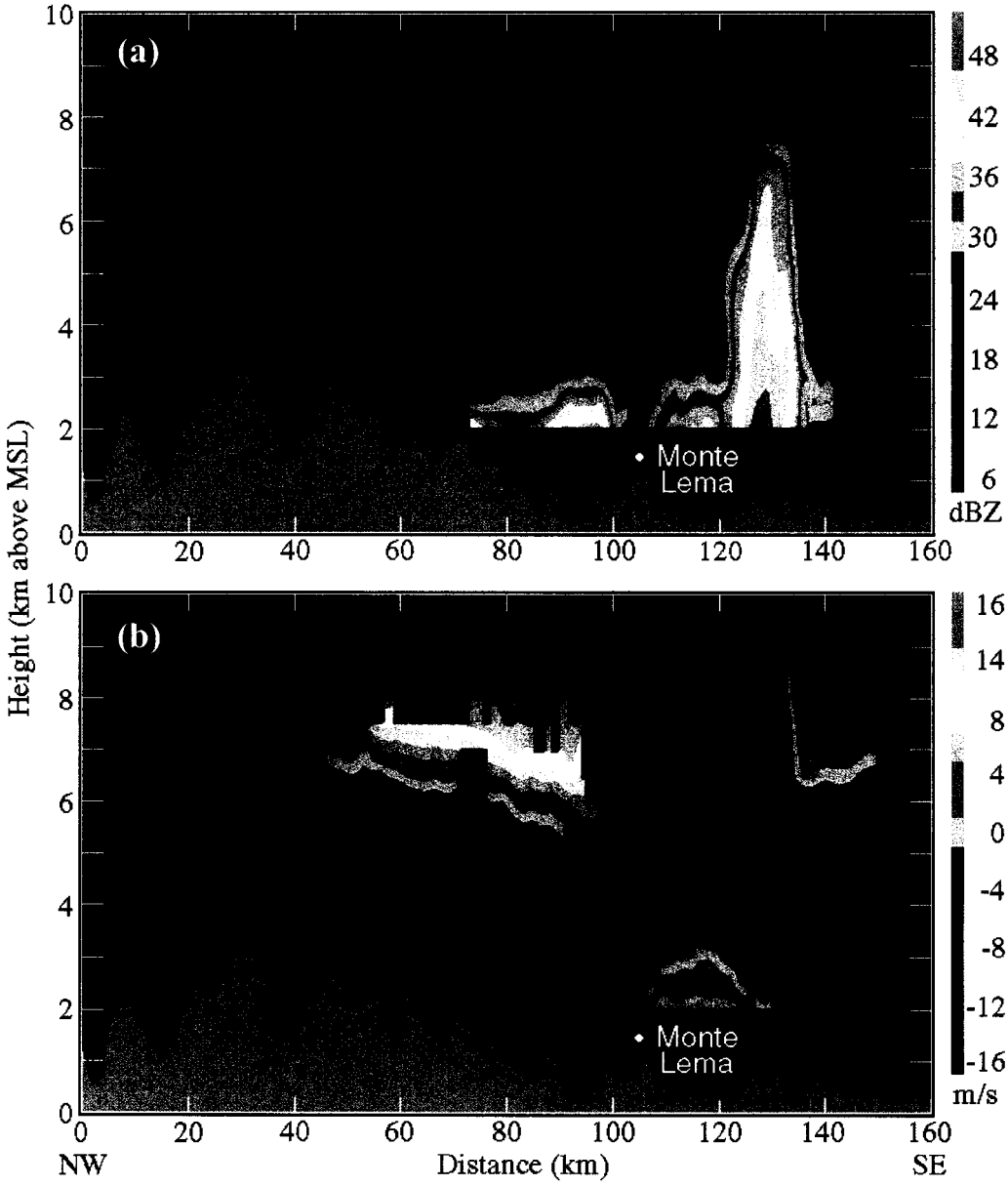

Figure 2.10. MountainZebra vertical cross sections from northwest to southeast of (a) reflectivity and (b) radial velocity obtained from an interpolated 20-tilt volume scan from Monte Lema at 0452 UTC 8 July 1996.

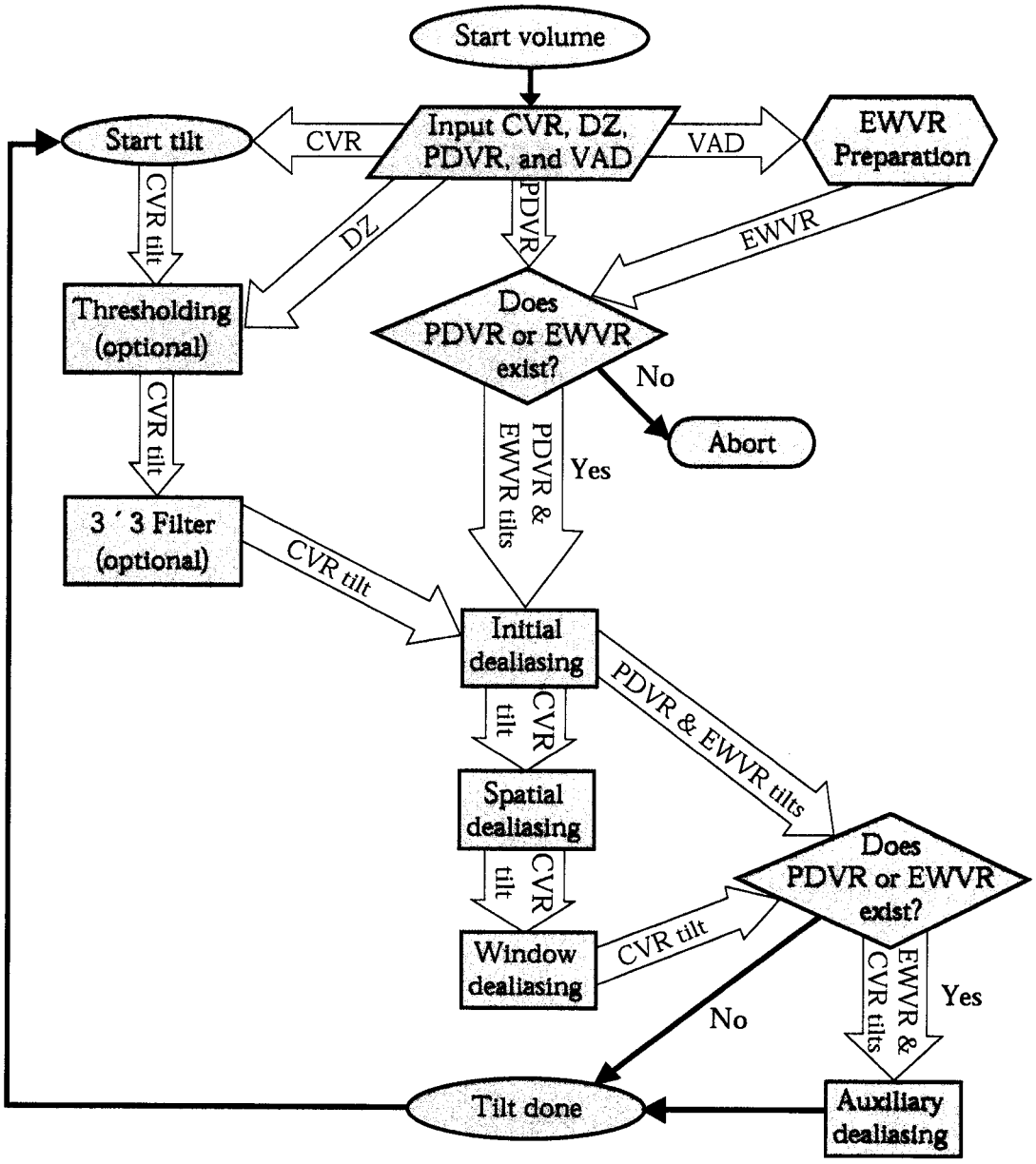

Figure 2.11. Flowchart depicting the processing chain performed on each radar volume by 4DD.

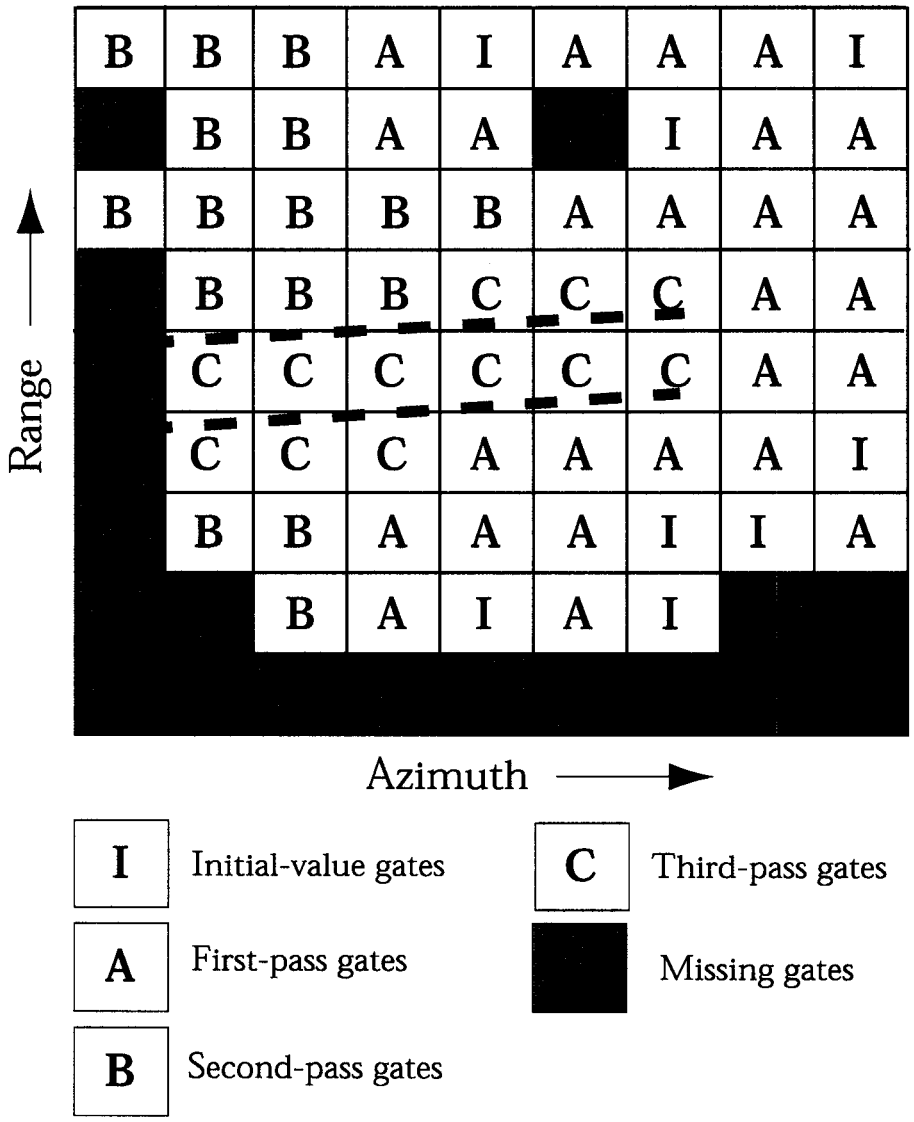

Figure 2.12. The behavior of the spatial dealiasing routine illustrated within a hypothetical 9 × 9 azimuth-range sector. The heavy dashed lines indicate the boundaries of a shear zone with gate-to-gate shears greater than $0.4V_n$. All initial-value gates (i.e., those dealiased during initial dealiasing that are available as initial values for spatial dealiasing) are labeled "I." Gates that are dealiased during the first, second, and third spatial dealiasing passes are denoted "A," "B," and "C" respectively. It should be noted that spatial dealiasing scans radially outward in clockwise (counterclockwise) order during the first and third passes (second pass), and that the shear threshold is relaxed from $0.4V_n$ to $1.0V_n$ before the third pass.

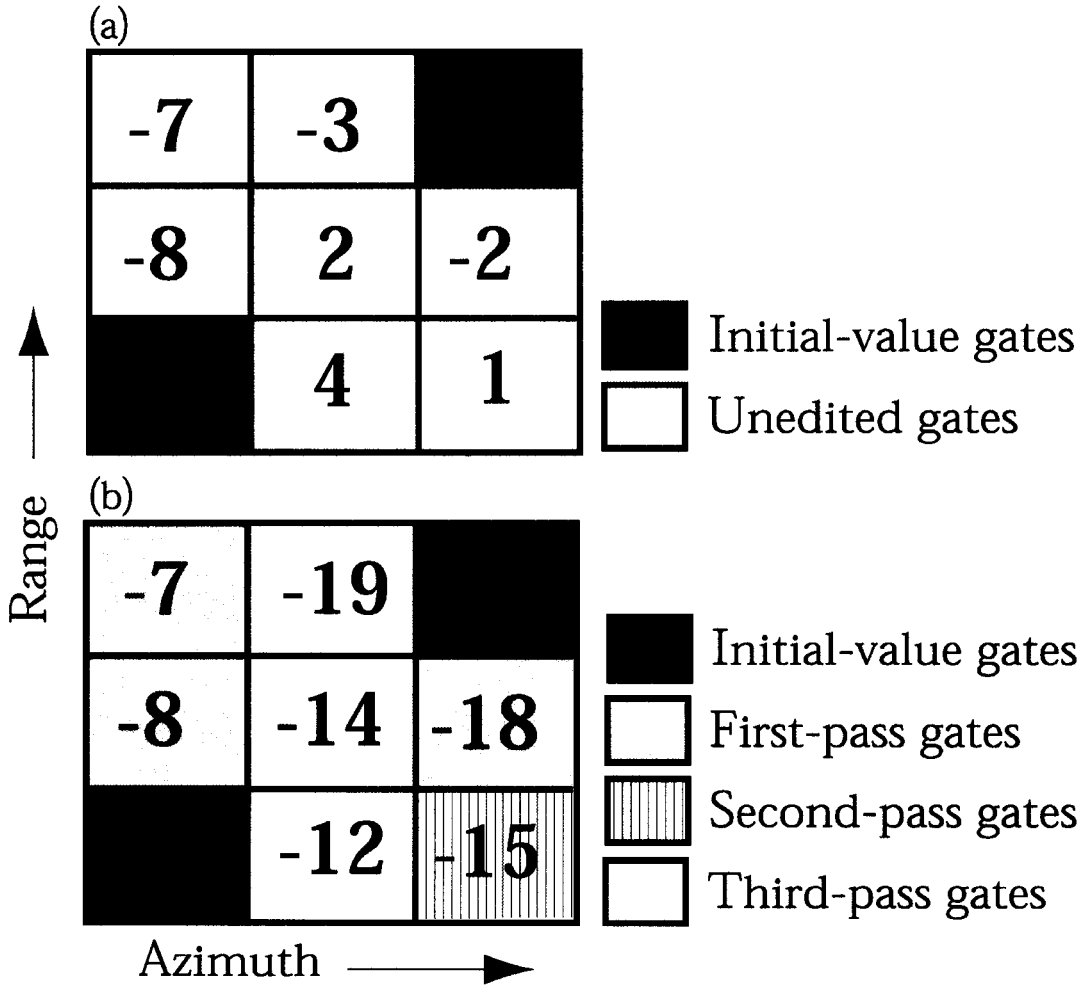

Figure 2.13. Radial velocity values within a hypothetical 3 × 3 radar echo (a) before and (b) after executing the spatial dealiasing routine. In (a), initial-value gates are shaded, while uncorrected gates are not. In (b), initial-value gates are shaded as in (a), while gates corrected during the first, second, and third spatial dealiasing passes contain gradually lighter shading to none.

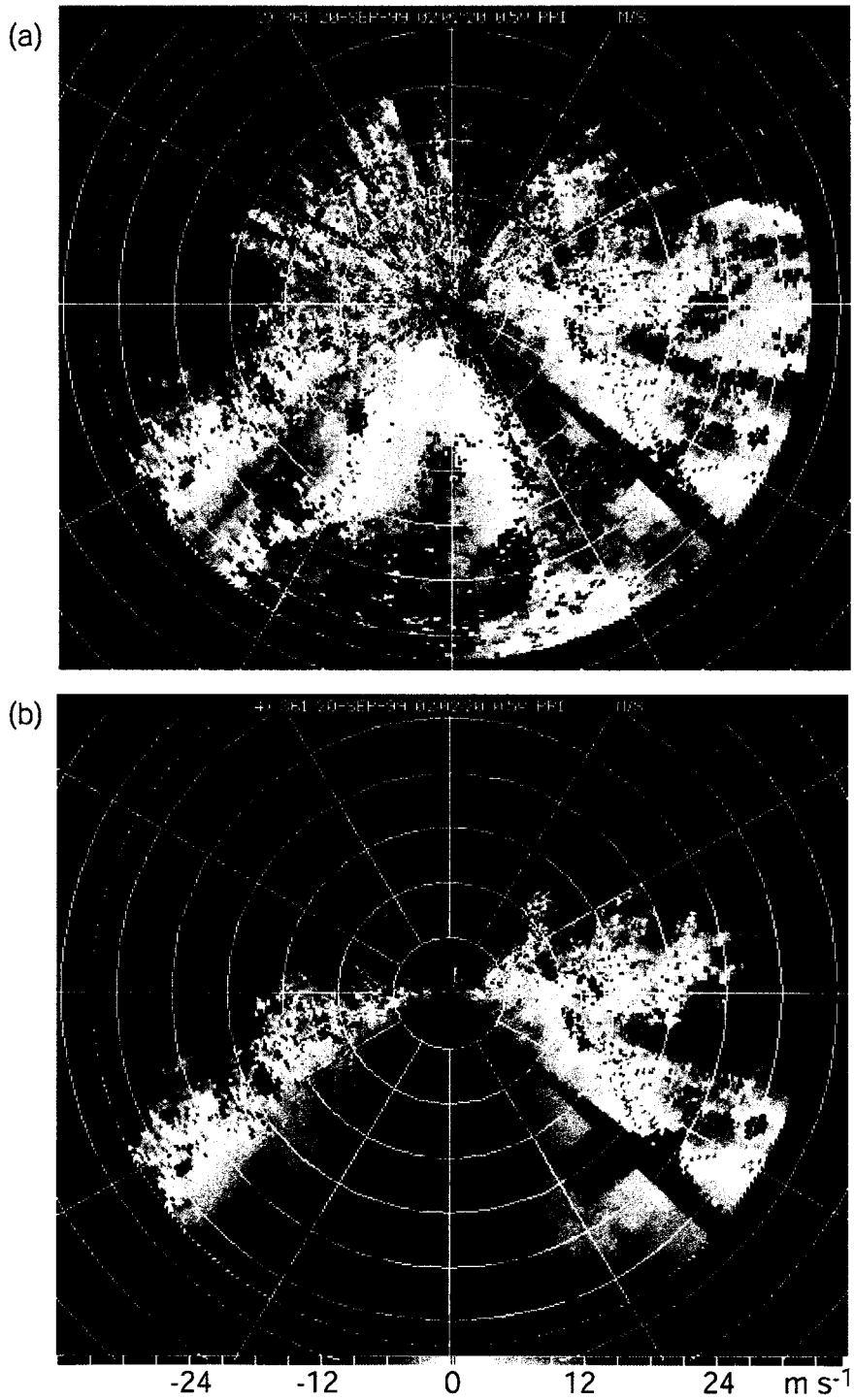

Figure 2.14. A 0.5° radial velocity tilt acquired during MAP at 0202 UTC 20 September 1999 (a) before and (b) after automatic real-time dealiasing via 4DD. The range-ring spacing is 20 km.

CHAPTER 3

THE MEDITERRANEAN SIDE OF THE ALPS[8]

3.1 Background

The European Alps are notorious for heavy rains and floods (Lionetti 1996; Buzzi et al. 1998; Doswell et al. 1998; Ferretti et al. 2000; Rotunno and Ferretti 2001). These events occur primarily in the autumn on the Mediterranean side of the Alps, when moist Mediterranean air ahead of baroclinic waves impinges on the barrier. Orographic air motions modify the baroclinic circulation to produce locally heavy and persistent rain, which runs off rapidly in deep rocky narrow river valleys emptying into the Po Valley of northern Italy. The high Alpine mountain barrier juxtaposed with the Mediterranean moisture source make the region a natural laboratory for studying orographic precipitation. MAP took advantage of these characteristics of the Alps in an investigation of orographic precipitation on the Mediterranean side of the mountain range in autumn 1999 (Bougeault et al. 2001).

Frei and Schär (1998) have analyzed data from rain gauges to map the mean pattern of precipitation over the Alps. Figure 3.1 shows the average pattern for the autumn season in relation to the terrain (solid contour). Prominent mesoscale maxima of rainfall accumulation occur on the southern slopes of the Alps collocated with indentations or concavities in the terrain. These maxima are mesoscale in the sense that they are much smaller than the whole Alpine massif yet much larger than

individual river valleys. At each location, the 800-m MSL terrain contour (thick line) curves inward. The mesoscale rainfall maximum outlined by the rectangle in Fig. 3.1 is the region examined in this study.

Figure 3.2 shows details of the topography within the region of the rectangle. At smaller scales, within each mesoscale maximum, the multiple ridges, peaks and river valleys further modify precipitation and runoff. The mesoscale indentations in the terrain evidently focus the large-scale moist flow over the barrier so as to maximize rain in these regions. The Coriolis force likely influences the flow within these mesoscale indentations but has a negligible effect on more localized flows around smaller-scale peaks, ridges and river valleys.

One of the scientific objectives of the MAP Special Observing Period (SOP), conducted from 7 September through 15 November 1999 in the region shown in Fig. 3.2, was to investigate how the Alpine barrier affects precipitation on a descending cascade of scales from the scale of the entire barrier, to the mesoscale indentations of the barrier, to individual ridges, peaks and river valleys (Houze et al. 1998). For the SOP, seven ground-based research radars and two aircraft-borne radars collected data on the Mediterranean side of the Alps. The ground-based radar network was configured to sample the mesoscale precipitation within the area enclosed by the rectangle in Figs. 3.1 and 3.2. This area is hereafter referred to as the Lago Maggiore region.

---

[8] Sections 3.1 and 3.2 are adapted from Houze et al. (2001).

As a precursor study, the author examined rain events that occurred in the Lago Maggiore region during autumn 1998, one year before the MAP SOP (Houze et al. 2001). The purpose was to explore the mesoscale precipitation climate of the region in further detail and provide insight that could be applied to field operations. A description of this experiment is given in Section 3.2, the early findings of which were made available to MAP researchers prior to the SOP. Then, Section 3.3 discusses how these findings were implemented into research operations and how they compare with results obtained in the field.

3.2 Preliminary climatological study

The primary data source for the preliminary study was the Swiss Meteorological Institute's Doppler weather radar located at the top of Monte Lema (altitude = 1.63 km, Fig. 3.2). The radar provided four-dimensional fields of radar reflectivity (a metric of the precipitation intensity) and radial velocity (an indicator of the airflow producing the precipitation) in high resolution over the entire autumn 1998 MAP season, one year before the SOP.

The data were examined climatologically (statistically) rather than by cases to obtain the most general picture possible of the airflow and precipitation processes at work in this critical region. Sounding data were used to characterize the upstream conditions and to stratify the data by Froude number, wind speed and stability. Specifically, the objective of this study was to use superposed epoch (i.e. composite) analysis of the radar data to help establish the relative importance of

these parameters in determining the orographic modification of the precipitation produced by the storms affecting the Lago Maggiore region.

3.2.1 Data and methods

3.2.1.1 The Monte Lema radar

Joss et al. (1998) describe the C-band Monte Lema radar in detail. It is an operational radar, and the elevation angle (tilt) sequence is fixed and includes 20 tilts per 5-min period. The reflectivity data undergo rigorous quality control within the radar processor. A decision tree algorithm consisting of a reflectivity threshold, a wide-band noise threshold, a Doppler velocity threshold, two statistical filters, a vertical reflectivity gradient test and a clutter map was incorporated to classify echoes as either clutter, system noise or precipitation. The technique removed virtually all of the reflectivity gates containing noise or terrain backscatter that could adversely affect statistical computations in this study. Nevertheless, as with other radars, terrain shadowing, bright band contamination, increasing sample volume size with range, attenuation and wet radome effects are potential sources of error when interpreting the data (Joss et al. 1998; Doviak and Zrnić 1993; Houze 1993).

Because the Monte Lema radar operates with a Nyquist velocity of only 8.27 m s^{-1}, the radial velocity field contained extensive aliasing (Chapter 2; Doviak and Zrnić 1993). Over 5,000 individual three-dimensional volumes of radar data were used, making it impractical to dealias the data by hand. 4DD was therefore utilized to successfully dealias the radar volumes with only occasional errors

(Chapter 2; James and Houze 2001). Even in extreme events, these errors were generally very localized and were so few as to have a minimal effect on the statistical results of this study.

Data volumes from all precipitation events in the Lago Maggiore region from 1 September through 30 November 1998 were recorded every 5 min. Following four-dimensional dealiasing, the time interval between volumes was increased from 5 min to 1 h to reduce the autocorrelation between volumes and ease data storage requirements. The result was a downsizing of the data archive from more than 5,000 radar volumes to 554 volumes. The remaining volumes were then bilinearly interpolated to a Cartesian grid with a resolution of 2 km · 2 km · 0.5 km using NCAR's SPRINT software (Mohr and Vaughan 1979) and finally converted to Unidata's Network Common Data Format (NetCDF) for visualization (Chapter 2; James et al. 2000).

The Monte Lema radar antenna is located at an altitude of 1.63 km MSL. The 2-km level is about the lowest available grid level that can be obtained using bilinear interpolation. In addition, the bilinear interpolation cannot produce an estimate of the conditions beyond a range of about 60 km, where the lowest radar tilt (-0.3°) usually rises above the 2-km level due to the earth's curvature. Therefore, results are only available at or above the 2-km level and out to a range of 60 km.

3.2.1.2 Calculations based on the radar data

Following the procedures outlined in the Appendix, seasonal mean reflectivity, rain rate and radial velocity were computed for autumn 1998. Superposed epoch analyses, with corresponding Student-*t* difference-of-means significance tests, were also computed. The most informative *t*-statistic results are included in the horizontal radar maps and will be discussed where relevant in Section 3.2.3.

3.2.1.3 Variables characterizing the upstream flow

Meteorological epochs during autumn 1998 were stratified by characteristics of the upstream flow. The flow into the region of precipitation observed by radar was sampled every six hours by radiosonde measurements from the Milano-Linate Airport (labeled "Milano" in Fig. 3.2). From these data, wind direction, wind speed, static stability and Froude number were calculated to characterize the environment immediately upstream of the radar-observed area. The values of these variables defined data subsets used in the superposed epoch analysis. Each variable was represented by its average value within the 925-700 hPa layer (corresponding roughly in altitude to 0.75-3 km MSL) in the sounding. If no sounding was available within 3 h of a radar volume time stamp, the volume was not used for those superposed epoch analyses that required sounding information. Sounding information was available for only 480 of the 554 radar volumes.

The Froude number is $F = U/(NH)$, where U is the upstream flow speed, N is static stability and H is the height of the mountain barrier. The characteristic ele-

vation of mountain passes along the north side of the Lago Maggiore region warranted a scale height of H = 2.5 km MSL. Superposed epoch analyses were based on the flow strength, static stability and Froude number for southerly and southeasterly flow events (specifically, those in which the direction of the mean flow in the 925-700 hPa layer was between 112.5 and 202.5° azimuth). The moist Brunt-Väisälä frequency (Durran and Klemp 1982) was computed using finite differences over the 925-700 hPa layer, consistent with the fact that this study considers only cases of precipitation seen by radar. Even if the upstream Milano sounding was less than saturated, the air was assumed to be saturated by the time it was producing rainfall over the Alps. Experiments assuming dry or moist Brunt-Väisälä frequency based on a humidity threshold (e.g. Mass and Ferber 1990) led to erratic results.

3.2.2 Overall average patterns of radial velocity and reflectivity

3.2.2.1 Mean radial velocity pattern

Figure 3.3 shows the mean radial velocity field for the autumn 1998 season. This figure indicates that the prevailing wind direction at 2-km MSL during precipitation events was south-southeasterly, and its magnitude was 4-6 m s^{-1}. A similar wind pattern was later observed during the MAP SOP, except that the flow at 2 km was stronger and more easterly. Other MAP radars indicated easterly flow at lower altitudes during the SOP (Houze et al. 2001). A change from easterly to southerly with increasing height at low levels was a characteristic of the Piedmont

flood on the Mediterranean side of the Alps in November 1994 (Buzzi et al. 1998; Doswell et al. 1998; Ferretti et al. 2000; Rotunno and Ferretti 2001).

The predominance of southeasterly flow at 2 km, as indicated by the radial velocity field in Fig. 3.3, agrees with a longer-term rawinsonde climatology compiled by Kappenberger and Kerkmann (1997) for autumn precipitation events over the Lago Maggiore region. They found that the synoptic setting most favorable for precipitation over the Lago Maggiore region was southwesterly flow at 500 hPa, ahead of an approaching upper-level trough, while at 850 hPa the wind directions ranged from east through south to southwest. Inspection of the average Monte Lema radial velocity field at higher levels (not shown) indicates that the wind veered with height during precipitation events in the Lago Maggiore region, becoming southwesterly at 5-km MSL, consistent with Kappenberger and Kerkmann's climatology.

3.2.2.2 Mean radar reflectivity pattern

Figure 3.4a shows the mean rainfall rate field derived from the Monte Lema radar data for the 2-km MSL level for September-November 1998, which is consistent with observations during the MAP SOP (Houze et al. 2001). It is also consistent with the rain-gauge-based climatology of Frei and Schär (1998; Fig. 3.1) but provides additional local detail plus three dimensionality. A vertical cross section through the mean reflectivity field (Fig. 3.4b) is consistent with the results of Frei and Schär (1998) in that the maximum precipitation occurred over the windward

slopes of the Alpine range ($x = 25 - 40$ km in Fig. 3.4b) rather than over the highest terrain. The melting level was nearly always between 2 and 3 km. The radar bright band may have caused the altitude of maximum reflectivity implied by radar to be located somewhat higher than its actual location on the windward slope, but still well below the maximum height of the Alpine barrier (~4 km). The maximum reflectivity in the vertical cross section occurred between $x = 25$ and $x = 40$ km on the horizontal axis (Fig. 3.4b). Terrain clutter may have caused some slight overestimation of the radar echo intensity as a result of residual clutter or side lobe echoes in this region; however, the Swiss Meteorological Institute's intensive quality control of the raw data (Sec. 3.2.1.1) all but eliminates this possibility. Echoes occurring downstream, over the highest peaks ($\sim x = 10$ km) and upstream over the Po Valley, were of consistently lower intensity. The vertical cross section of precipitation frequency (Fig. 3.4c), defined as the percentage of volumes in which the reflectivity equaled or exceeded 13 dBZ, was also maximum on the lower windward slopes, where the average reflectivity (Fig. 3.4b) was maximum; hence this maximum was not a transient feature but a robust characteristic throughout the season.

The vertical cross section of reflectivity (Fig. 3.4b) also indicates that the maximum reflectivity consistently occurs at low altitude, below ~4 km MSL. This altitude is approximately the height of the highest terrain downstream. This persistent feature of the echo pattern indicates that the precipitation particles form, grow

and fall out quickly and efficiently over the lower slopes of the Alpine barrier, with most of the precipitation particle growth occurring at low levels. The height of the 0°C isotherm in this season was typically 3-km MSL or lower. The echo maxima extend above this height. Therefore, the precipitation growth mechanisms are not entirely warm coalescence of liquid drops. These results suggest that ice evidently also plays a role in the growth. Further studies of the MAP SOP data have shed light on these low-level growth mechanisms over the lower windward slopes of the terrain (see Section 3.3).

3.2.3 Reflectivity and velocity patterns by epoch[9]

3.2.3.1 Rain distribution as a function of direction of impinging flow

As mentioned in Section 3.1, the terrain curves inward over the Lago Maggiore region. Figure 3.5 indicates the influence of the concave shape of the topography on the precipitation in relation to the upstream wind direction (after Houze et al. 2001). The individual panels of this figure present the radar data for both the autumn 1998 and 1999 seasons according to the average wind direction in the 925 – 700 hPa layer, as computed from the Milano soundings (Sec. 3.2.1.3). For each wind-direction category (east, southeast, south, and southwest), the panels on the left show the distribution of radar-derived rain rate while the panels on the right show the *t*-statistic of the rain pattern (computed as described in the

[9] Since the data acquired during the autumn 1999 MAP SOP are in general agreement with the autumn 1998 season, the data for the two years have been merged in the analyses described in the remainder of this chapter after Houze et al. (2001).

Appendix). Each panel also shows the 800-m MSL topographic contour. This contour indicates both the fine-scale pattern of ridges and valleys in the lower portion of the Alps and the broader outline of the mesoscale concave indentation of the Alps surrounding the Lago Maggiore region (cf. Figs. 3.1 and 3.2). The contour lies generally east, north, and west of the Monte Lema radar, with the lowland region of the Po Valley lying to the south. Thus, winds over this region from the east, southeast, south, and southwest each encounter rising terrain.

Figure 3.5a shows the rain rate field at 2 km for the easterly flow cases (wind direction between 67.5 and 112.5°), which favor upslope enhancement of precipitation over the western slopes of the mountains surrounding the area covered by the radar. The statistical significance of this result is shown by the field of the *t*-statistic of the rain rate at the 2-km level (Fig. 3.5b). The red areas, where $t > 1.96$, indicate where the sample mean is significantly above the seasonal mean. Blue areas, where $t < -1.96$, indicate where the sample mean is significantly below the seasonal mean. Over most of the domain, the precipitation rate was not significantly different from the seasonal climatology. Rates were significantly above the seasonal mean over some regions to the west, where the flow was upslope, and significantly below over a few slopes of the eastern side, where the flow was downslope. The composite for southeasterly flow (112.5-157.5°, Fig. 3.5c) shows intense precipitation over most of the domain with a statistically significant precipitation increase over the western slopes and over the Po Valley (Fig. 3.5d). The cases with

southerly flow (157.5-202.5°, Figs. 3.5e and 3.5f) had intense, significantly increased precipitation over all the lower slopes of the Lago Maggiore area. Comparison of figure panels 3.5c and 3.5e indicates that both southeasterly and southerly flow produced large orographic enhancement of rainfall on the lower slopes of the Alps, with southerly flow providing the strongest upslope component. In southwesterly flow, precipitation was below the seasonal mean, especially in the western portion of the radar domain, evidently because of drier downslope flow (Figs. 3.5g and 3.5h).

3.2.3.2 Froude number

From Section 3.2.3.1 it is evident that the southeasterly and southerly cases are associated with the most intensely orographically enhanced precipitation. Therefore, the Froude number analysis will be restricted to cases within these two epochs.

The Froude number combines the influences of stability, wind speed and terrain height. It indicates whether or not the flow has enough kinetic energy to rise over the barrier (Durran 1990; Chapter 12 of Houze 1993). It therefore suggests whether or not the orographic lifting will occur directly over the terrain or upstream. High Froude number flow rises easily over a mountain barrier and robust upslope flow occurs, which can enhance precipitation over the windward side of a mountain barrier and increase spillover to the lee of the barrier. When low Froude

number flow is blocked by the terrain, lifting and enhancement of rainfall can occur upstream of the barrier (e.g. Grossman and Durran 1984).

Figure 3.6 shows the fields of rain rate and *t*-statistic at the 2-km level for the Froude number composite analyses. These patterns contain all radar data obtained when the flow into the Lago Maggiore region, as measured by the Milano sounding, was southeasterly or southerly and not blocked ($F > 1$, Figs. 3.6a and 3.6b) and blocked ($F < 1$, Figs. 3.6c and 3.6d). The *t*-statistic calculations show that when the Froude number was high, the precipitation rates over the foothills, lower slopes and western Po valley were significantly stronger.

When the Froude number was low, the precipitation rates were very close to the climatology, with a suggestion of blocking far upstream. This upstream blocking is evidenced by higher rainfall rates and *t*-statistic calculations near the southeast corner of the radar domain at a range of about 80 km from the radar. The Alpine crest is located 60 km to the north and northwest of the radar site. The characteristic horizontal scale over which the effects of blocking occur in the case of statically stable low Froude number flow is the Rossby radius of deformation, or

$$L_R = NHf^{-1} \tag{3.1}$$

where N is the moist Brunt-Väisälä frequency and H is the characteristic barrier height. The average value of N was about 0.008 s^{-1} when the Froude number was <1. Using the same value of H as for the Froude number calculations (2.5 km) and $f = 1.05 \times 10^{-4}$ s^{-1} for 46°N latitude, $L_R \approx 190$ km. The occurrence of upstream

enhancement at a distance of 140 km of the barrier crest is thus consistent with theory.

If the upstream Froude number computed from sounding data truly indicates whether or not the low-level flow is blocked, the radial velocity field observed by radar should be consistent with relatively unimpeded upslope flow in the high Froude number cases, as well as with blocking in the low Froude number cases. The lowest level available in the Monte Lema radar data is 2-km MSL (Sec. 3.2.1.1). The flow direction at this level tended toward a more southerly direction in the high Froude number cases (Fig. 3.7a) and toward a more southeasterly direction in the low Froude number cases (Fig. 3.7b). This directional difference would be consistent with the impinging flow at lower Froude number turning cyclonically as it approached the barrier, as would be expected in a blocking scenario. However, it is only a slight directional difference and could indicate different synoptic patterns between blocked and unblocked cases. Also, the strength of the flow is comparable for the two cases and unblocked at the 2-km level. The effect of blocking was apparently felt below 2 km.

Low-altitude radar measurements at 0.5 km MSL later obtained during the MAP SOP (autumn 1999) confirmed this suspicion (Houze et al. 2001). High Froude number flow at 0.5 km was upslope and nearly perpendicular to the barrier axis, while low Froude number SOP cases exhibited 0.5-km northeasterly flow and down-valley flow within individual river valleys, in response to blocking by the

barrier (Steiner et al. 2000; Houze et al. 2000). Houze et al. (2001) also showed that at low altitudes over the Po Valley, well upstream from the Monte Lema radar and the Alps, the precipitation was enhanced during the blocked cases.

The Froude number $F = U/(NH)$, and hence the tendency toward blocking or not, depends on both strength and stability of the flow. To separate these two influences, the Froude number composites were subdivided according to the wind speed (Fig. 3.8; after Houze et al. 2001). The cases with upstream wind speed > 8 m s^{-1} had the heaviest precipitation on the lower windward slopes of the Alps, especially northwest of the radar (Figs. 3.8c and 3.8g). The mean upstream wind speed U and moist Brunt-Väisälä frequency N were calculated for all cases. The upstream wind speeds for the two strong flow cases were comparable (11 m s^{-1}), hence any difference in the patterns was due to the stability. Very stable cases constitute the $F < 1$ strong-flow epoch ($N = 8.7 \times 10^{-3}$ s^{-1}) and thus produce the blocking signal observed well upstream from the Alps during the SOP (Houze et al. 2001). Much less stable cases constitute the $F > 1$ strong-flow composite ($N = 1.0 \times 10^{-3}$ s^{-1}), and the air stream easily rose over the terrain. The t-statistic showed significantly enhanced rain rates both over and out to about 40 km upstream of the lower slopes of the Alps (red area in Fig. 3.8d).

In contrast to the strong flow cases, the weak flow composites (upstream wind speed 0 – 8 m s^{-1}) have very little precipitation (Figs. 3.8a and 3.8e). The corresponding t-statistic fields indicate that the precipitation over the lower slopes

of the Alps was significantly suppressed in these cases (see the blue patches over the lower slopes in both Figs. 3.8b and 3.8f). The mean wind speed for the two weak-flow regimes was comparable (~5.5 m s^{-1}). The extremely low mean stability for the higher Froude number ($F > 1$) weak-flow case ($N = 0.2 \times 10^{-3}$ s^{-1}) evidently accounted for isolated patchy (probably convective) precipitation over the Po Valley just upstream of the slopes (Figs. 3.8a and 3.8b). The lower Froude number ($F < 1$) weak flow case (Fig. 3.8e) was very stable ($N = 7.6 \times 10^{-3}$ s^{-1}) and it produced barely any precipitation.

3.2.3.3 Diurnal cycle

Figure 3.9 shows the total radar-estimated rainfall over the Lago Maggiore region for each hour of the day for autumn 1998. A prominent maximum was observed between 0700 and 1000 LST (0600 and 0900 UTC). A maximum occurred during the same time of day during the SOP in autumn 1999 but was not as prominent (Houze et al. 2001). If the synoptic patterns had coincidentally produced stronger or more frequent lifting during the morning hours during these two particular years, this diurnal cycle could merely reflect a sampling fluctuation of the radar data. However, a physical basis might exist for such a maximum. The mean rainfall rate for 0700 – 1000 LST during the 1998 MAP season (Fig. 3.10) was spatially maximized in a contiguous region extending about 80 km from Lago Maggiore toward the southeast (outlined by the dashed elliptical contour). In this region, a number of deep Alpine river valleys empty into the larger Po Valley dur-

ing the morning hours when the atmosphere is most stable. It was therefore speculated prior to the SOP that morning drainage flow from the river valleys converged with the synoptic-scale flow over the Po Valley and thus enhanced the upward air motion and precipitation within the Lago Maggiore region. Further evidence to support this hypothesis was later obtained during the SOP (see Section 3.3).

3.2.4 Summary of findings

During the autumn season in the Lago Maggiore region heavy rains and floods can occur when baroclinic waves bring Mediterranean air into northern Italy at low levels. Whenever this air impinges on the Alpine massif there is the potential for a major rain or flood event. This preliminary study utilized Doppler-radar data to reveal the detailed three-dimensional climatology of precipitation structure and accompanying airflow during autumn 1998. The radar reflectivity and Doppler radial velocity patterns shown in Figs. 3.3 and 3.4 are in close agreement with what was later observed during the MAP SOP (Houze et al. 2001). One important implication of this result is that the MAP season (Bougeault et al. 2001) was generally representative of autumn rainfall on the Mediterranean side of the Alps.

Consistent with previous studies of rain gauges in the Alps (Frei and Schär 1998), the radar reflectivity was generally largest over the lower windward slopes and decreased toward higher terrain. Vertical cross sections of the mean three-dimensional reflectivity show that precipitation generally developed at low alti-

tudes, with most of the precipitation growth occurring at altitudes below the Alpine crest.

Superposed epoch analyses of the Doppler-radar data collected in the Lago Maggiore region during autumn 1998 (supplemented with data from autumn 1999 after Houze et al. 2001) indicate that there is a clear relationship between the upstream flow direction and the intensity of precipitation over the Lago Maggiore region. These analyses further show the role of the perpendicularity between the local topography and the air stream. Over the Lago Maggiore region the precipitation was significantly greater when the wind direction around the 2-km level was southerly or southeasterly. The rainfall over the lower slopes rapidly dropped off when the flow became either easterly or westerly. When the southerly and southeasterly flows had a high Froude number, the flow proceeded directly up and over the terrain, and the precipitation was greatly enhanced over the lower windward slopes and over the portions of the Po valley just upstream of the mountains. In extreme cases, this type of flow can lead to flooding in the Alps (Buzzi et al. 1998; Doswell et al. 1998; Ferretti et al. 2000; Rotunno and Ferretti 2001). With low Froude number southerly and southeasterly flows were strongly blocked below the 2-km level (Houze et al. 2001). However at higher elevations the air stream rose over the terrain fairly easily. Thus, the enhancement of precipitation directly over the lower mountain slopes was denied the participation of the air in the lowest 2 km, which turned eastward in response to blocking. Apparently the lifting of the

low-level air stream was shifted upstream, as precipitation enhancement occurred ~140 km (approximately one Rossby radius) upstream of the barrier crest in the blocked cases.

Composite analysis indicates that the speed of the flow strongly affected whether or not orographic enhancement of the precipitation occurred on the lower windward slopes of the Lago Maggiore region. The role of stability was to influence the location of the precipitation with respect to the topography. When the flow was strong and the stability low, the precipitation was greater over the lower slopes of the Alps and plains close to the mountains. During strong and very stable flow conditions (blocked case), the precipitation was also enhanced but some of the enhancement occurred upstream of the Alps. When the flow was weak the precipitation was in general equal or slightly below the mean, except for the low stability case, when there was some enhancement in the form of patchy cells over the Po valley.

Most of the physical interpretation of the climatological behavior of the Doppler-radar data in this study as a function of upstream wind speed and stability and perpendicularity to the terrain derives from simple basic principles. Stronger wind and lower stability favor flow rising easily over terrain, with most of the precipitation enhancement occurring directly over the lower slopes of the terrain (Figs. 3.8c and 3.8d).

If the stability is low enough, further enhancement may occur by the release of buoyant instability (Figs. 3.8a and 3.8b). Higher stability favors blocking, which shifts some of the orographic lifting upstream of the mountain barrier (Figs. 3.8g and 3.8h). These basic principles are discussed ideally in pedagogical references on orographic precipitation (e.g. Smith 1979; Houze 1993). The same principles have been used in various combinations to explain the specific behavior of the Alpine orographic precipitation leading to the famous Piedmont flood of November 1994 (Buzzi et al. 1998; Doswell et al. 1998; Ferretti et al. 2000; Rotunno and Ferretti 2001). This chapter shows how these straightforward basic principles clearly relate to the overall average behavior of the orographic precipitation on the Mediterranean side of the Alps. Moreover, the radar climatology shows that the orographic enhancement is extremely sensitive to the basic upstream flow properties on the detailed scale of the Lago Maggiore region. The upstream flow speed and stability evidently determines whether heavy rains will be directly over the slopes or will be partially shifted upstream, over the Po Valley. Rather slight differences in prevailing upstream wind direction determine on which side of the convex indentation of the Alpine terrain bounding the Lago Maggiore region the heaviest rains and runoff will occur.

Finally, a diurnal precipitation maximum occurred between 0600 and 0900 UTC over the Lago Maggiore region. To produce this maximum, one may speculate that down-valley flow inside deep river valleys emptying into the larger Po

Valley and converging with the synoptic-scale flow in the Po Valley was maximum in the early morning when the air was most stable.

3.3 The MAP SOP

3.3.1 Field operations

The findings detailed above for autumn 1998 (Sect. 3.2; Houze et al. 2001) provided insight into the Alpine precipitation climate and were tested during the MAP SOP (autumn 1999). At that time, two additional ground-based scanning radars, the U.S. NCAR S-Pol and the French RONSARD, were situated in the Po Valley and aligned with the operational radar at Monte Lema in a roughly south-southwest to north-northeast orientation (Bougeault et al. 2001; Fig. 3.2). These three radars surveyed the four-dimensional characteristics of precipitation, micro-physics and airflow over the Lago Maggiore region. Other ground-based research radars such as the mobile Doppler on Wheels (DOW) sampled the precipitation and flow at finer scales within individual river valleys. In addition, research aircraft added more detailed Doppler radar and in situ measurements overhead.

A Project Operations Center (POC; Bougeault et al. 2001) was established at the Milano-Linate airport in northern Italy to coordinate operations between multiple observing platforms. From the POC, scientists guided research operations using both forecast model guidance and real-time observations. Live data streams from various radar sites were reformatted, edited, interpolated and displayed using MountainZebra (Chapter 2; James et al. 2000), which the author helped configure

for the POC. Aircraft positions were obtained through radio communication and manually entered into Zebra (Corbet et al. 1994) by the author, and the resulting flight tracks were superposed with the radar data. Thus, real-time imagery was available at the POC containing radar fields, flight tracks, and terrain. The displays enabled POC scientists to guide research operations and thus achieve orographic precipitation research objectives (Bougeault et al. 2001).

The author also wrote various software scripts that automatically captured imagery from MountainZebra and uploaded the images via ftp to the MAP Field Catalog (www.joss.ucar.edu/map/catalog/). The catalog was made available to the scientific community for both real-time and post-SOP analysis. Figure 3.11 presents a sample graphical product that was updated to the catalog every 10 minutes. The image contains a composite of aircraft flight tracks and reflectivity from multiple ground-based radars, providing a "quick look" at where aircraft were positioned in relation to precipitation.

Figure 3.12 presents another product that was available in real-time at the POC, which displayed reflectivity with horizontal wind vectors and vertical velocity over the terrain. This three-dimensional airflow and reflectivity depiction was achieved every 15 minutes through the synthesis of multiple Doppler radar data when precipitation was occurring in the Lago Maggiore region. To the author's knowledge, MAP was the first field experiment of its kind to achieve multiple Doppler syntheses in real time (Chong et al. 2000; Chapter 2). These syntheses

provided MAP scientists with insight into the complex three-dimensional airflow in the Lago Maggiore region. The author provided initial motivation for this effort and configured 4DD (James and Houze 2001; Chapter 2) to operate on the Monte Lema data stream. Without 4DD, reliable multiple Doppler syntheses could not have been achieved in real time over the greater Lago Maggiore region, because it was the only available algorithm that could dealias the Monte Lema radar's low Nyquist velocity (8.27 m s^{-1}) scans effectively.

The MAP Field Catalog (www.joss.ucar.edu/map/catalog/) also stores online mission summaries that were generated by the POC Science Director at the conclusion of each Intensive Observing Period (IOP). These summaries contain HTML code, text, and figures contributed by the author.

3.3.2 Relevant findings

A wide variety of precipitation events occurred in the Lago Maggiore Region during MAP. The observations obtained in the field confirmed that orographic precipitation strongly depends on characteristics of the impinging flow, as summarized in Section 3.2.4. For example, Houze et al. (2001a) illustrate the importance of atmospheric stability and Froude number in their comparative study of IOP2b (19-21 September 1999) and IOP8 (20-21 October 1999). Both storms corresponding to IOP2b and IOP8 exhibited strong (~15 m s^{-1}) southeasterly flow above the 900-mb level (analogous to Fig. 3.5c), yet IOP2b had much heavier precipitation accumulation over the Lago Maggiore region. The IOP8 storm was a

very stable case (corresponding to Fig. 3.8g), with weak flow below 900 mb. IOP2b, on the other hand, had potential instability and stronger flow into the region (similar to Fig. 3.8c).

Houze et al. (2001a) found that the unblocked flow in IOP2b, despite background stratiform precipitation, exhibited deep lifting of the air over the lower windward slope of the Alps, with coalescence growth and deeper echoes over the first Alpine peaks. Fig. 3.13a exhibits the deeper vertical extent of reflectivity 40 km northwest of the S-Pol radar during IOP2b, compared to IOP8 (Fig. 3.13b). At that same location, graupel was observed during IOP2b (Fig. 3.13c) amid strong radially outbound flow that rose easily from near the surface and up over the terrain (Fig. 3.13e).

However, IOP8 had lighter mainly stratiform precipitation upstream from the peaks, as evidenced by bright banding and layered echoes within 40 km range of the S-Pol radar (Fig. 3.13b; Houze et al. 2001a). Polarimetric data indicate mainly ice crystal deposition growth and fallout during IOP8 (Fig. 3.13d), although graupel was observed at fine scales as the result of turbulent shearing motions over blocked low-level flow (not shown; Houze and Medina 2004).

Fig. 3.13f depicts the weak near-surface blocked flow, which was northwesterly during IOP8 and denied rich low-level moisture from rising over the Alpine slopes. This return flow was observed during several MAP IOPs by the DOW, which was deployed to the Toce and Ticino River valleys of the Lago

Maggiore region. During stable upslope flow events, the DOW observed persistent down valley flow in a shallow surface layer less than 2-km deep (Steiner et al. 2000; Houze et al. 2000). Airborne Doppler radar observations from MAP also show a blocked return flow response at low altitudes during stable events that opposes the larger-scale upslope flow and enhances lifting (Bousquet and Smull 2001). Because atmospheric stability is generally stronger within a shallow surface layer in the morning hours, these observations may explain the diurnal precipitation pattern that was observed in the Lago Maggiore region prior to MAP (Sect. 3.2.4).

Medina and Houze (2003) developed the conceptual model in Fig. 3.14, integrating observations from IOP2b and IOP8. The model generalizes the orographic precipitation mechanisms that occurring in blocked v. unblocked flow. In Chapter 4, this conceptual model is tested for the more stable climate of coastal Northern California. Further research using MAP data archives will lead to additional insight into the details of orographic precipitation that can also be generalized and applied to other mountainous climates.

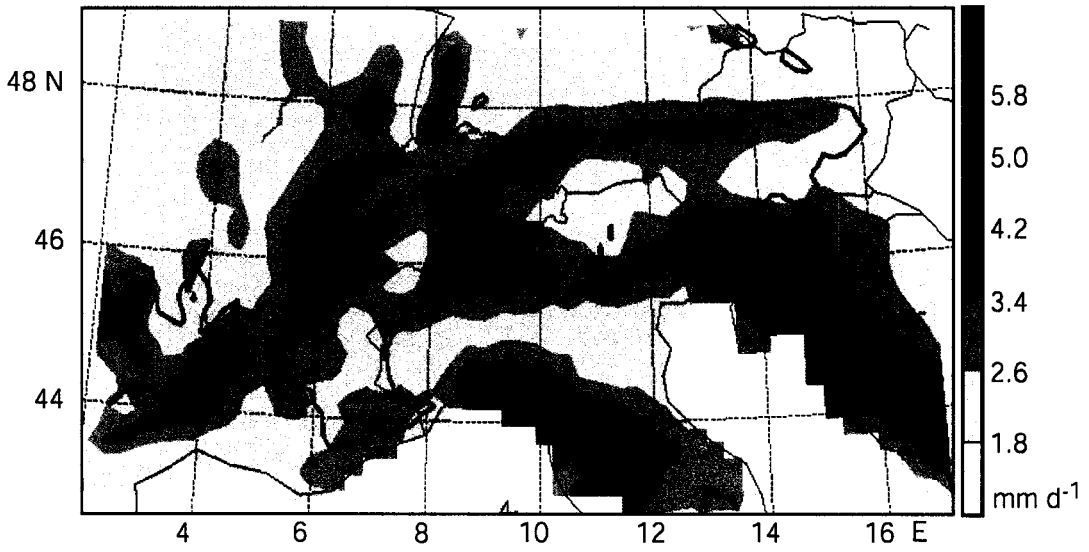

Figure 3.1. Mean Alpine precipitation during September – November for 1971 – 1990. Thick lines indicate the 800-m MSL terrain contour. The MAP Northwest Target Area (rectangle) is also shown (After Frei and Schär 1998.)

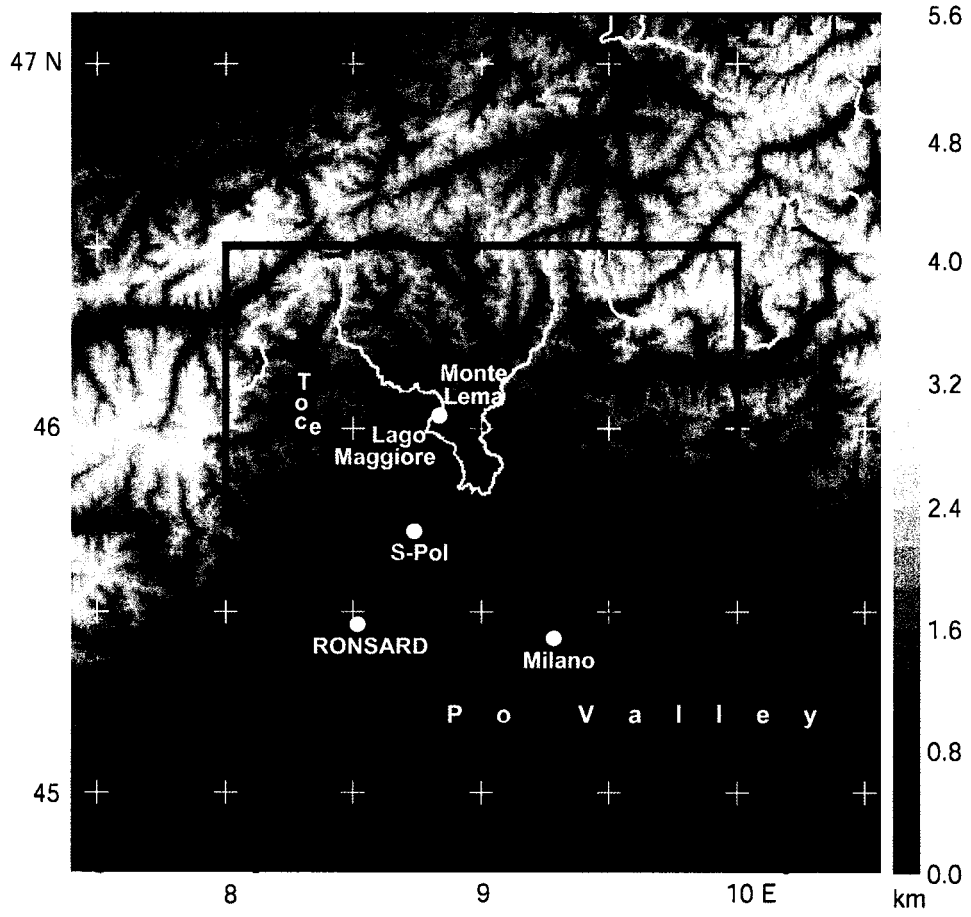

Figure 3.2. The MAP Northwest Target Area (rectangle). The Swiss-Italian border (white contours), bodies of water (thin contours), geographic features and MAP radar locations are also shown.

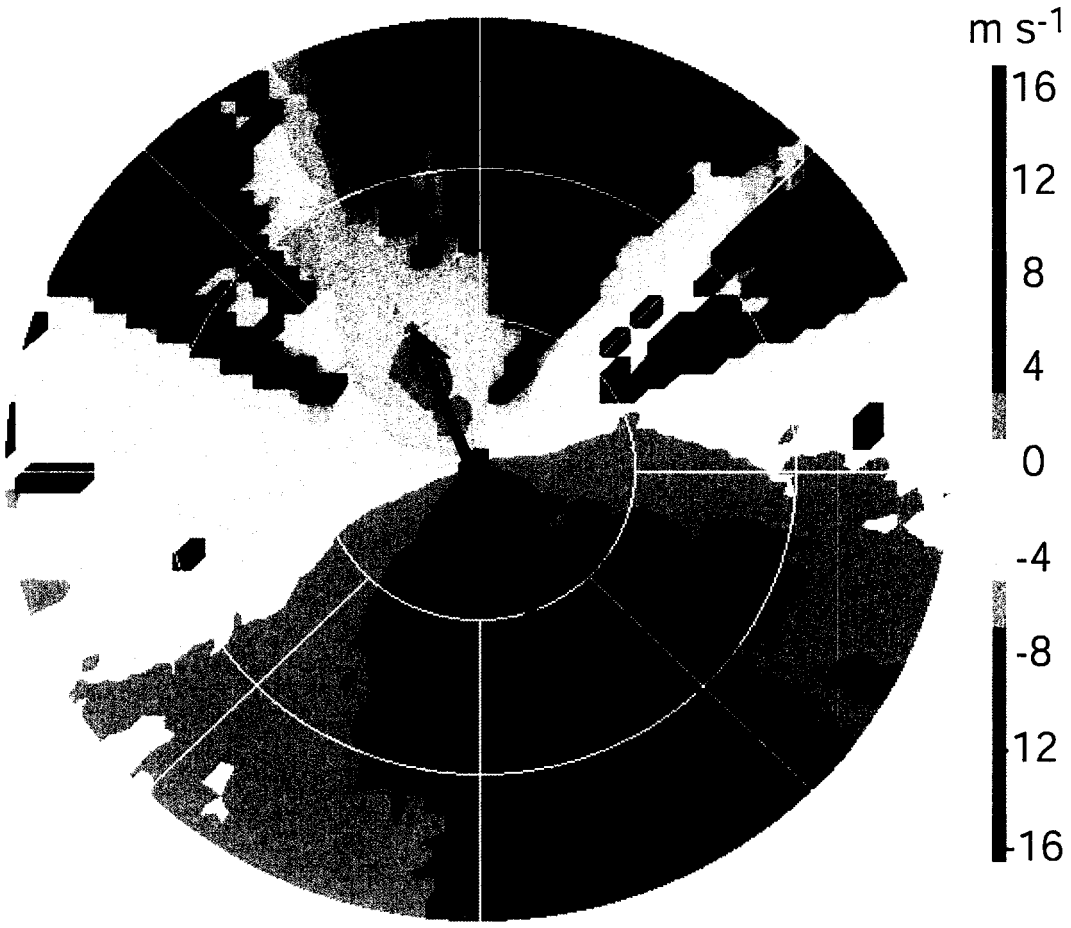

Figure 3.3. Constant altitude plot (2.0 km MSL) containing the mean radial velocity during all precipitation events observed by the Monte Lema radar (autumn 1998; 554 radar volumes included in calculation). The range ring spacing is 20 km. Note that by Swiss convention, negative (positive) radial velocities denote outbound (inbound) flow. The arrow indicates the flow direction at the radar site.

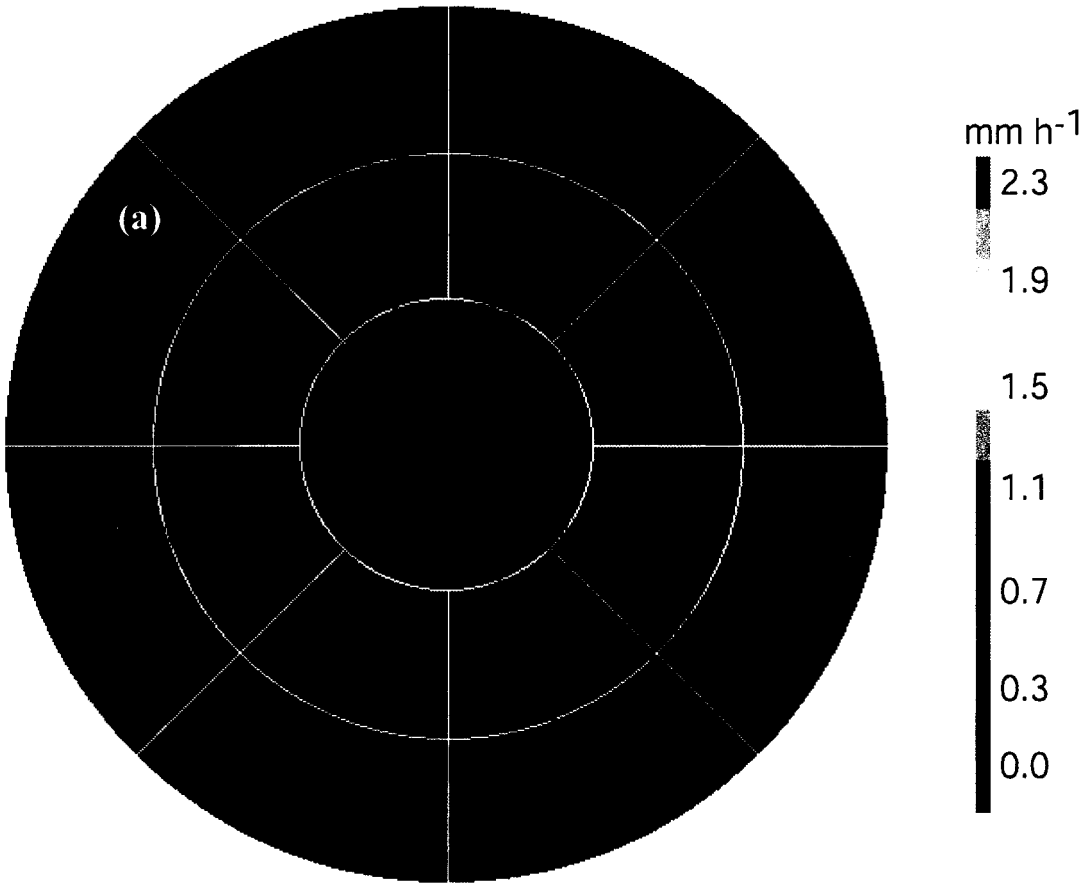

Figure 3.4. (a) Constant altitude plot at 2-km MSL containing the mean radar-derived rainfall rate observed by the Monte Lema radar during all precipitation events (autumn 1998; 554 radar volumes included in calculation). Range ring spacing is 20 km. Vertical cross section along the red line segment in (a) depicts (b) radar-derived reflectivity and (c) precipitation frequency (i.e. the percentage of volumes for which the reflectivity $\geq$ 13 dBZ at each grid point).

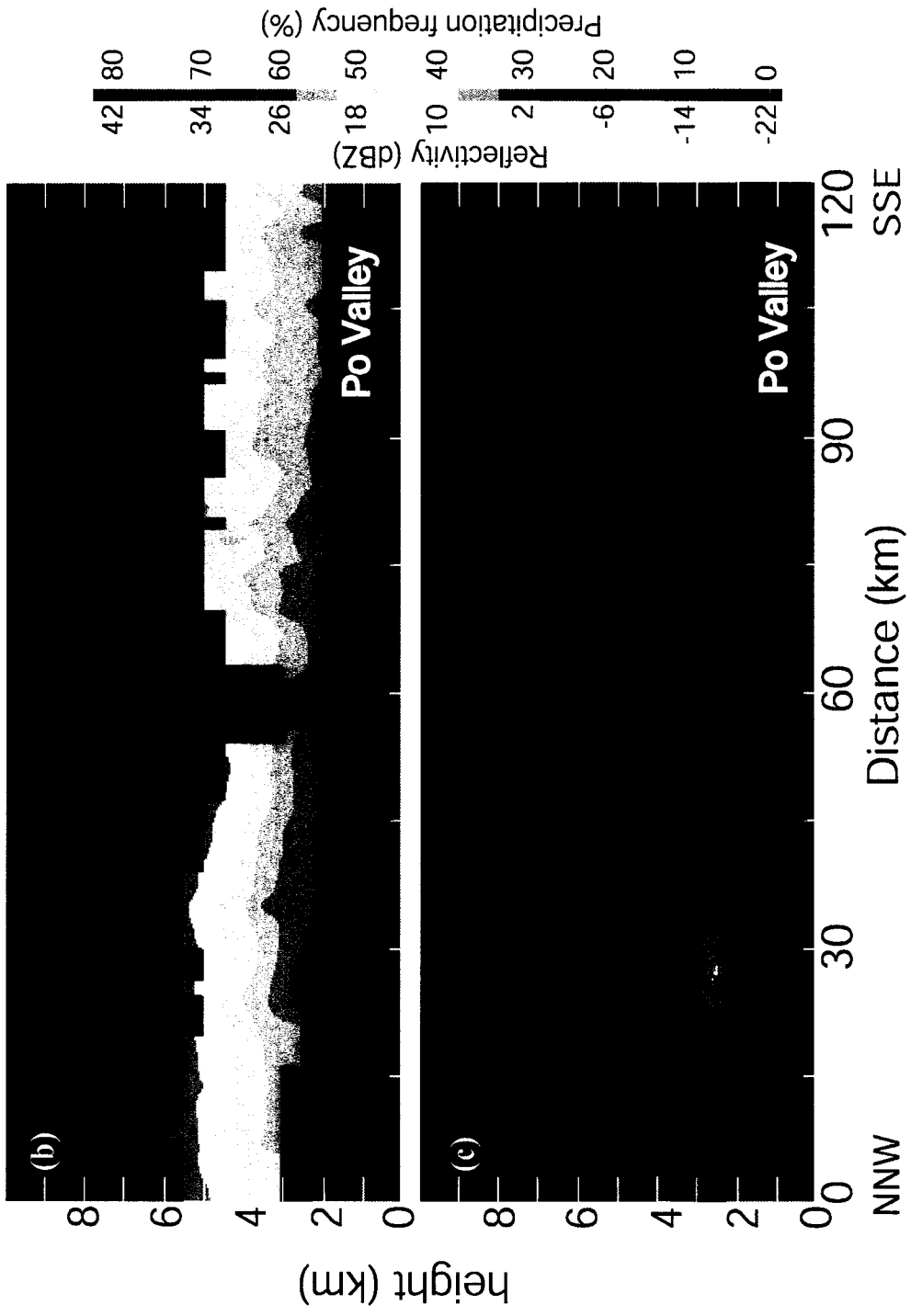

Figure 3.4. (continued)

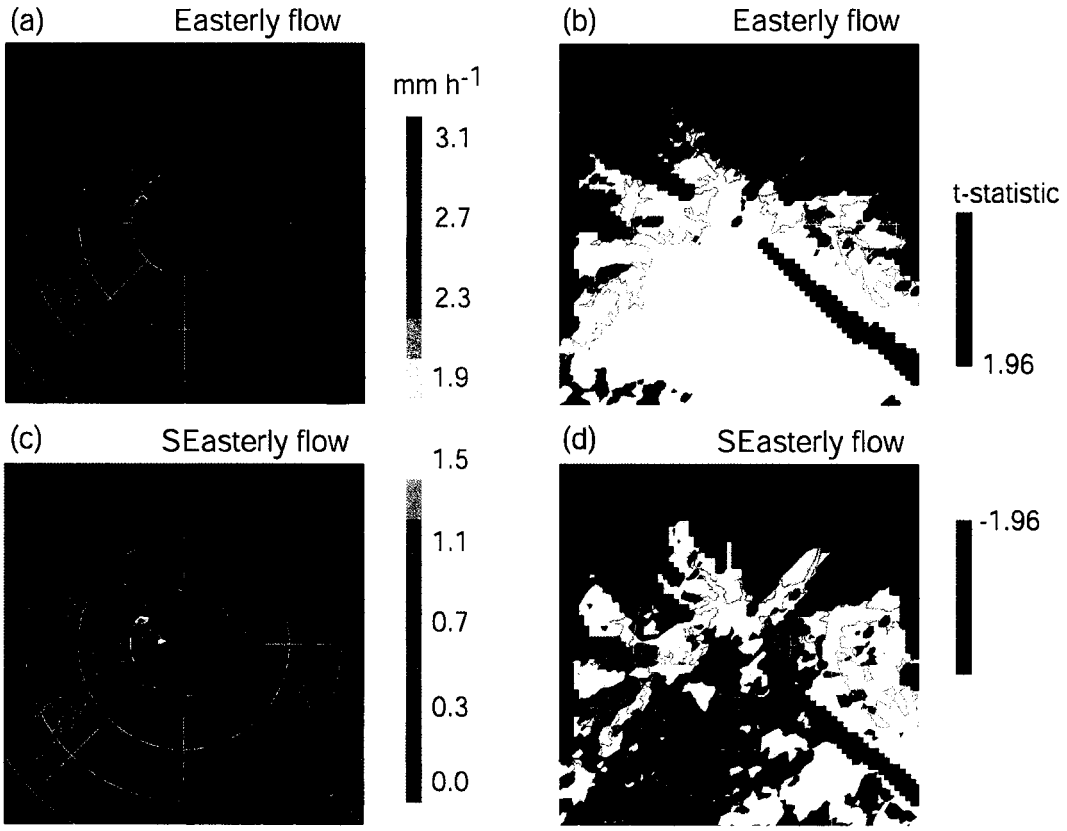

Figure 3.5. Constant altitude plots of mean rainfall rates and *t*-statistics of rain rate (first and second column, respectively) at 2-km MSL for all precipitation events in which the layer-averaged 925-700 hPa wind in the Milano-Linate sounding indicated flow from (a) and (b) 67.5-112.5° (91 radar volumes included in calculation); (c) and (d) 112.5-157.5° (183 radar volumes included in calculation); (e) and (f) 157.5-202.5° (248 radar volumes included in calculation); and (g) and (h) 202.5-247.5° azimuth (284 radar volumes included in calculation) during the 1998 and 1999 MAP season, along with the 800-m MSL terrain contour. Range ring spacing is 20 km. Red (blue) contours indicate regions where the *t*-statistic is greater than or equal to 1.96 (less than or equal to -1.96) and the null hypothesis can be rejected with a 95% confidence level (autumn 1998 and 1999; after House et al. 2001).

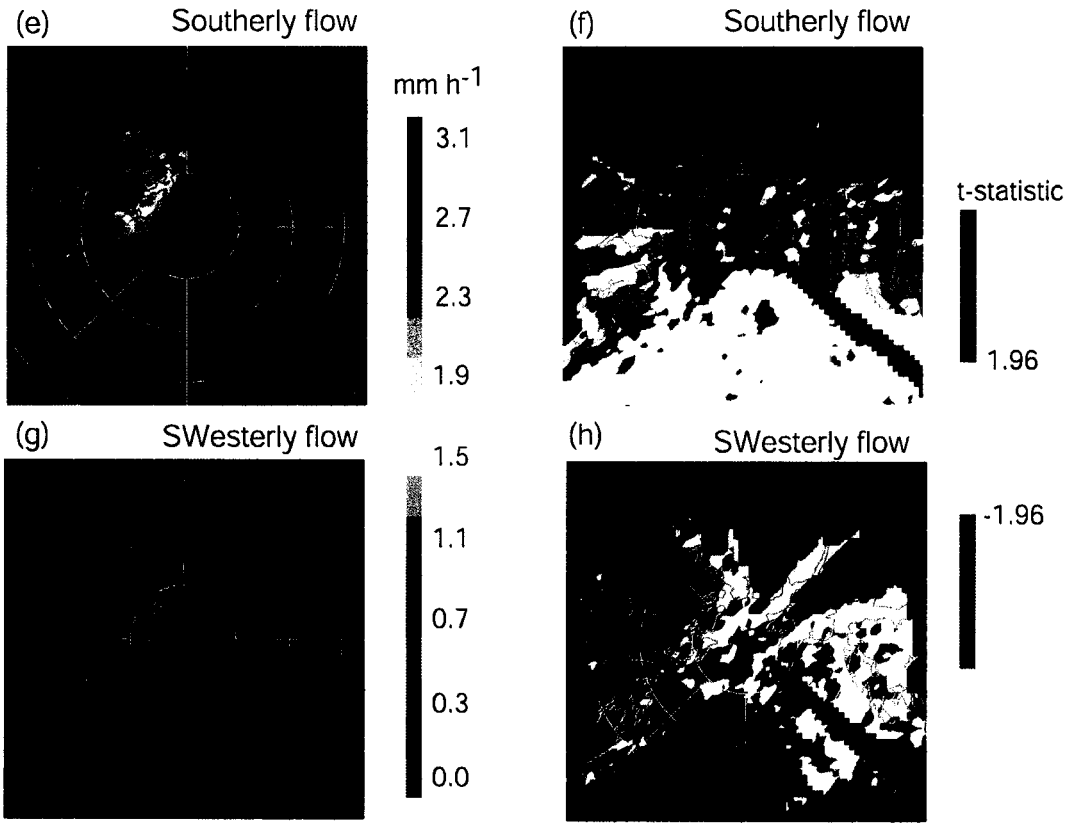

Figure 3.5. (continued)

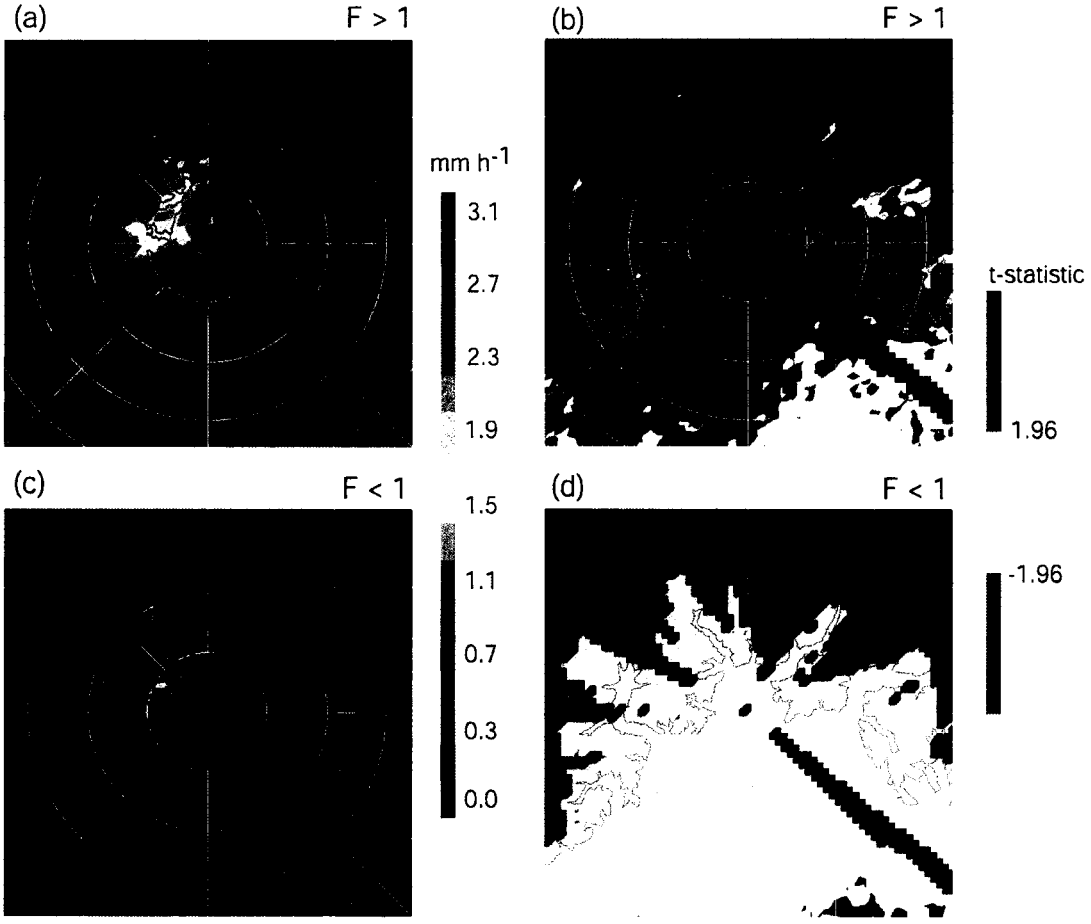

Figure 3.6. Mean 2-km fields observed by the Monte Lema radar when the layer-averaged 925-700 hPa flow direction was between 112.5-202.5° azimuth, and the Froude number was > 1, (a) Rainfall rate and (b) *t*-statistic (291 radar volumes included in calculation); and Froude number < 1, (c) Rainfall rate and (d) *t*-statistic (140 radar volumes included in calculation) during the 1998 and 1999 MAP seasons, along with the 800-m MSL terrain contour. Range ring spacing is 20 km. Red (blue) contours indicate regions where the *t*-statistic is greater than or equal to 1.96 (less than or equal to -1.96) and the null hypothesis can be rejected with a 95% confidence level (autumn 1998 and 1999; after Houze et al. 2001).

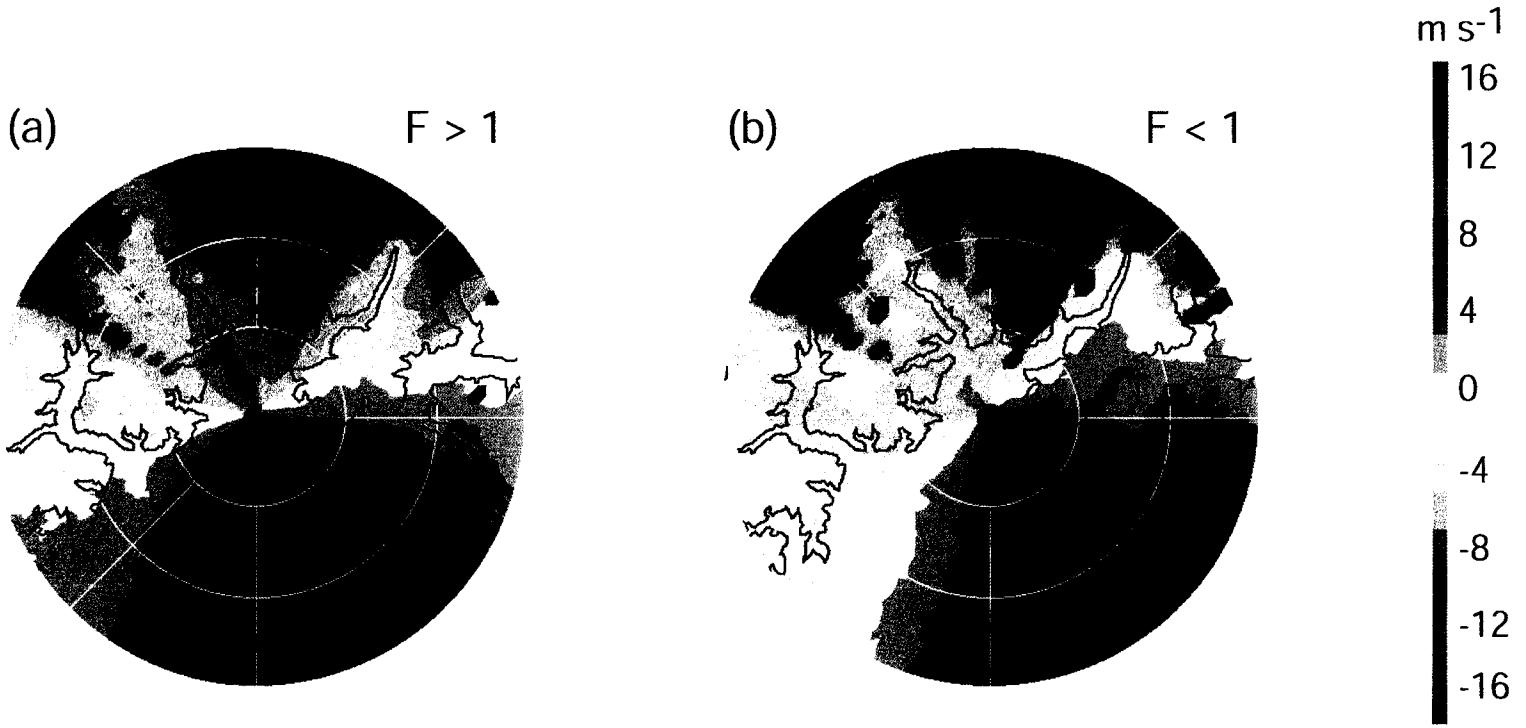

Figure 3.7. Mean 2-km radial velocity observed by the Monte Lema radar when the layer-averaged 925-700 hPa flow direction was between 112.5 – 202.5° azimuth, and the Froude number was (a) > 1 (291 radar volumes included in calculation) and (b) < 1 (140 radar volumes included in calculation) during the 1998 and 1999 MAP seasons, along with the 800-m MSL terrain contour. Range ring spacing is 20 km. Negative (positive) radial velocities denote outbound (inbound) flow (after Houze et al. 2001).

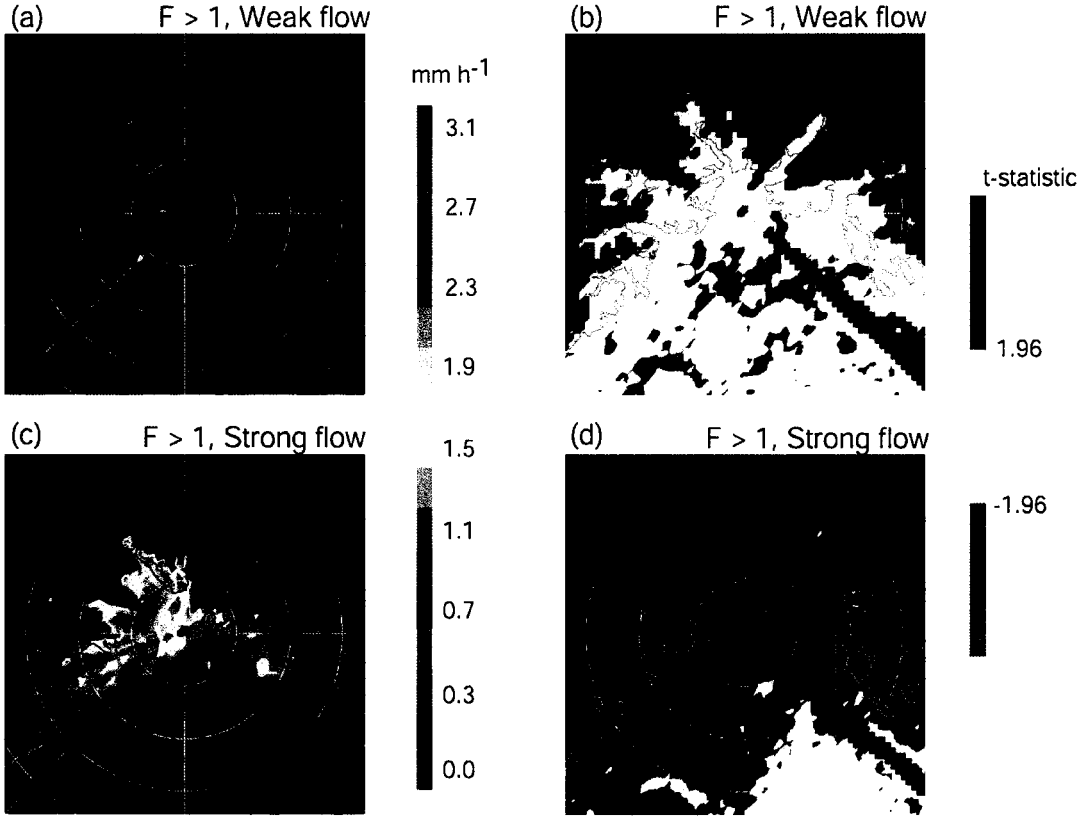

Figure 3.8. Mean 2-km rainfall rate and *t*-statistic (first and second columns) observed by the Monte Lema radar when the layer-averaged 925-700 hPa flow direction was between 112.5- 202.5° azimuth, and the Froude number was > 1 for (a) and (b) flow below 8 m s^{-1} (121 radar volumes included in calculation) and (c) and (d) flow above 8 m s^{-1} (68 radar volumes included in calculation) and Froude number < 1 for (e) and (f) flow below 8 m s^{-1} (170 radar volumes included in calculation) and (g) and (h) flow above 8 m s^{-1} (72 radar volumes included in calculation) during the 1998 and 1999 MAP seasons, along with the 800-m MSL terrain contour. Range ring spacing is 20 km. Red (blue) contours indicate regions where the *t*-statistic is greater than or equal to 1.96 (less than or equal to -1.96) and the null hypothesis can be rejected with a 95% confidence level (after Houze et al. 2001).

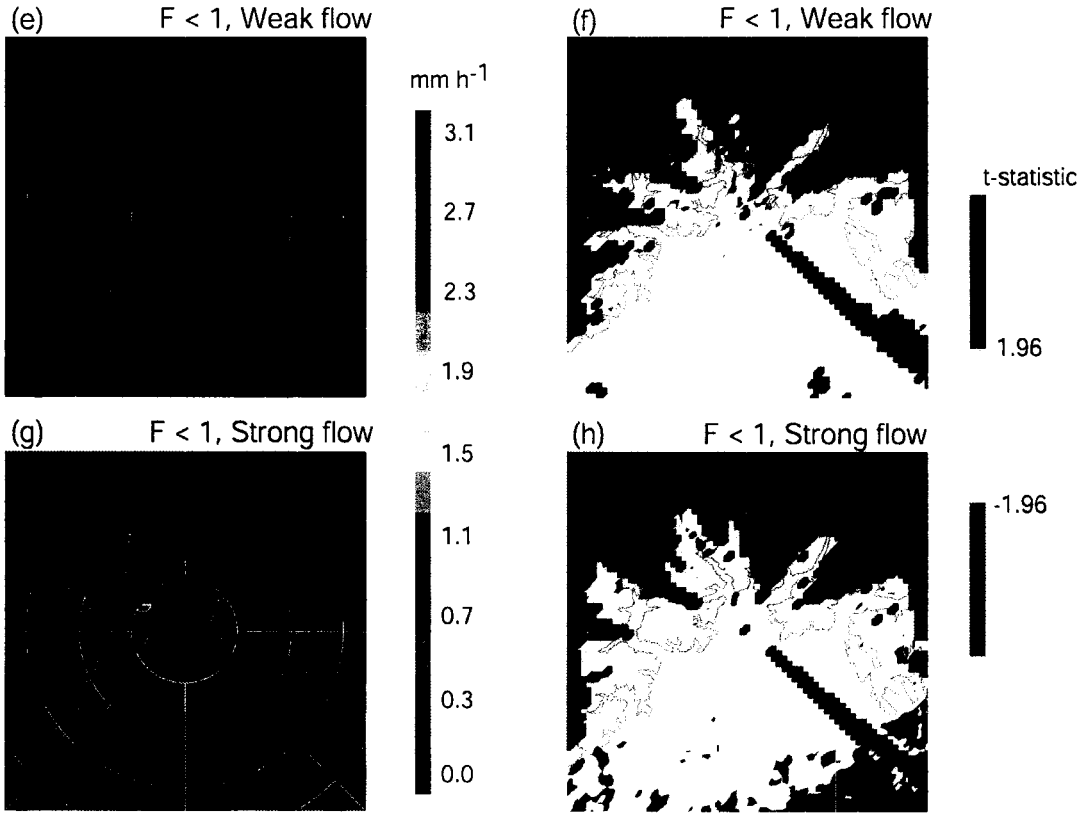

Figure 3.8. (continued)

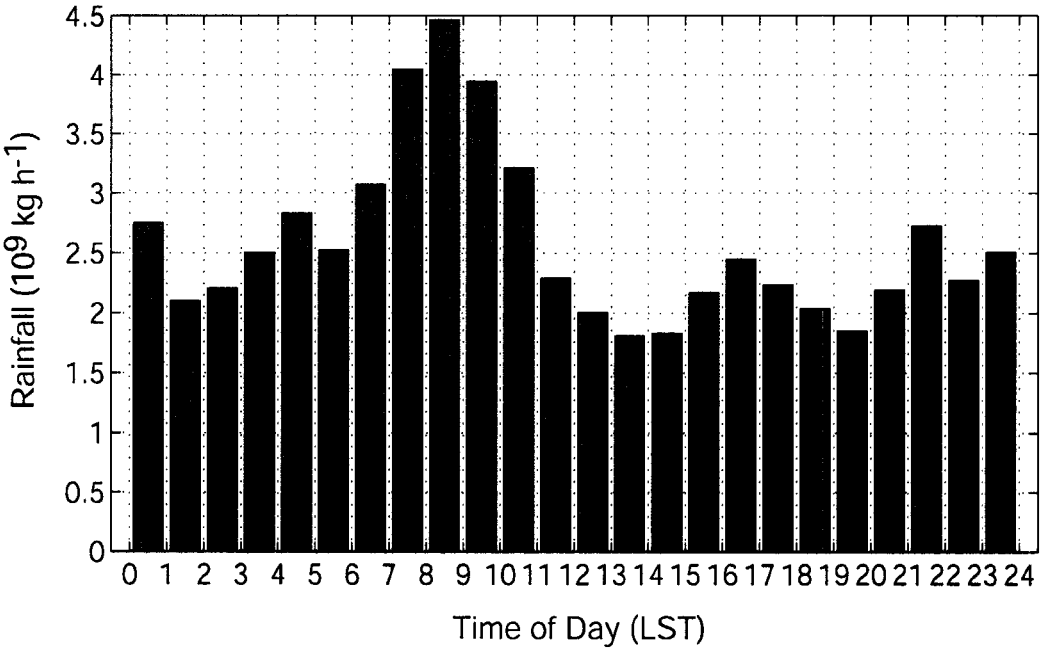

Figure 3.9. Total Monte Lema radar-derived rainfall estimate by the hour over the Northwest Target Area (rectangle in Figs. 3.1 and 3.2) at an altitude of 2-km MSL during the autumn 1998 season.

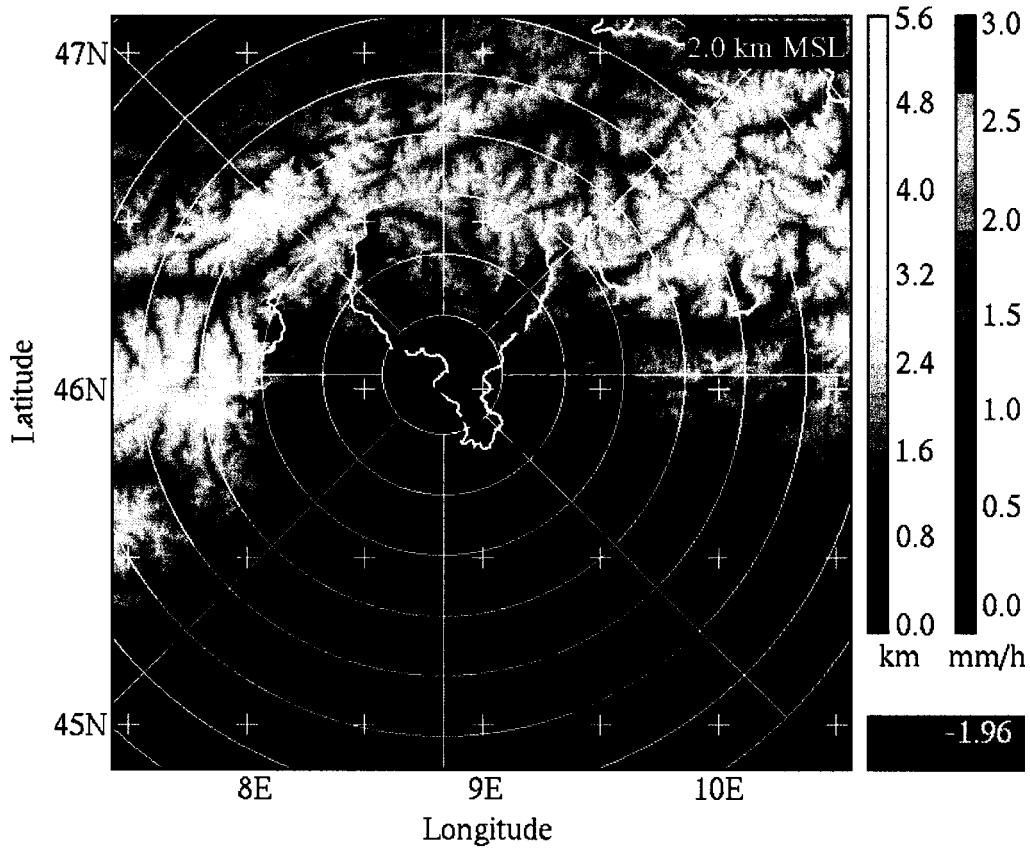

Figure 3.10. Constant altitude plots of mean rainfall rate between the hours of 0700 and 1000 LST (0600 – 0900 UTC) observed by the Monte Lema radar during the 1998 autumn season (67 volumes total). Range ring spacing is 20 km, the white contour outlines the Swiss-Italian border. The red contours outline regions where the *t*-statistic was greater than 1.96, allowing the null hypothesis to be rejected (95% confidence). The dashed elliptical contour outlines the area of maximum rainfall.

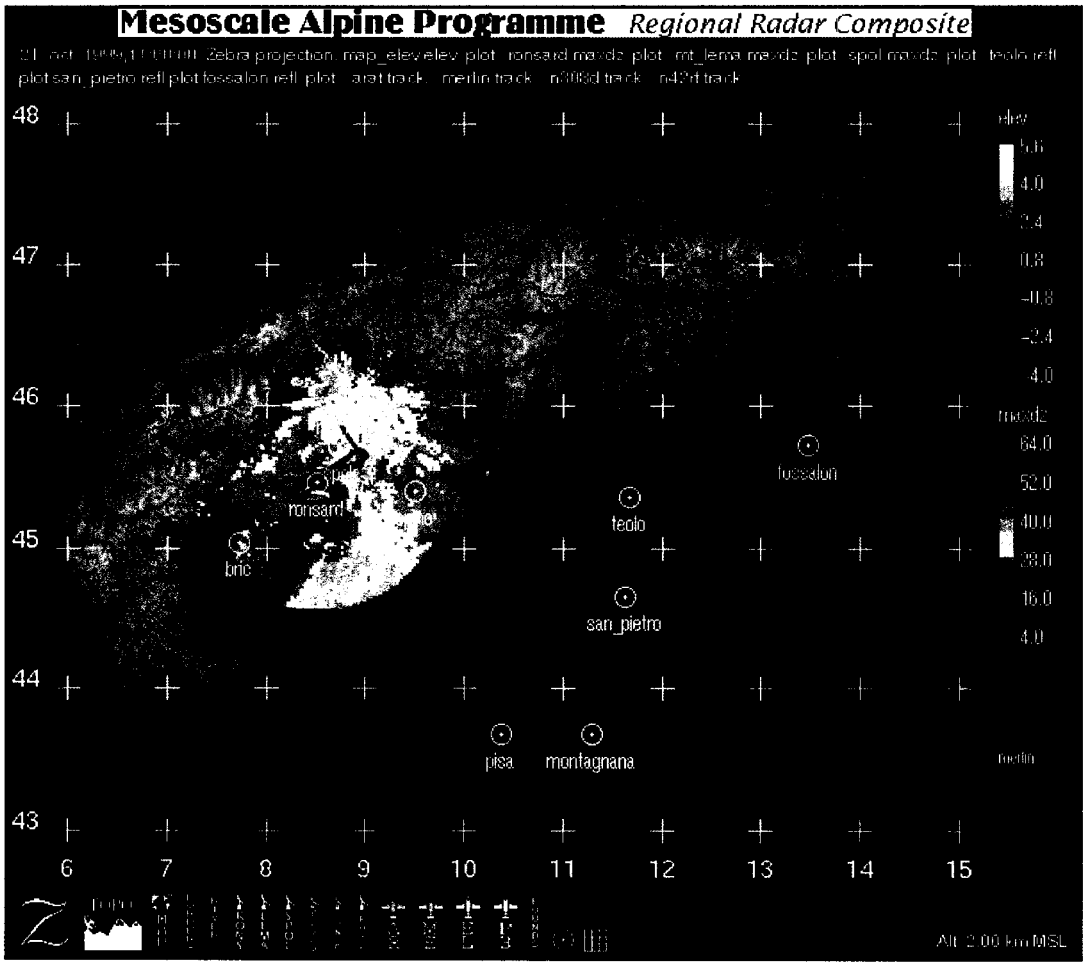

Figure 3.11. Sample regional radar composite automatically generated using MountainZebra at 1200 UTC 21 October 1999 during MAP IOP8. Reflectivity data (color shading) from the real-time Monte Lema, RONSARD, and S-Pol radar data streams are displayed, along with NCAR Electra (thick red) and NOAA P3 (blue) flight-track positions. Underlying terrain is shaded, with rivers (light blue) and political borders (thin red) superposed. Axes are in degrees (latitude/longitude).

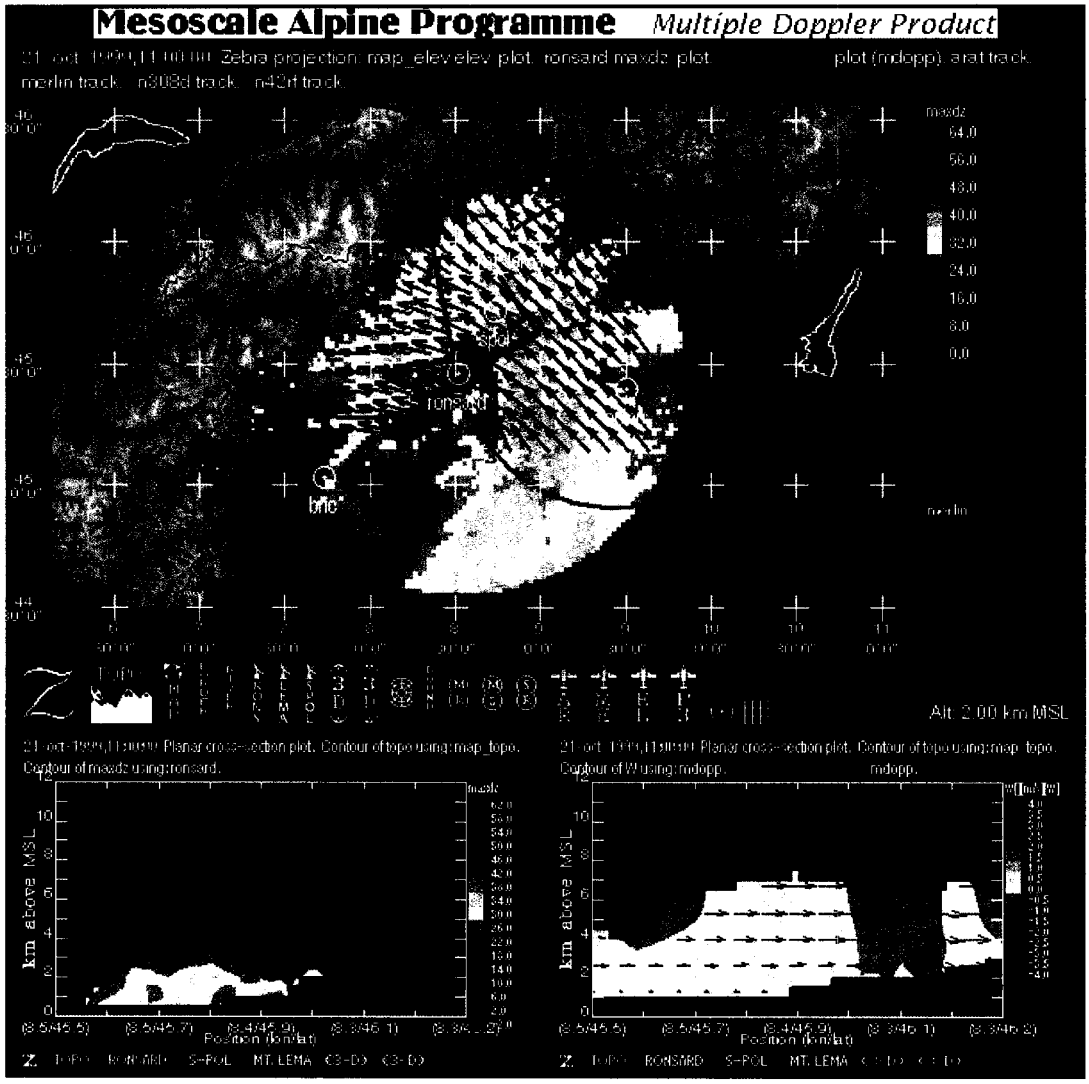

Figure 3.12. Sample MAP multiple Doppler synthesis generated in near real time using data acquired just before 1100 UTC 21 October 1999. The top panel is analogous to Fig. 3.11, except that wind vectors (red), dual Doppler lobes (black), and the position of the vertical cross sections (black line) are shown. Vertical cross sections along the black line are shown in the bottom panels, with RONSARD reflectivity (left panel), vertical velocity and horizontal wind vectors (right panel). The underlying terrain in the bottom panels is shown in green.

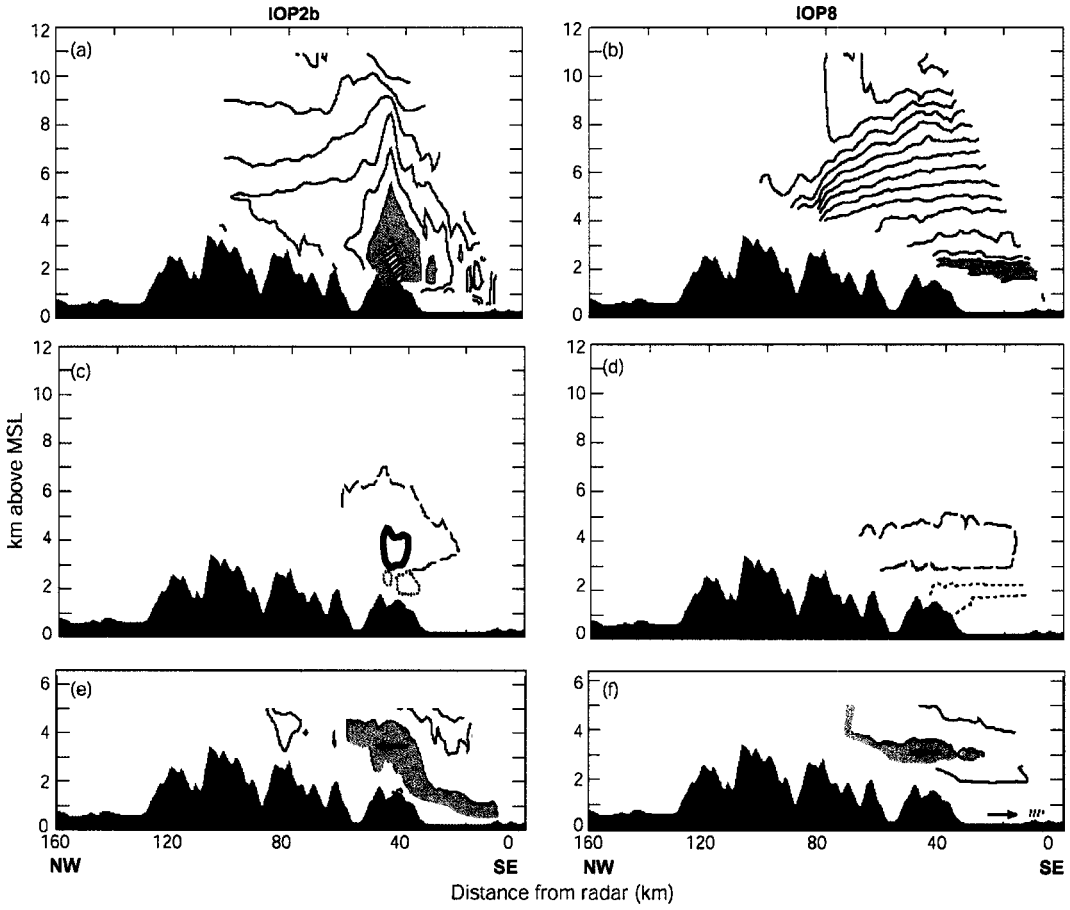

Figure 3.13. Southeast-northwest vertical cross section of S-Pol radar data. The section extends 160 km from the S-Pol radar, which was located at the southeast end of the cross section. The fields in the cross section panels have been either accumulated or averaged over 1500-1900 UTC 20 Sept 1999 for 1OP2b and 0810-0850 UTC 21 Oct 1999 for IOP8.(a)-(b)Mean reflectivity.IOP2b:contours every 10 dBZ, dBZ = 32-42 shaded, dBZ > 42 hatched. IOP8: contours every 4 dBZ, dBZ = 30.5-34.5 shaded, dBZ > 34.5 hatched. (c)-(d)Participle types identified by polarimetric radar algorithms. Contours enclose regions of frequency of occurrence of dry snow (long dashed: IOP2b, 0.15; IOP8, 0.85), wet snow (short dashed: IOP2b, 0.08; IOP8, 0.40), and graupel (solid: IOP2b, 0.13). (e)-(f)Mean radial velocity. IOP2b: > 12 m s^{-1} shaded; IOP8: > 19.5 12 m s^{-1} shaded. Negative contour shown: –0.5, –3 m s^{-1}. Solid contours indicate flow towards the radar; dashed lines indicate flow away from it. Arrows indicate direction of horizontal component of radial velocity (reproduced from Houze et al. 2001a).

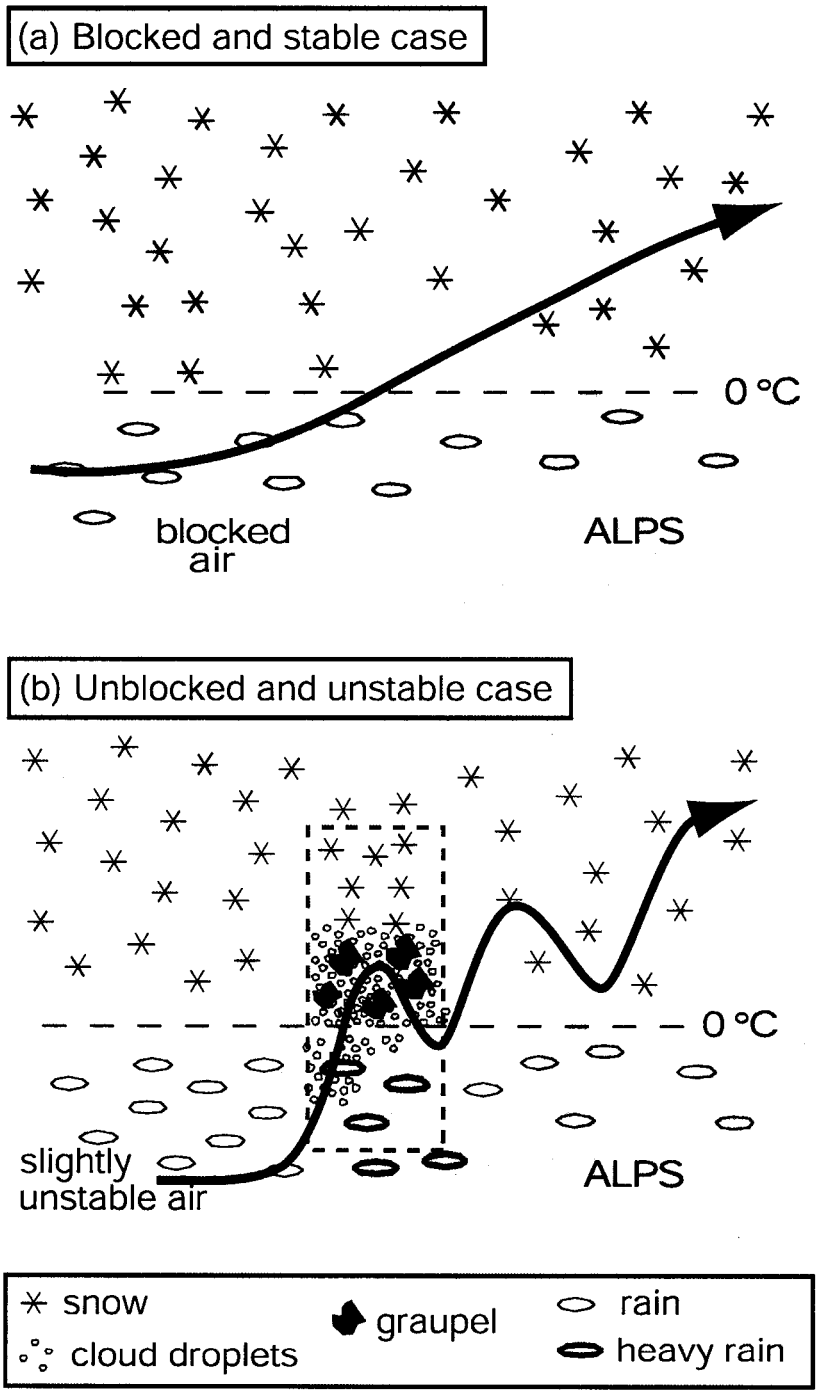

Fig. 3.14. Conceptual model of Alpine precipitation amid (a) blocked and stable flow and (b) unblocked and unstable flow. The streamlines indicate the behavior of the flow, while symbols denote hydrometeor type. The dashed box outlines the location of embedded convection (after Medina and Houze 2003).

CHAPTER 4

THE COASTAL TERRAIN OF NORTHERN CALIFORNIA[9]

4.1 Background

Coastal Northern California is an ideal laboratory for observing stable orographic precipitation. Deep convection is rare along the West Coast, and heavy precipitation is usually associated with land-falling baroclinic systems that direct strong, moist low-level flow against the terrain from the Pacific Ocean (e.g., Nagle and Serebreny 1962; Elliot and Hovind 1964; Hobbs et al. 1975, 1980; Houze et al. 1976; Braun et al. 1997;Doyle 1997; Colle et al. 1999, 2002; Yu and Smull 2000; Neiman et al. 2004; Ralph et al. 2004). The terrain in the region contains quasi two-dimensional mountain ridges that are analogous to traditional idealized model studies of flow over terrain (e.g., Queney 1948). The ridges are oriented from north-northwest to south-southeast and are approximately orthogonal to the prevailing low-level flow during heavy precipitation events (Fig. 4.1). The ridges known as South Fork Mountain and the King Range will be prominent in the subsequent discussions of this chapter.

When strong, moist, low-level wind interacts with the California coastal orography, heavy rainfall accumulation (up to 250 mm in a day) can occur. The rain may combine with rapid snowmelt and produce extreme flooding of local rivers and streams. During one flood in December 1964, the Eel River (Fig. 4.1) rose approx-

imately 25 m above flood stage and experienced a peak discharge rate of 21,300 m^3 s^{-1} (source: U.S. Geological Survey). These extreme events can occur when the low-level jet (LLJ) required by hydrostatic balance and geostrophic adjustment ahead of a front conveys moisture and heat into the region of the mountains for prolonged periods of time, sometimes for several days. Floods occur in the European Alps for much the same reason, as the low-level moist jet ahead of a front impinges on the barrier (Buzzi et al. 1998; Doswell et al. 1998; Rotunno and Ferretti 2001).

Browning (1986) characterized the poleward heat transport by a LLJ ahead of a front as a "warm conveyor belt." Ralph et al. (2004) have referred to the strong core of poleward moisture flux within prefrontal LLJs approaching the California coastline as "atmospheric rivers." This manifestation of the LLJ emanates from the northern fringes of the tropics, and is hence quite moist. When fronts approach the northern California coast, the LLJ is nearly always southwesterly, oriented quasi-perpendicular to the 2D ridges of the coastal mountains of Northern California and thus in an optimal orientation for orographic enhancement of the precipitation associated with the passing baroclinic system.

Small-scale processes evidently play various roles in the orographic precipitation enhancement process. Smith (1979) pointed out the likely importance of convective-scale cellularity. Elliot and Hovind (1964) suggested that precipitation associated with fronts passing over California indeed manifested embedded small

---

[9] This chapter to be submitted to Monthly Weather Review (James and Houze 2004)

convection, which they thought enhanced the total rainout. Also examining California precipitation, White et al. (2003) pointed out the probable importance of coalescence in the cloud layer below the 0°C level as an important microphysical mechanism producing precipitation fallout in the air passing over the coastal mountains of California. They also suggested that small convective cells may play a role. Larger, deep convective cells obviously also play a role when they occur in flow over terrain (e.g. Caracena et al. 1979); however, the northern California region is not a favored location for deep convection. In studying the radar echo climatology in regions of precipitation enhancement over the Alps, Houze, James and Medina (2001, hereafter HJM; Chapter 3) found that the basic pattern of precipitation enhancement depended on whether the upstream flow was blocked or unblocked. When blocked the enhancement began upstream of the barrier (as suggested, for example, by Grossman and Durran 1984). In the unblocked cases, the enhancement occurred over the lower slopes of the barrier. Major Alpine floods occur primarily with the unblocked cases in which all the low level air tends to suddenly rise over the barrier with concomitant rapid growth and fallout of precipitation (Buzzi et al. 1998; Doswell et al. 1998).

Using data from the Mesoscale Alpine Programme (MAP), Medina and Houze (2003) examined cases in which orographic enhancement was occurring in both blocked and unblocked flows ahead of baroclinic troughs passing over the Alps. They found distinctly different Doppler and polarimetric radar signatures in

the two types of flow. In the unblocked flow the warm moist air rose abruptly, some small-scale convective cells occurred at peaks in the terrain, and riming and coalescence growth occurred vigorously at low altitudes (Yuter and Houze 2003). The blocked flows were generally stable and marked by a layer of nearly zero cross-barrier flow at low levels. Strong shear marked the transition to a layer of strong cross barrier flow above the blocked layer (Medina and Houze 2003; Houze and Medina 2004; Medina et al. 2004).

This chapter explores the pattern of orographic precipitation enhancement over the coastal mountains of northern California and how the pattern relates to the strength and stability of the upstream flow. Achieving this objective will help determine whether processes occurring over this mountainous region are similar to or different from processes over the Alps and other major mountain ranges. In this effort, WSR-88D radar data was collected over a 2.5-year period at Eureka, California (Fig. 4.1). The radar covers the precipitation both over the ocean and as it crosses the windward slopes of the mountain barrier. The radar echo climatology was analyzed in relation to the topography, wind, and thermodynamic stratification. This analysis elucidates the orographic precipitation processes by analyzing not only the mean horizontal precipitation patterns but also the mean vertical structure of the radar echo in relation to the coastline and mountainous terrain.

Section 4.2 describes the data and methods used in this chapter. Section 4.3 presents the large-scale setting of major rain events over the northern California

coastal region. Section 4.4 presents the overall average three-dimensional radar echo climatology. Section 4.5 discusses the variability of the radar echo climatology with respect to mid-level flow. Section 4.6 analyzes the orographic precipitation processes with respect to the wind velocity and stability of the low-level flow impinging on the mountains. Section 4.7 integrates all the results.

4.2. Data and methods

The basic data set for this chapter is a 2.5-year archive of major precipitation events from the Eureka, California, WSR-88D. This coastal radar, located near Cape Mendocino, has a relatively unimpeded view of precipitation over the mountains to its east and over the ocean to the west. This location (Fig. 4.1) allows sampling of precipitation systems as they approach the coast, make landfall, and move over the mountains. Terrain clutter and shadowing are less of a problem for the Eureka WSR-88D than other West Coast WSR-88D sites (Westrick *et al.* 1999). Archived Level II data of reflectivity and radial velocity (Crum and Alberty 1993) were obtained for most of the heavy precipitation days during 1 October 1995 - 31 March 1998, a period including the CALJET experiment (Ralph et al. 1999).

A major precipitation event was defined as a day on which at least 25% of the 73 automated rain gauges in the region bounded by 39 °N, 42 °N, 122 °W, and the California coastline recorded 25 mm (1 in) or more of precipitation. The white circles in Fig. 4.1 show the locations of the gauges. Radar archives were available

for 61 of the 67 heavy precipitation days identified (see Table 4.1). The basic unit of radar data was the three-dimensional volume scanned by the WSR-88D elevation angle sequence. To reduce autocorrelation and minimize data storage requirements, the time resolution of the radar data was reduced by using only the data volumes obtained at one-hour time intervals.

Since the radar processor's clutter suppression algorithm was insufficient to remove all terrain contamination, a digital terrain mask was developed. The terrain mask used an equivalent-earth-radius ray-propagation model to approximate the altitude of the radar's lowest tilt (0.5°) at each radar gate (Doviak and Zrnić 1993, p. 14 – 23). The equivalent earth radius corresponding to the strongest vertical refractivity gradient of all 61 heavy precipitation days was used to give a liberal estimate of the amount of beam refraction. Then, a terrain elevation dataset with 30-sec spatial resolution was used to determine whether any terrain intersected the bottom of the radar beam in a horizontal latitude/longitude element of dimensions 1' × 1'. If the main lobe of the radar (width 0.94°) was intersected by terrain, then that range bin and all bins at farther range in that radial were removed. To reduce side-lobe contamination, if terrain was located within 0.5° of the bottom of the main lobe, then the corresponding radar bin was deleted. This technique removed virtually all terrain clutter and shadowing from the dataset, and allowed all radar reflectivity over terrain to be interpreted as precipitation rather than clutter contamination.

To remove noise, radial velocity data were deleted if their corresponding reflectivity values were deleted or below a threshold of -10.0 dBZ. The radial velocity data were then dealiased using a University of Washington algorithm similar in construction to the WSR-88D algorithm (Eilts and Smith 1990). A small fraction of the volumes that were not successfully dealiased by the algorithm were rejected, leaving a total of 1,176 for analysis. The volumes were bilinearly interpolated to a three-dimensional Cartesian grid with 2-km horizontal spacing and 0.5-km vertical spacing using NCAR's *SPRINT* software (Mohr and Vaughan 1979) and finally converted to Unidata's Network Common Data Format (NetCDF) for analysis using *MountainZebra* (James et al. 2000), which is a version of NCAR's *Zebra* software (Corbet *et al.* 1994) in which the detailed terrain field is included. The interpolation grid, superposed with a vertical cross section of the most commonly used WSR-88D Volume Coverage Pattern (VCP 21), is shown in Fig. 4.2.

Using the interpolated radar volumes, reflectivity and radial velocity means and composites were computed (see Appendix). To reduce unwanted noise and radar artifacts, inverse range-squared horizontal smoothing was then applied at each interpolation grid point within a 16-km horizontal radius of influence for all horizontal maps (6-km horizontal radius for all vertical cross sections). The superposed epoch analyses led to conclusions about the sensitivity of the precipitation in the vicinity of Eureka to dynamic and thermodynamic variables of the offshore flow. These upstream variables were estimated using analyses and 6-h forecasts from a

90-km Eta model grid. The model data at the four upstream model grid points bounded by the ellipse in Fig. 4.1 were horizontally averaged to produce smooth vertical soundings at 6-h intervals. If no model grid was available within 3 h of a radar-volume time, the volume was not used for those calculations that required sounding information. Model grids were available for 1116 of the radar volumes.

The 900 – 800 mb layer (1 – 2 km MSL) in the synthetic soundings, corresponding to the LLJ altitude and the strongest correlation with precipitation (Neiman et al. 2002), was used to estimate the static stability, wind speed, wind direction, and dew point temperature upwind. The static stability was represented by the moist Brunt-Väisälä frequency (Durran and Klemp 1982), and computed using finite differences. The 700 – 500 mb layer in the synthetic soundings was used to represent "mid-level" characteristics of the flow.

4.3 Large-scale flow and stability

Figure 4.3a and 4.3b shows the mean large-scale synoptic conditions indicated by NCEP (National Centers for Environmental Prediction) reanalysis grids for the major rain events. This map shows that on average the 1000 and 500 mb flows are generally southwesterly, perpendicular to the mountain ranges of coastal northern California, consistent with Ralph et al. (2004) and other studies mentioned above.

Fig. 4.4a shows the mean upstream sounding produced for the 61 heavy precipitation days. The average 0°C level is around 780 mb (over 2 km MSL) and the -15°C level is at about 560 mb (~4 km MSL). The dew-point depression in the profile gradually increases from about 2°C at the surface to 8°C above 4 km MSL, indicating that mid-level cloud is more scarce than at low levels. In addition, the temperature profile reveals the prevalence of weak conditional instability below the 850-mb level, combined with abundant near-surface moisture. It may be assumed that such conditions promote shallow convective enhancement over the terrain (e.g. Medina and Houze 2003). Within the layer of conditional instability below 850 mb, the wind profile veered with height, indicative of warm advection, with an average 900 – 800 mb wind speed of 30 – 35 kt (15 – 18 m s^{-1}) from the west-southwest.

As will be shown in the remainder of this chapter, the precipitation regimes observed by radar are distinctly different under thermodynamically stable vs. neutral and unstable conditions. Figure 4.4 also shows the average upstream soundings during (b) unstable or neutral and (c) stable events, respectively, when the 900 – 800 mb wind direction was west-southwesterly and the 0°C level was at least 2.5 km MSL (see Section 4.6). The soundings showed only slight deviations from the mean sounding. The unstable/neutral events exhibited slight conditional instability in the 900 – 800 mb layer and somewhat drier mid-level air.

Figure 4.3 also depicts the composite synoptic patterns observed during unstable (Figs. 4.3c,d) and stable events (Figs. 4.3e,f). The mean sea-level pressure

panels (Figs. 4.3c and 4.3d) are qualitatively very similar, except that the stable events exhibited slightly weaker southwesterly gradient wind. The mid-level height pattern (Figs. 4.3d and 4.3f) was also very similar, with comparable 700-mb upward motion between unstable and unstable events. The 700-mb vertical motion patterns are both elongated in Figs. 4.3d and 4.3f, with apparent frontal orientation from south-southwest to north-northeast. In both cases, the California coast appeared to be located in prefrontal flow. Figures 4.3 and 4.4 thus show that the synoptic conditions for the heavy rain events were similar. Both stable and unstable events corresponded to prevailing southwesterly, prefrontal flow, with only slightly weaker low-level wind during stable events. However, as will be shown below, the orographic precipitation enhancement varied dramatically depending on slight variations in the stability of the flow impinging on the coastal mountains.

4.4 Radar climatology

The horizontal maps of mean echo patterns in this discussion are mostly taken at the 2-km level, which is high enough to avoid much of the near-field blocking of the radar beam by the terrain while being in the rain layer below the 0°C level (Fig. 4.2). Vertical cross sections shown here incorporate all available grid levels.

Figure 4.5a shows the 2.0-km altitude horizontal display of reflectivity over Coastal Northern California, averaged over the 61 heavy precipitation days. Partial

beam shadowing occurred behind South Fork Mountain (Fig. 4.1) and other terrain features, and corresponding radar gates beyond those obstacles to the beam were removed from the dataset. Removal of these blocked and partially blocked beams results in the circle of radar observations being much smaller to the east of the radar than to the west in Fig. 4.5 and similar figures throughout the chapter.

The overall pattern of reflectivity in Fig. 4.5a indicates upstream enhancement. The echo contours offshore are oriented roughly parallel to the coast, with echo intensity generally increasing towards shore. The strongest offshore gradient of reflectivity is roughly 60 km from the coast, which is roughly 150 km from the crest of the Coastal Range. Estimates of the average Rossby radius using the dry Brunt-Väisälä frequency roughly correspond to this offshore distance, suggesting that convergent lifting due to geostrophic adjustment in sub-cloud air may be enhancing precipitation upstream. The Rossby radius estimated using the moist Brunt-Väisälä frequency (Durran and Klemp 1982) is only about 30 km, and within this distance from the barrier the reflectivity was even higher, suggesting additional adjustment within the cloud layer itself, closer to shore. However, Doppler velocity data do not provide conclusive evidence of the suspected upstream flow adjustment, and the complexity of the terrain and variability in the static stability make scale analyses of the Rossby radius non-trivial.

A quasi-circular maximum of reflectivity is apparent offshore at radar range of about 40 km in Fig. 4.5a. This curved maximum is caused by bright-band pat-

terns, associated with melting of ice particles. However, the ringed pattern mimics the shape of the coastline (e.g., Braun et al. 1997), which bulges westward at Cape Mendocino, and the curved reflectivity pattern could also indicate upstream enhancement. Over the terrain, especially on the windward side of the gradually upward sloping Coastal Range and over the smaller-scale peaks (i.e. King Range and South Fork Mountain; Fig. 4.1), strong enhancement is observed.

Fig. 4.5b depicts the percentage of radar volumes in which the reflectivity equaled or exceeded 13 dBZ, which is roughly equivalent to a rainfall rate of 0.2 mm/h. Overall, the patterns in Fig. 4.5a and 4.5b are qualitatively similar, suggesting that orographic forcing primarily makes precipitation more *frequent* rather than more *intense*. Calculations of mean conditional rainfall rate (not shown), which is related to mean echo intensity, confirm this result, with the exception that slightly higher echo intensity occurred both over the higher terrain and offshore within roughly 60 km of the coast.

The prevailing Doppler velocity at 2.0 km MSL over all 1176 radar volumes (Fig. 4.5c) was nearly perpendicular to the Coastal Range from the southwest at speeds approaching 20 m s^{-1} at 2.0 km MSL. Maps of the Doppler velocities at other altitudes indicated the wind was veering with height, especially below 3-km MSL altitude, consistent with frictional turning and/or warm advection. The strong horizontal component of the upslope flow in this chapter (~20 m s^{-1}) is at least twice

the strength of that component observed during MAP rainfall events (~8 m s^{-1}; Ch. 3).

The strong flow toward the barrier at the 1-3 km levels during heavy precipitation events had Froude numbers greater than unity for both saturated and unsaturated air, indicating that flow blocking was not occurring at the 900 – 700 mb levels. Nonetheless, upstream precipitation enhancement was evident in the reflectivity data. This enhancement was particularly strong along the red line in Fig. 4.5a. The high reflectivity values began well offshore. The vertical cross section of average reflectivity in Fig. 4.5d, taken parallel to the prevailing southwesterly wind along the red line in Fig. 4.5a, shows the vertical structure of the enhanced reflectivities. The portion of the cross section located within 45 km of the shore included echo within the layer 1-3 km MSL. However, the echo was truncated below this layer as a result of beam geometry. The strongest average reflectivity occurred over the first major peak of terrain (i.e. the King Range; located at about 70 km on the horizontal scale in Fig. 4.5d). This maximum extends to the upper levels as an upward bending of the reflectivity contours over the first peak. This behavior was evident in HJM's radar echo climatology (Chapter 3) over the Mediterranean side of Alps and by Medina and Houze (2003) in MAP. The latter authors used Doppler and polarimetric radar data to conclude that the occurrence of the maximum over the first peak of the mountain range was a characteristic of unblocked flow, i.e. strong upstream flow, approximately neutral to slightly unstable, impinging on the

barrier. Thus the strong echo maximum over the first peak of terrain is consistent with the mean sounding upstream of Eureka indicating a generally unblocked southwesterly flow impinging on the mountains of northern California.

In contrast to the sounding and radar data just discussed, the upstream enhancement far ahead of the first peak of terrain is suggestive of blocking. The climatological radar echo pattern in the Eureka radar is thus a combination of unblocked and blocked characteristics. In Sec. 4.6, it will be shown that while the flow is unblocked as a result of the strong low-level cross-barrier flow component, which would dominate the Froude number, the thermodynamic stability of the flow is often quite strong, and upstream enhancement increases with increasing stability of the cross-barrier flow. This behavior suggests that perhaps the cross-barrier flow, which is largely unblocked in the Froude number sense, nevertheless feels some effects of the barrier upstream via stability, and these effects enhance the precipitation offshore and upstream of the coastal topography.

Since the radar data for the major rain events considered here do not extend below the 1-km level (nor below 3 km far from the radar), it is impossible to know the reflectivity or radial velocity conditions in the boundary layer or near the sea surface. It is possible that some of the echo enhancement seen in the echo climatology over the ocean upstream from the coastal mountains could have been influenced by a very thin layer of near-surface air, in contact with the cold ocean, blocked and dammed against the coastal terrain. Further evidence is needed to con-

firm this suspicion. Neiman et al. (2002, 2004) have found such a thin layer off the coast of California and have suggested that its blocking modifies landfalling cyclones with LLJs of the type considered here. The air above the surface layer could have been lifted over this shallow layer of cold air enough to produce the offshore upstream enhancement. The layer lifted above the thin layer of marine air could have then proceeded over the coastal mountains in a relatively unblocked fashion. This behavior might help explain why upstream enhancement (normally associated with blocked flow) occurs offshore in an otherwise relatively unblocked flow (Medina and Houze 2003). The shallow blocked pool of cold marine air might work together with the stability of the cross-barrier flow above the shallow surface layer to explain the echo enhancement upstream of the mountains.

4.5 Relationship of radar climatology to mid-level flow

A number of superposed epoch analyses were performed on the radar data to provide insight into the sensitivity of heavy coastal precipitation to characteristics of the low-level (900 – 800 mb) and mid-level (700 – 500 mb) flow. Of these analyses, most are not presented here, as they do not provide new insight into the behavior of precipitation. Of particular note, the moist and dry Froude number F of the flow (where $F=U/(Nh)$, U is the speed of the wind normal to an idealized two-dimensional barrier, h is the height of the barrier, and N is the Brunt-Väisälä frequency) was usually greater than unity within the 900 – 800 mb layer and had low

correlation with radar reflectivity. Thus, classic idealized two-dimensional flow blocking did not appear to play as clear a role in patterning the precipitation as in the Alpine region examined in MAP (HJM; Medina and Houze 2003). Compared to the Alps, the flow toward the California coastal mountains is stronger and the mountain barrier is lower. It will be shown here that the strength and stability of the cross barrier flow both appear to be important for the California coastal mountains, but seem to affect the flow response (and hence the precipitation) separately rather than in the proportional sense expressed by the Froude number. Table 4.2 lists the upstream flow characteristics that showed significances. These are subdivided into low-level and mid-level flow features. The radar volumes were divided into subsets or "epochs" based on each of the variables as shown in Table 4.2. The mid-level features will be discussed in this section (Analyses I and II), and the low-level features in Section 4.6.

4.5.1 Analysis I: Mid-level wind speed

Analyses I, II, IV, and V investigate the sensitivity of the three-dimensional reflectivity pattern when the low-level (900 – 800 mb) wind direction was between southwesterly and westerly (225 - 270°), and the 0°C level was at least 2.5 km MSL altitude. Thus constraining the 0°C level allowed bright band contamination of the echo patterns to be minimized in 2.0-km MSL horizontal displays. Limiting the wind direction to 225 – 270° allowed signals associated with key variables other

than wind direction to be investigated for the prefrontal and frontal LLJ cases dominating the coastal orographic precipitation.

The strength of the mid-level flow is an indication of the strength of the synoptic forcing. Figure 4.6 shows the mean reflectivity at 2.0 km MSL altitude as a function of the 700 – 500 mb layer-averaged wind speed. When the speed was < 30 m s^{-1} (Fig. 4.6a), synoptic forcing was weaker and the echo intensity tended to be weaker over most of the radar domain. Much less terrain enhancement and random precipitation patterns were observed. The vertical cross section of reflectivity in Fig. 4.6b lies along the red line in Fig. 4.6a, which is generally parallel to the LLJ. The greatest echo enhancement was at low levels over the windward slopes, midway up the range (Fig. 4.17b; x = 130 – 170 km). The maximum echo over the first peak of terrain was apparent but weaker than average (cf. Figure 4.5d).

Stronger mid-level flow produced a much stronger pattern of radar echo enhancement (Fig. 4.6d). The offshore echo intensity gradient associated with upstream enhancement was strong and sharply defined. The echo intensity directly over the first two primary ridges in the terrain was greatly intensified. The strong upstream enhancement began about 60 km offshore, and the bright band was evident both just ahead of and just downstream of the first peak of terrain. The bright band emphasizes again the stratiform nature of the precipitation, punctuated by the echo core over the first peak of terrain. In this well-defined pattern, the precipitation extrema over individual peaks (especially King Range at x = 115 km in Fig. 4.6d)

were displaced downwind from their positions in Fig. 4.6b by the stronger mid-level flow. Precipitation was thus more apt to spill over into inland areas in the cases of stronger mid-level.

4.5.2 Analysis II: Mid-level dew-point depression

The importance of mid-level humidity to the orographic precipitation enhancement is indicated by the Eta-model dew point depression (temperature minus dew-point) of the mid-level flow (Fig. 4.7). When the 700 – 500 mb dew-point depression (i.e. temperature minus dew-point temperature) was at least 3°C, much lower reflectivity was generally observed (Figs. 4.7a and 4.7b). When the dew-point depression was <3°C all the orographic processes are more pronounced.

4.6 Sensitivity of heavy precipitation to low-level flow characteristics

The frequency distributions of low-level wind and thermodynamic variables during heavy precipitation events are shown in Fig. 4.8. As expected, about half of the radar volumes during heavy precipitation events exhibited southwesterly-westerly flow (Fig. 4.8a), approximately orthogonal to the Coastal Range (Fig. 4.1). Most of the volumes had a LLJ speed between 15 and 25 m s^{-1} (Fig. 4.8b). Figure 4.8c shows that more than half the volumes were conditionally unstable or neutral between 900 and 800 mb, while during stable events the moist Brunt-Väisälä frequency exhibited a wide range of values. The influence of each of these variables in

relation to precipitation structure is examined below in the discussions of Analyses III-V.

4.6.1 Analysis III: Low-level wind direction

Figure 4.9 displays the mean reflectivity composites when the offshore low-level layer-averaged wind direction was (a) south-southwesterly (180 – 210°), (b) southwesterly (210 – 240°), (c) west-southwesterly (240 – 270°), and (d) west-northwesterly (270 – 300°) respectively. In this figure, it is evident that each low-level flow direction experienced at least some precipitation enhancement over South Fork Mountain and the King Range. South-southwesterly and southwesterly flow (Figs. 4.9a and 4.9b), which was most likely pre-frontal or frontal, produced greater precipitation not only over land, but well upstream. This flow apparently brought plentiful moisture into the region (Ralph et al. 2004), and typically possessed a higher static stability. Average reflectivity values exceeding 25 dBZ are evident in Figs. 4.9a and 4.9b at distances > 150 km upstream from the Coastal Range, implying either a large Rossby radius of upstream influence or simply more precipitation in general.

West-southwesterly and west-northwesterly flow (Figs. 4.9c and 4.9d), which was likely post-frontal and therefore less stable, exhibited lower-than-average mean reflectivity values over most of the domain and especially upstream. These flow directions apparently provided less moisture and decreased static stabil-

ity, and therefore favored more intermittent convective showers, especially over the highest terrain. The mean radar reflectivity pattern under these conditions (Figs. 4.9c and 4.9d) exhibited the same general upslope enhancement as the southwesterly cases. However the enhancement was more evident in the southern part of the radar area, possibly because the northern portions would have been more influenced by the colder air behind the typical southwest-to-northeast oriented fronts moving onshore. A bright-band ring pattern at 60 km range from the radar is apparent in post-frontal northwesterly flow (Figs. 4.9c and 4.9d), consistent with lower 0°C levels in the colder postfrontal air.

4.6.2 Analysis IV: Low-level wind speed

Analysis IV divided the west-southwesterly flow events into epochs based on the magnitude of the 900 – 800 mb wind (Fig. 4.10). Comparing Figs. 4.10a and 4.10c, when the wind was weaker the overall response of the reflectivity was less and more concentrated over the mountains 40 – 60 km east-southeast of the radar. When the wind was stronger, the response over the mountains was stronger 40 – 60 km east-northeast of the radar and over the King Range 20 – 60 km south-southeast of the radar. Under weaker flow (Fig. 4.10a), precipitation was reduced over the low-lying terrain between 30 and 50-km range and 20 and 70° azimuth.

The vertical cross sections in Figs. 4.10b and 4.10d are taken along the red line in the horizontal sections to examine the echo enhancement upwind of the King

Range (x = 110 km), which was orthogonal to the flow and therefore expected to have the strongest orographic effects. The upstream echo enhancement was strong 70 km upstream from the coast (x = 40 km in Figs. 4.10b and 4.10d), where sub-cloud geostrophic adjustment possibly began to influence precipitation in land-falling storm systems. The intensity and upstream extent of this enhanced echo pattern could be exaggerated by bright band contamination, but the upward bulge of the echo contours at that range suggests an abrupt rise of the air offshore, perhaps indicating the onshore low-level flow was bumped upward over a thin surface layer of cooler air, as suggested in Sec. 4.4.

Although the radar data are obscured in some areas by terrain, it appears that the strongest local reflectivity enhancement in Figs. 4.10c and 4.10d occurred at the first large peak of terrain near the coast, similar to the overall mean cross section (Fig. 4.5d). As noted in Sec. 4.4, this maximum and the associated upward bulge of reflectivity contours over this first peak is consistent with the behavior of precipitation enhancement by an unblocked upslope flow (Chapter 3; HJM; Medina and Houze 2003). A secondary maximum of reflectivity occurred at the second major rise of terrain (at ~160 km on the horizontal scale of Figs. 4.10b and 4.10d), probably also as a result of the rise of the unblocked flow over the terrain.

Inland from the first peak of terrain, reflectivity contours sloped upward to near the mean crest of the terrain, indicating a general upward-motion response to the overall mountain barrier. When the flow was stronger (Figs. 4.10c and 4.10d),

the vertical cross section indicated the same echo enhancement features (offshore, over the first peak, and up to the main crestline), but they were all more pronounced. These observations are generally consistent with Sinclair et al. (1997), who concluded that heavier precipitation amounts occurred immediately downwind when the cross-barrier flow was stronger. The mean pattern for the stronger flow (Fig. 4.10d) displays a bright band at the melting level indicating that the enhanced precipitation was basically stratiform, but punctuated by the reflectivity peak at the first and second rises of terrain (x = 110 and 160 km).

4.6.3 Analysis V: Low-level moist Brunt-Väisälä frequency

This analysis shows that upstream enhancement over the ocean was sensitive to the upstream static stability. Figure 4.11 divides the west-southwesterly flow events with the 0°C level ≥2.5 km MSL into unstable/neutral and stable categories. Figures 4.11a and 4.11b show the unstable/neutral cases defined as those for which the moist Brunt-Väisälä frequency was imaginary or zero. Figures 4.11c and 4.11d show the stable cases for which the moist Brunt-Väisälä frequency was greater than zero.

Figure 4.11 illustrates that the reflectivity was stronger everywhere when absolute stability prevailed. In particular, upstream enhancement (seen best along the red line in panels a and c) was stronger under stable conditions (compare panels a-b with c-d). Under stable conditions, the leading edge of the upstream enhance-

ment was marked by a strong gradient of reflectivity. In both vertical cross sections, the leading edge of the offshore enhancement (at about 50 km on the horizontal scale) is marked by an echo maximum and upward protuberance of the reflectivity contours, similar to that seen near the first peak of terrain onshore. While this upstream echo structure may be exaggerated by bright band influences, it suggests the southwesterly flow was responding to an offshore cold pool similar to the way it responded to the terrain proper.

The offshore precipitation between the initial reflectivity core offshore and the first peak of terrain, and between the first and second peaks of terrain, exhibited a stratiform vertical structure with a bright band under both unstable/neutral (Fig. 4.11b) and stable (Fig. 4.11d) conditions. These observations indicate that the coastal terrain, and possible offshore cold pools, were enhancing the basic stratiform precipitation structure of the landfalling baroclinic storm systems, and that this overall enhancement was punctuated by sudden upward responses of the flow, first to the leading edge of an offshore cold pool, then to the first and second major rises of terrain. It is possible that the growth of ice particles produced by these sudden rising motions were advected downstream by the strong southwesterly flow to produce enhanced stratiform precipitation analogous to the stratiform precipitation that occurs in the stratiform region of a squall line, downshear from the leading line of convective cells (Houze 1993, Ch. 9). Such a growth and fallout pattern would

account for the enhanced stratiform precipitation between the three primary reflectivity cores in Figs. 4.11b and 4.11d.

Further insight is achieved by subdividing the reflectivity data into bins A, B, and C shown in Figs. 4.11a and 4.11c A comparison of echo frequencies during neutral or unstable events (Fig. 4.12a) and stable events (Fig. 4.12b) at bin A (upstream from the terrain) suggests that precipitation was more frequent when the flow was statically stable. Over land (bins B and C), echo frequencies were skewed towards lower values when the flow was unstable/neutral (Fig. 4.12a) and towards higher values (Fig. 4.12b) when stable. These results suggest that precipitation on the whole was more frequent *and* heavier during stable events.

Figure 4.13 shows the average Doppler radial velocity along a southwest-northeast cross section passing through the radar site for unstable/neutral and stable conditions. Both sections show strong southwesterly flow increasing gradually with height. The flow was slightly less intense in the stable cases but nevertheless rapidly moving over the coast and up over the mountains. These sections are consistent with unblocked flow. Thus, as noted above, the upstream enhancement seen in Fig. 4.11d must be occurring in an essentially unblocked flow. The radial velocity sections do not extend below the 1-km level, so the possibility that the flow in the section was lifted over a shallow coastal marine layer cannot be determined. However, Neiman et al. (2002; 2004) observed near-surface blocked flow along the West Coast that enhanced upstream precipitation in much the same way.

Average hourly profiles of Doppler vertical velocity of precipitation from a 915-MHz wind profiler at Eureka, CA, during stable (solid) and unstable (dashed) heavy rain events are shown in Fig. 4.14. The measured Doppler velocity is a result of the combination of vertical air motion and particle fall speed. The figure clearly shows that downward Doppler vertical velocities were about 0.5 m s^{-1} weaker in stable air than in neutral/unstable conditions. This result, combined with higher reflectivity values observed during stable events (Fig. 4.11c), indicates either that precipitation particles under absolutely stable conditions may be smaller and more numerous within similar ambient upward air motions, or that the particles are larger but with significantly stronger ambient upward motion. The latter explanation is more consistent with the findings of White et al. (2003), who suggested that stratiform precipitation consisted of fewer, larger raindrops.

The strong sensitivity of precipitation to static stability apparently contributed to a diurnal precipitation cycle in Northern California that agreed well with diurnal patterns observed during MAP (HJM). Fig. 4.15 depicts the average rainfall observed per hour at 2.0 km altitude during the 61 rain days, estimated using a standard *Z-R* relationship (Marshall and Palmer 1948). A maximum was observed between 3 and 9 am Pacific Standard Time (PST), with up to 60% more rainfall in the morning than other hours of the day. Higher stability combined with higher relative humidity several hours before and after dawn probably generated this diur-

nal response, which occurred 2-3 hours earlier than the diurnal peak observed during MAP (HJM).

4.7 Summary

Radar reflectivity and Doppler velocity archives obtained during 61 major rain days along the coast of Northern California during the period 1 October 1995 – 31 March 1998 by the WSR-88D at Eureka, California, reveal the orographic precipitation pattern of the region. The major rain events occurred during southwesterly flow characterized by a low-level jet (LLJ) and a high influx of tropical moisture as described by Ralph et al. (2004). The average speed of the LLJ (observed by Doppler radar) was ~20 m s^{-1}. South of Eureka the southwesterly LLJ was perpendicular to a series of two-dimensional mountain ridges. Orographic enhancement of the precipitation occurred both over the coastal mountain ranges and upstream over the ocean. Climatologically, the upstream enhancement occurred within about 150-km of the crest of the Coastal Range (about 60 km upstream from the coast), consistent with geostrophic adjustment theory. However, the impinging flow (above the 1-km level) was strong enough to be unblocked by the terrain, and the occurrence of the upstream enhancement was in this respect unexpected. It is possible that a thin layer of cold marine air (<1 km deep) was dammed against the coastal mountains, and the unblocked flow lifting over the cold pool was enough to produce upstream

enhancement, although bright-band contamination may have exaggerated the upstream extent and intensity of the observed echo enhancement.

Vertical cross sections through the climatological echo pattern of the heavy rain events were generally stratiform in character from over the ocean to inland over the mountains. Directly over the mountains, the broad pattern of the mean reflectivity field on the scale of the overall region of coastal mountains showed upward sloping echo contours indicative of a general upslope orographic enhancement. This basic stratiform echo pattern over the mountains was interrupted by an embedded core of maximum mean reflectivity over the first major peak of terrain encountered by the unblocked flow. This core was the strongest feature of the orographic precipitation pattern. Under strong wind conditions this core was advected slightly downwind of the first peak. This mean embedded echo core had a maximum intensity at low levels (below the 0°C level) but extended to high levels, to near the top of the layer of echo.

A mean echo core observed at the first major peak of terrain, embedded in a broader stratiform echo structure, has also been observed in the European Alps (Chapter 3; HJM; Medina and Houze 2003). The precipitation growth processes contributing to this echo core over the first major peak of terrain in the Alps were determined to be coalescence below the 0°C level and riming just above the 0°C level (Medina and Houze 2003; Yuter and Houze 2003). Similar processes probably were active in the heavy rain events over the California Coastal Range. White et al.

(2003) also concluded that low-level growth by coalescence was important in precipitation over the California Coastal Range.

A secondary echo core occurred over the second major peak of the coastal mountain terrain. It was similar to the core over the first peak of terrain, but not as intense. Interestingly, an embedded echo core was also observed over the ocean at the leading edge of the upstream enhancement of radar echo, although bright band contamination may have exaggerated this echo pattern. The upstream echo core could be an indication that the unblocked cross-barrier flow was bumped upward over a thin layer of cold marine air lying out ahead of the coastal mountains. The pool of cold marine air would have acted as a barrier to the oncoming unblocked flow in much the same way as the coastal mountains. The stratiform radar echo between the offshore core and the echo core over the first peak of inland terrain, and between the cores located over the first and second peaks of inland terrain was probably enhanced by ice particles grown in the cores and advected downwind to seed and thus intensify the intervening stratiform precipitation. Additional observational data are needed to confirm the presence of near-surface cold air damming offshore and to illuminate the microphysical growth mechanisms contributing to the echo patterns observed in this chapter.

The orographically enhanced precipitation and associated upstream, offshore, enhanced precipitation were stronger when the upstream flow was stronger or when the lower atmosphere was statically stable as opposed to neutral or slightly

conditionally unstable. The similarity in the synoptic patterns between stable and neutral/unstable events suggests that this latter result may be in response to orographic influences. Stable conditions may conform the flow and associated precipitation more tightly to the topography. The slight instability in some cases may have produced somewhat more random patterns, less coherent to the topography. The sensitivity of the orographic response to stability was evidently sufficiently strong to have produced a diurnal cycle with a peak of echo intensity in the early morning (more stable) times.

Table 4.1. Heavy rain events identified during the period 1 October 1995 – 31 March 1998 for which WSR-88D radar archives were available.

1995	1996	1997	1998
11 Dec 1995	15 Jan 1996	1 Jan 1997	2 Jan 1998
12 Dec 1995	16 Jan 1996	16 Mar 1997	3 Jan 1998
14 Dec 1995	18 Jan 1996	18 Apr 1997	11 Jan 1998
15 Dec 1995	27 Jan 1996	3 Jun 1997	12 Jan 1998
	4 Feb 1996	8 Oct 1997	14 Jan 1998
	17 Feb 1996	15 Nov 1997	16 Jan 1998
	18 Feb 1996	16 Nov 1997	18 Jan 1998
	19 Feb 1996	26 Nov 1997	25 Jan 1998
	20 Feb 1996	29 Nov 1997	26 Jan 1998
	4 Mar 1996	7 Dec 1997	1 Feb 1998
	21 May 1996	14 Dec 1997	2 Feb 1998
	17 Nov 1996		3 Feb 1998
	18 Nov 1996		5 Feb 1998
	19 Nov 1996		6 Feb 1998
	4 Dec 1996		7 Feb 1998
	7 Dec 1996		14 Feb 1998
	8 Dec 1996		16 Feb 1998
	9 Dec 1996		19 Feb 1998
	10 Dec 1996		21 Feb 1998
	26 Dec 1996		12 Mar 1998
	29 Dec 1996		21 Mar 1998
	30 Dec 1996		22 Mar 1998
	31 Dec 1996		23 Mar 1998

Table 4.2. Superposed epoch analyses. Shown are the criteria used to separate the WSR-88D radar archive into epochs for superposed analysis I – V. Also tabulated are the number of hourly radar volumes used for each analysis and all corresponding figures.

Analysis	Epoch 1	Epoch II	Epoch III	Epoch IV
I. 500 – 700 mb wind speed (low-level wind direction 225 – 270°; FZL ≥2.5km)	0 – 30 m s^{-1} 125 vol. Fig. 4.6a, b	30 m s^{-1} – ∞ 103 vol. Fig. 4.6c, d		
II. 500 – 700 mb dew-point depression (low-level wind direction 225 – 270°; FZL ≥2.5km)	3°C – ∞ 104 vol. Fig. 4.7a, b	0 – 3°C 124 vol. Fig. 4.7c, d		
III. 900 – 800 mb wind direction	180 – 210° 54 vol. Fig. 4.9a	210 – 240° 330 vol. Fig. 4.9b	240 – 270° 362 vol. Fig. 4.9c	270 – 300° 235 vol. Fig. 4.9d
IV. 900 – 800 mb wind speed (low-level wind direction 225 – 270°; FZL ≥2.5km)	0 – 20 m s^{-1} 104 vol. Fig. 4.10a, b	20 m s^{-1} – ∞ 130 vol. Fig. 4.10c, d		
V. 900 – 800 mb moist Brunt-Väisälä frequency (low-level wind direction 225 – 270°; FZL ≥ 2.5km)	Imag. – 0 s^{-1} 153 vol. Figs. 4.3c, d; 4.4b; 4.11a, b; 4.12a; 4.13a; 4.14	0 s^{-1} – ∞ 81 vol. Figs. 4.3e, f; 4.4c; 4.11c, d; 4.12b; 4.13b; 4.14		

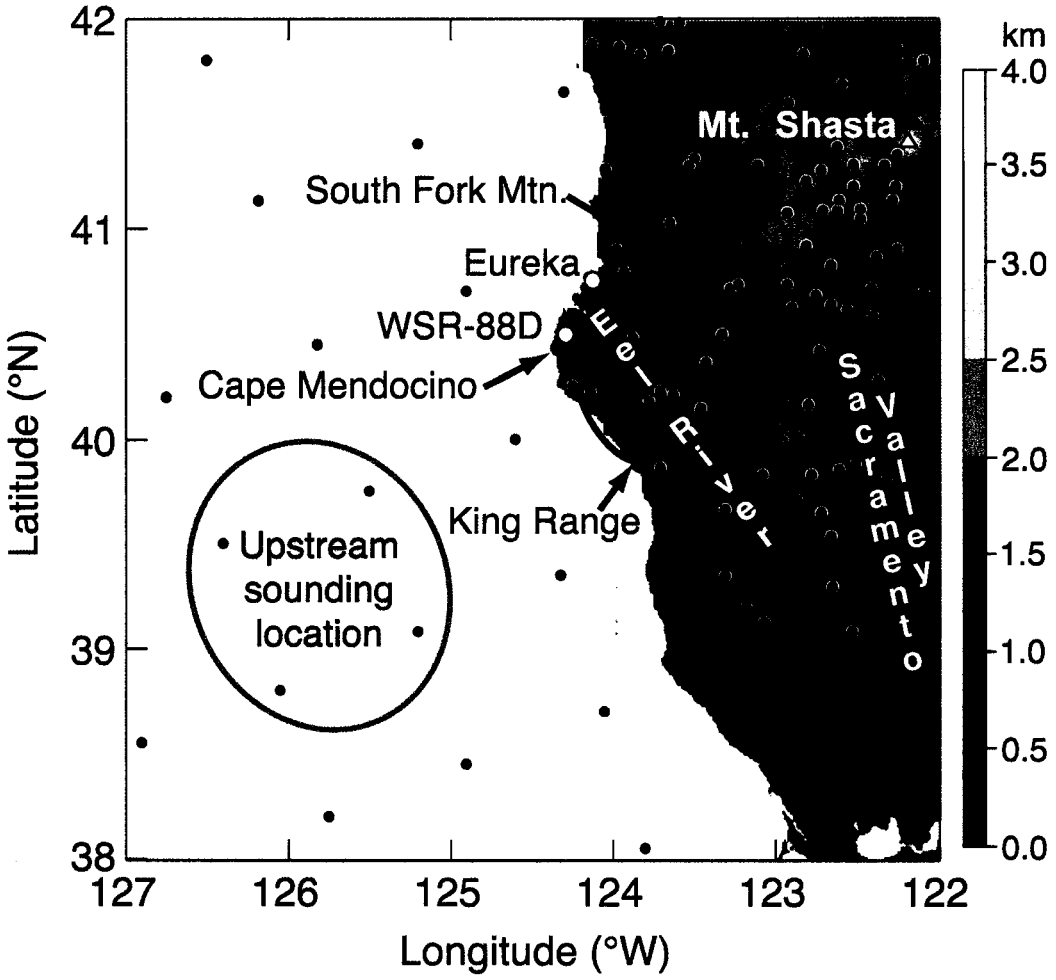

Figure 4.1. Digital terrain map of coastal Northern California, with terrain elevation (km above MSL) shaded. The locations of important geographic features and the Eureka WSR-88D are labeled. White circles over land represent automated rain-gauge stations; black dots over ocean depict the locations of Eta-model gridpoints. The four points enclosed by the ellipse were horizontally averaged to produce a synthetic sounding representative of the upstream flow.

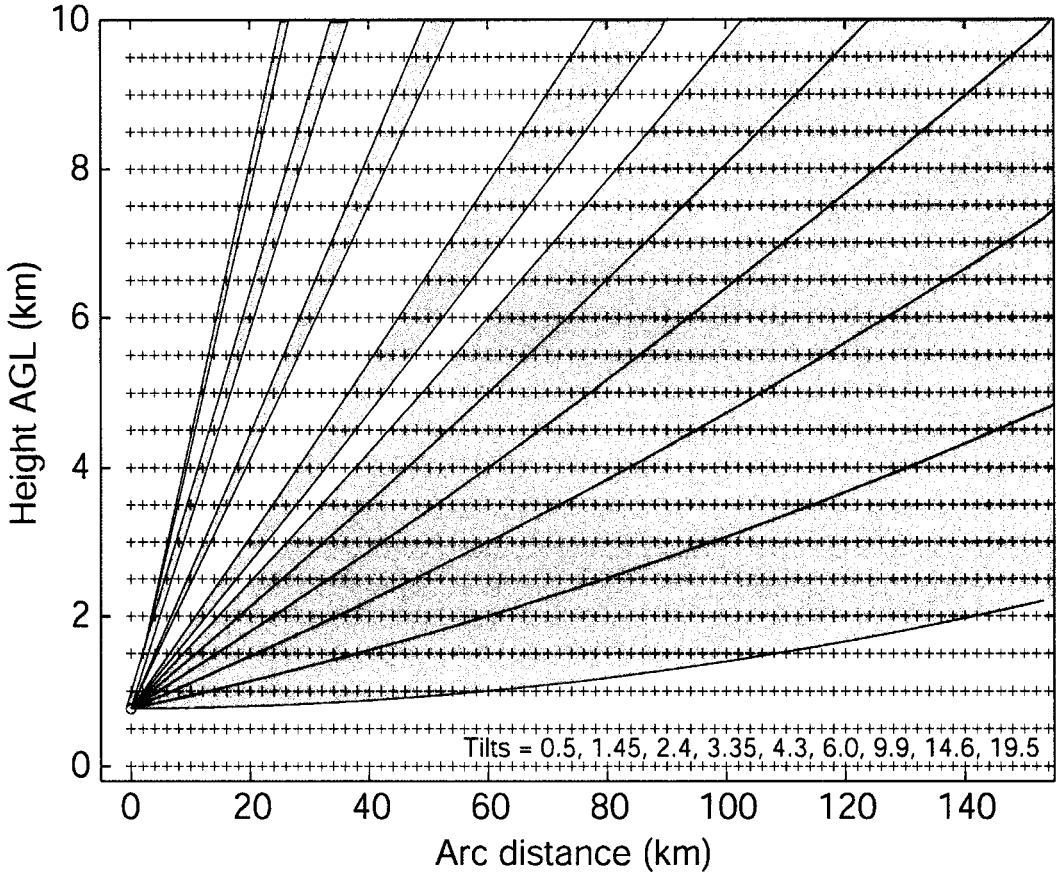

Figure 4.2. Height vs. range representation of the Eureka WSR-88D tilt sequence looking east from the radar site (indicated by the open circle at 767-m altitude and 0-km range). Each radar tilt is shaded, and interpolation grid points are indicated by '+' (after James et al. 2000).

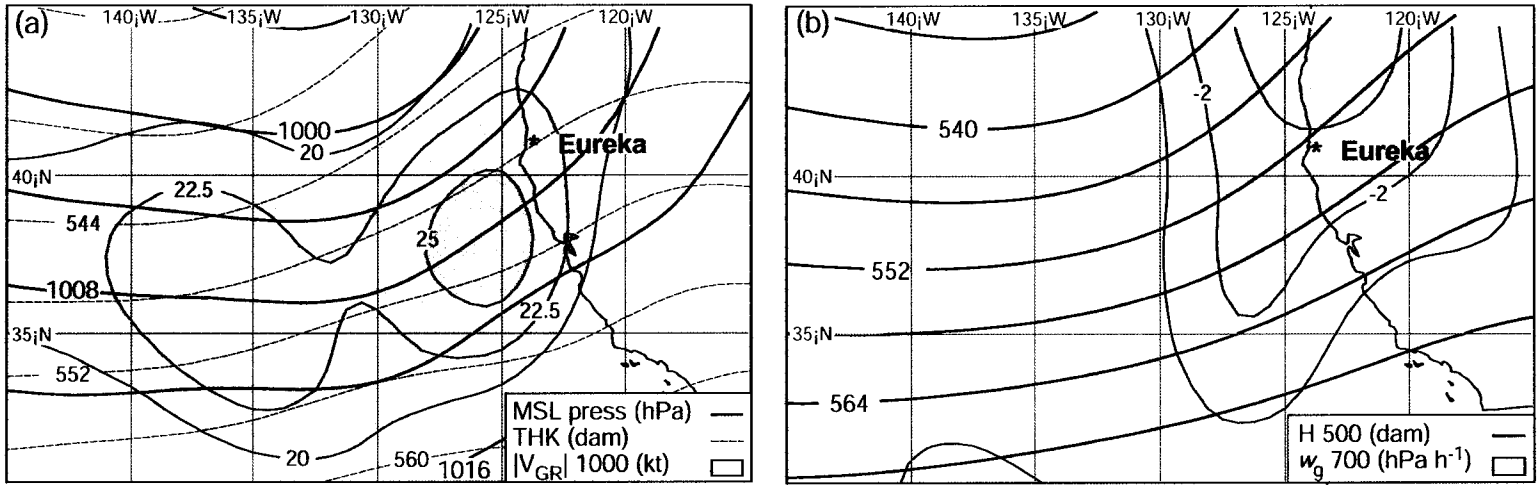

Figure 4.3. Mean NCEP reanalysis fields, averaged over 61 heavy precipitation events during the period 1 Oct 1995 – 31 Mar 1998. Panel (a) depicts MSL pressure [mb] (solid), 1000 – 500 mb thickness [dm] (dashed), and isotachs of gradient wind [kt] (shaded). Panel (b) shows 500-mb height [dm] (solid) and ω [mb/h] (shaded). Composite synoptic patterns are shown in (c) and (d) for the subset of heavy rain events that had neutral or unstable west-southwesterly flow in the 900 – 800 mb layer, with the 0°C level above 2.5 km MSL. Panels (e) and (f) are identical to (c) and (d), respectively, with the exception that only stable events are shown.

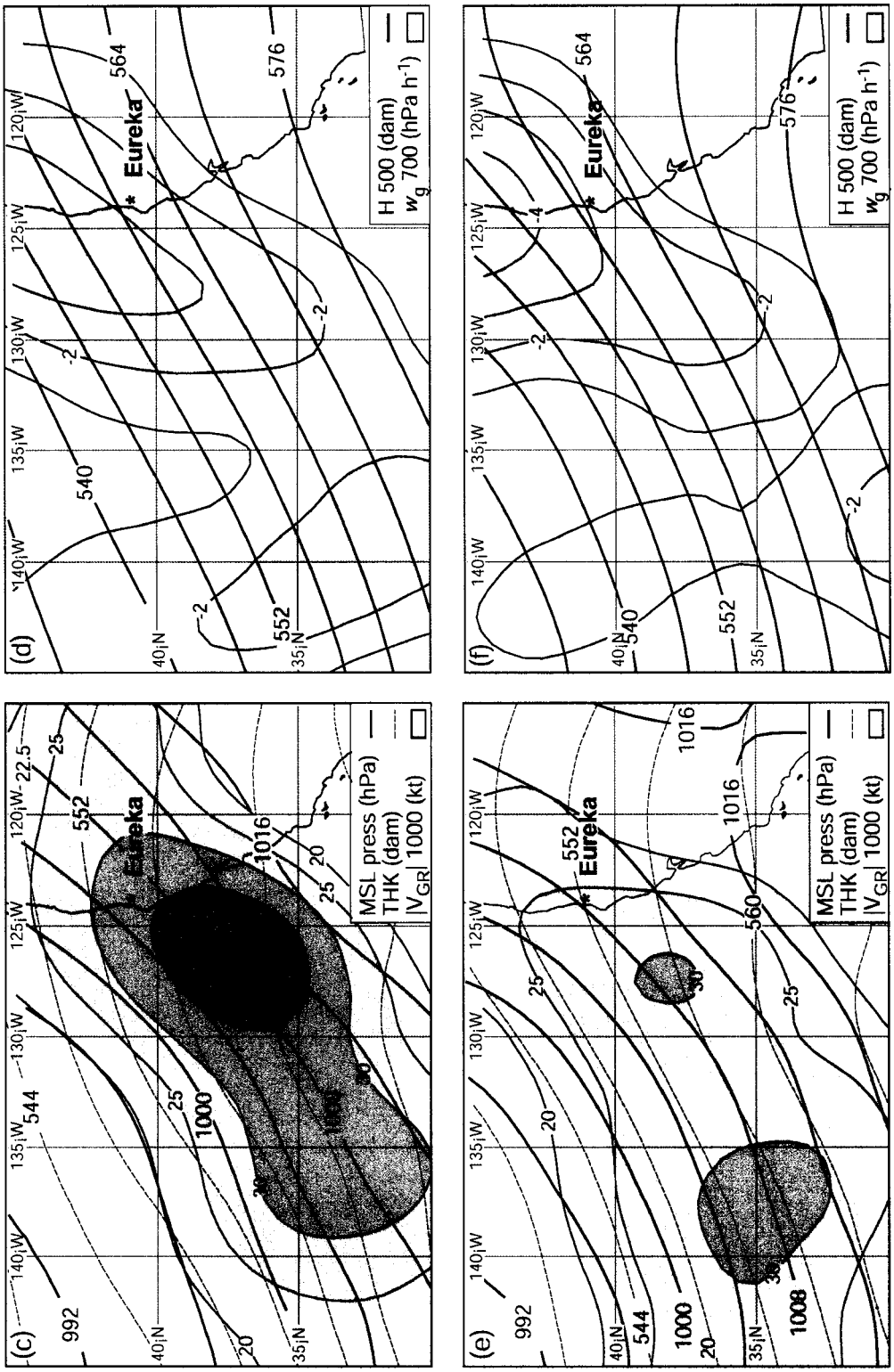

Figure 4.3. (continued)

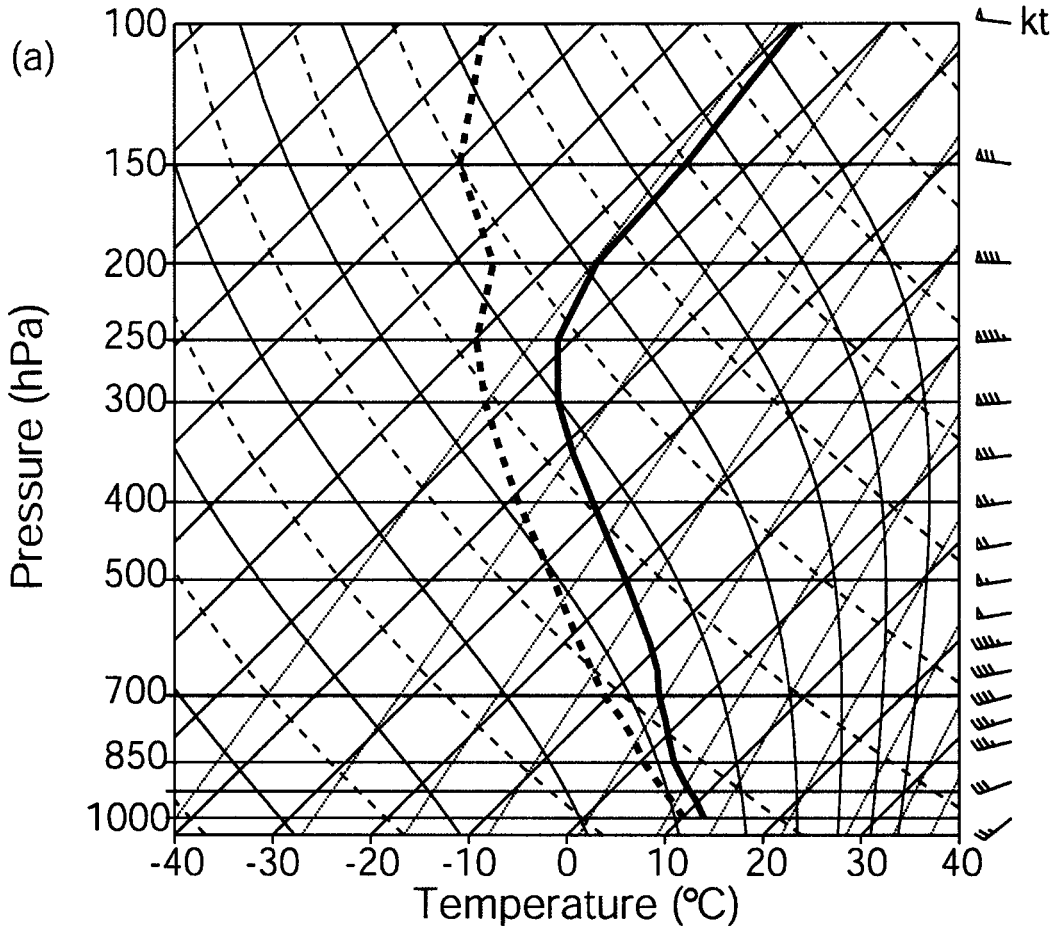

Figure 4.4. Mean Eta-derived sounding (see location in Fig. 4.1) representing impinging upstream flow, averaged over all 61 heavy precipitation days. Mean soundings are also shown for rain events with (b) neutral/unstable and (c) stable west-southwesterly 900 – 800 mb flow (0°C level above 2.5 km MSL). The temperature [°C] profile is solid, the dew-point temperature [°C] is dashed, and wind speeds are in knots.

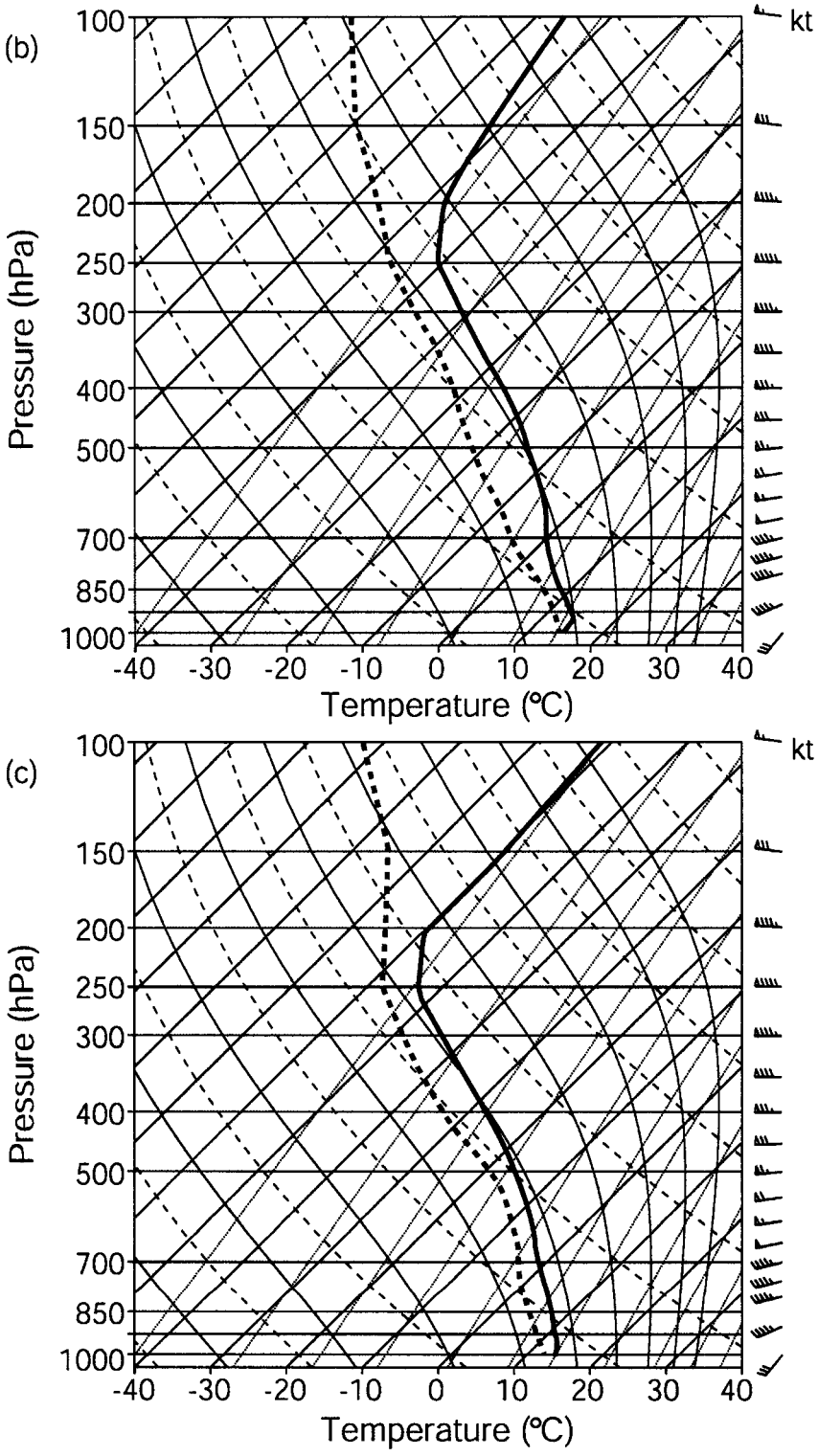

Figure 4.4. (continued)

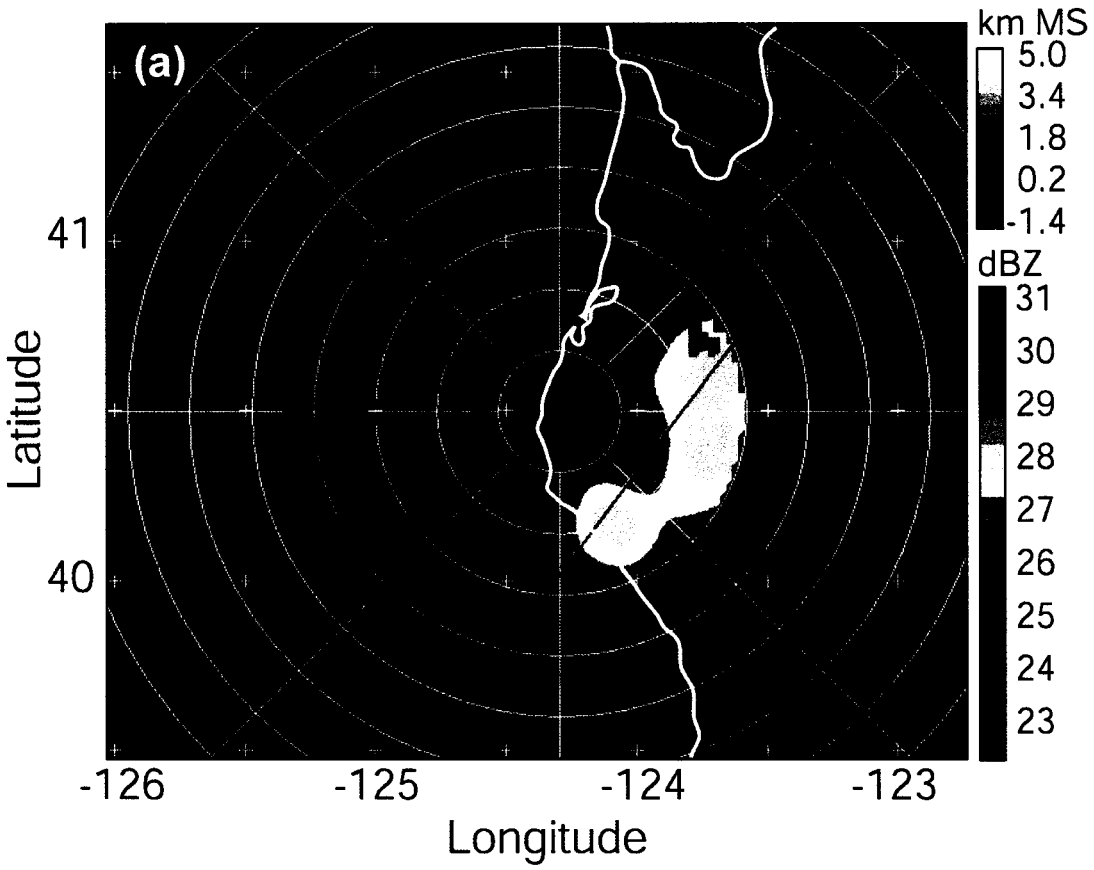

Figure 4.5. Shown is the Eureka WSR-88D radar-derived precipitation climatology obtained for all heavy precipitation events. Constant altitude plots at an altitude of 2.0 km depict (a) mean reflectivity [dBZ], (b) the rainfall frequency, or percentage of radar volumes in which the reflectivity was at least 13 dBZ, and (c) mean Doppler radial velocity [m s^{-1}]. Negative (positive) radial velocity indicates flow towards (away from) the radar. Range ring spacing is 20 km, and azimuth lines are drawn every 45°. The thick white contour represents the coastline. In (c), a vertical cross-section plot of mean reflectivity [dBZ] is shown from southwest to northeast along the red line in (a), with the underlying terrain shaded green.

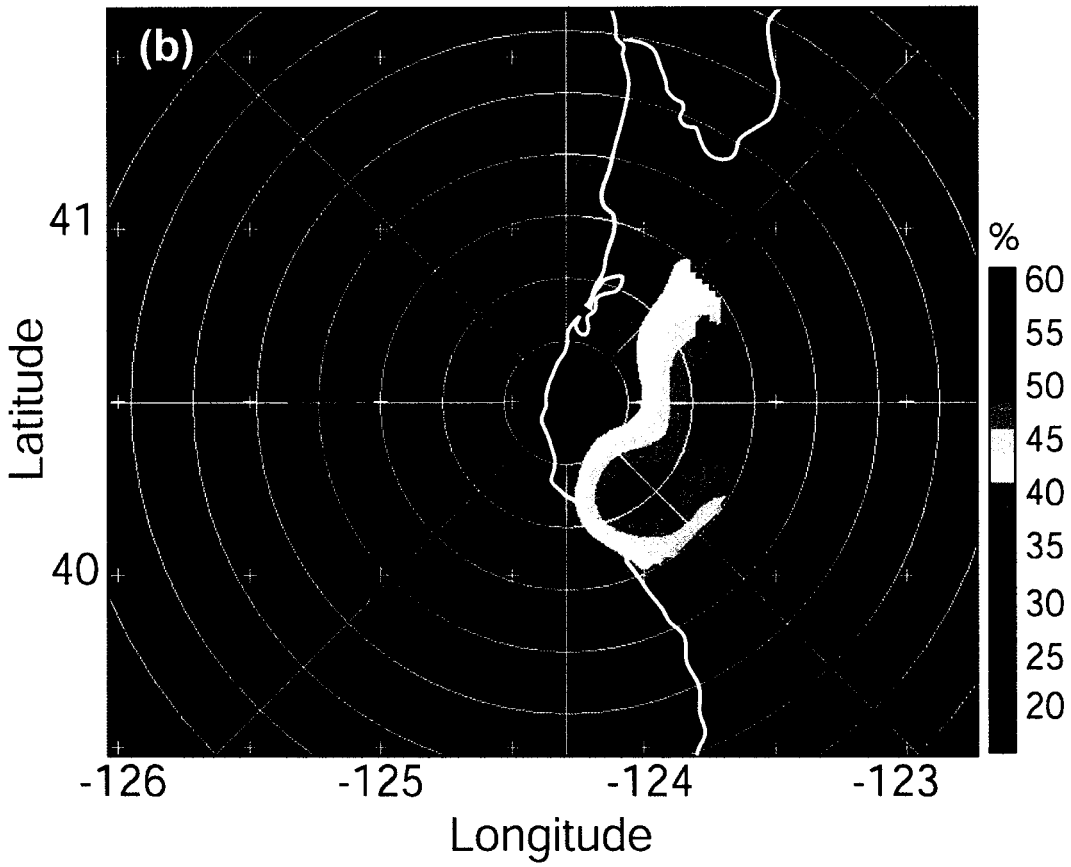

Figure 4.5. (continued)

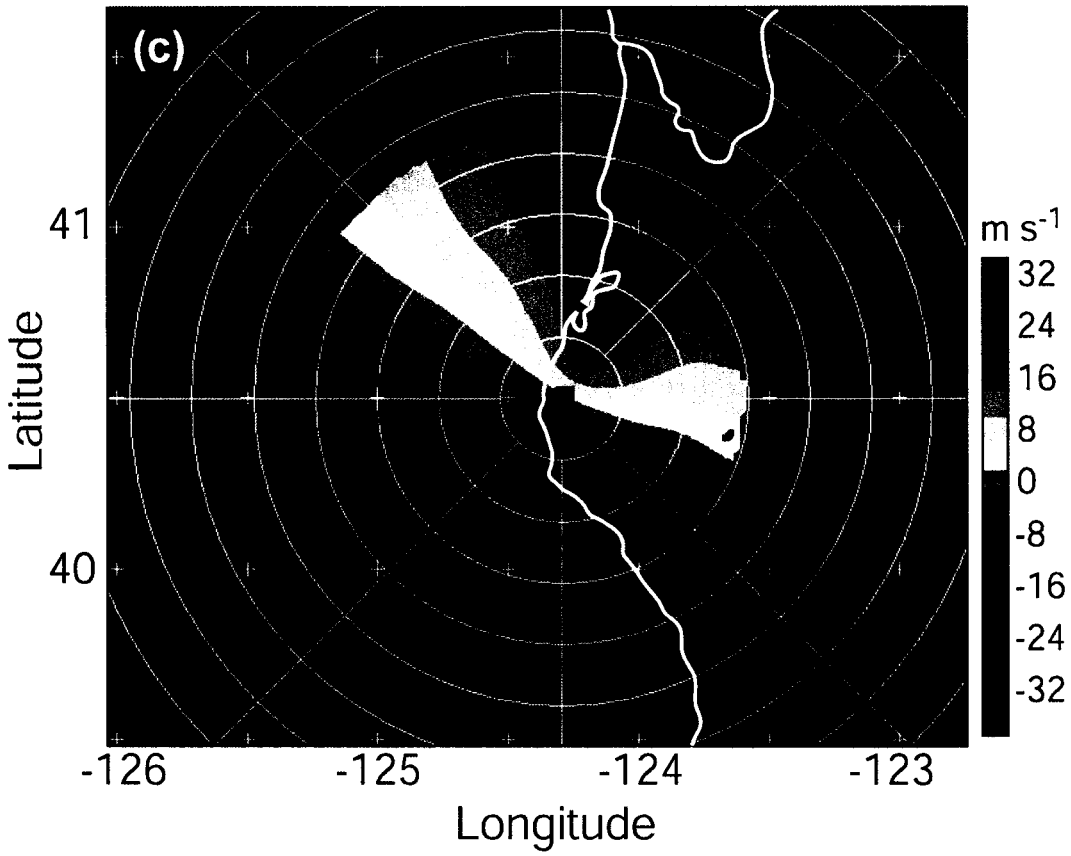

Figure 4.5. (continued)

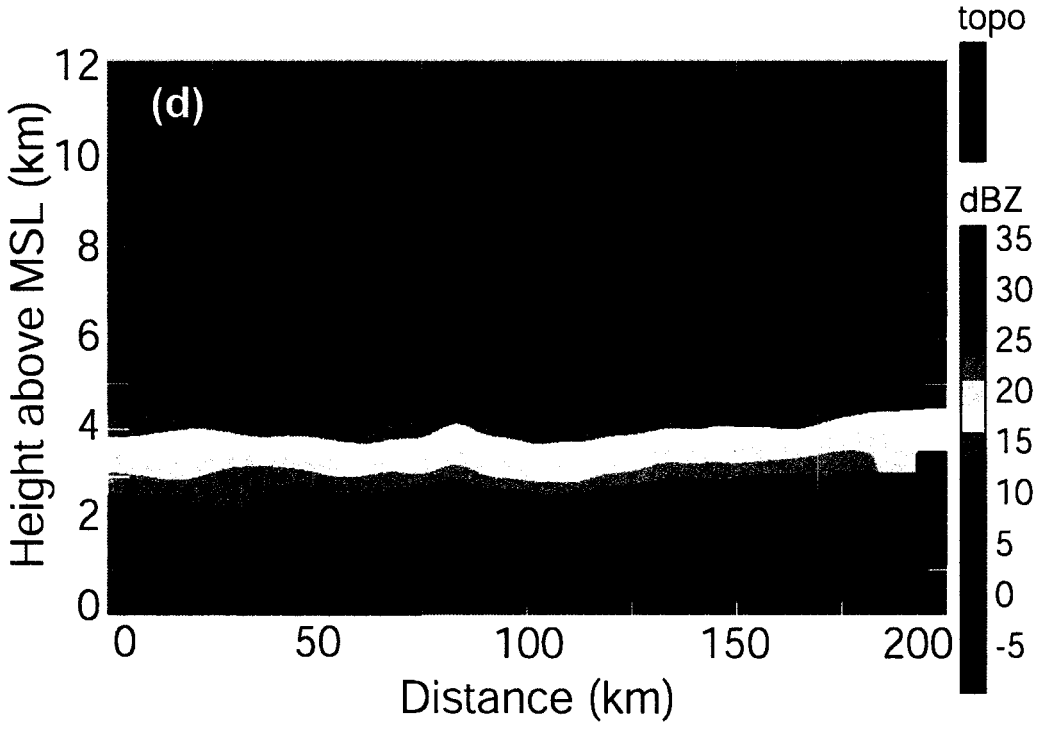

Figure 4.5. (continued)

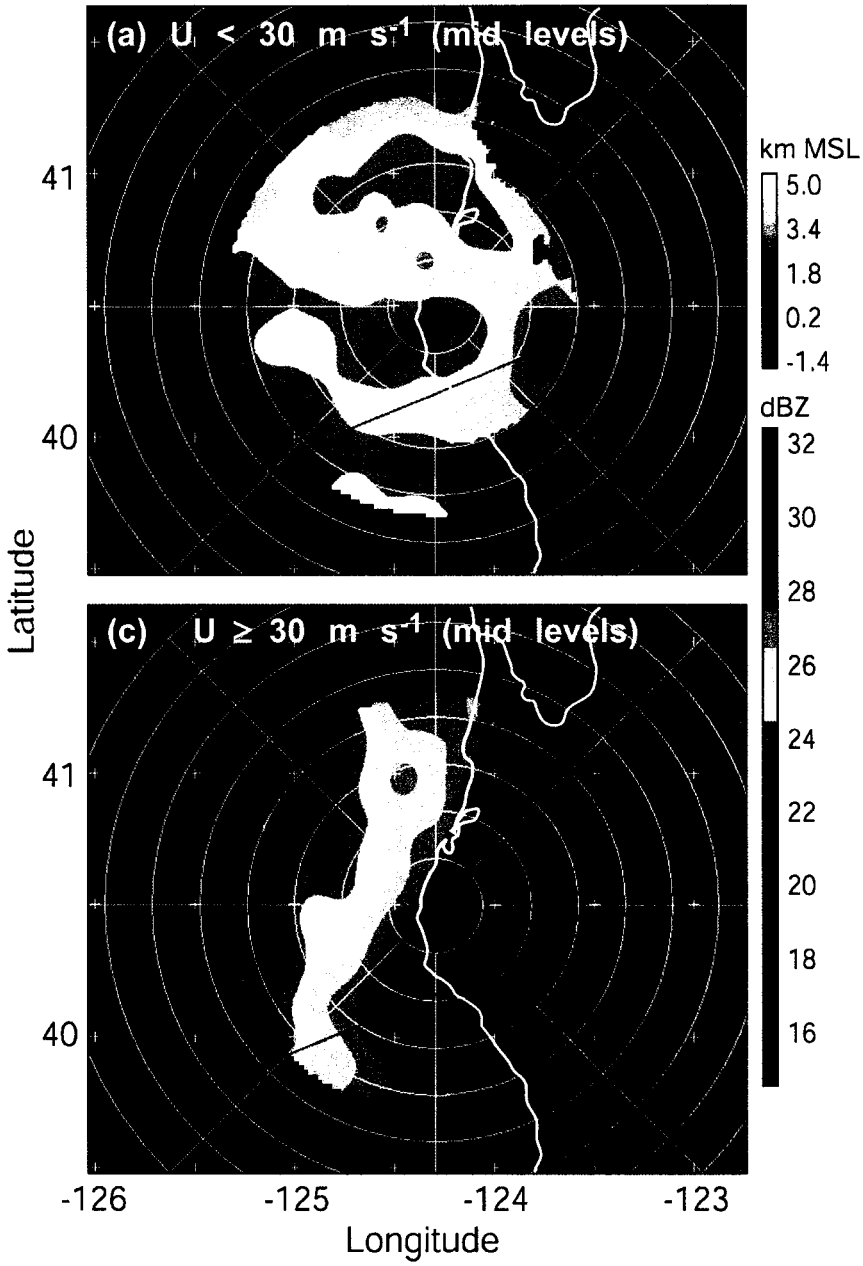

Figure 4.6. For the subset of hourly radar volumes during heavy rain events in which the 900 – 800 mb wind direction fell between 225° and 270° and the 0°C level was at least 2.5 km, this analysis shows the mean reflectivity [dBZ] at 2 km MSL when the layer-averaged 700 – 500 mb wind speed was (a) less than 30 m s^{-1} and (c) at least 30 m s^{-1}. Vertical cross sections of mean reflectivity from west-southwest to east-northeast along the red lines in (a) and (c) are shown in (b) and (d), respectively, with the underlying terrain profile shaded green. Range ring spacing is 20 km, with azimuth lines drawn every 45°.

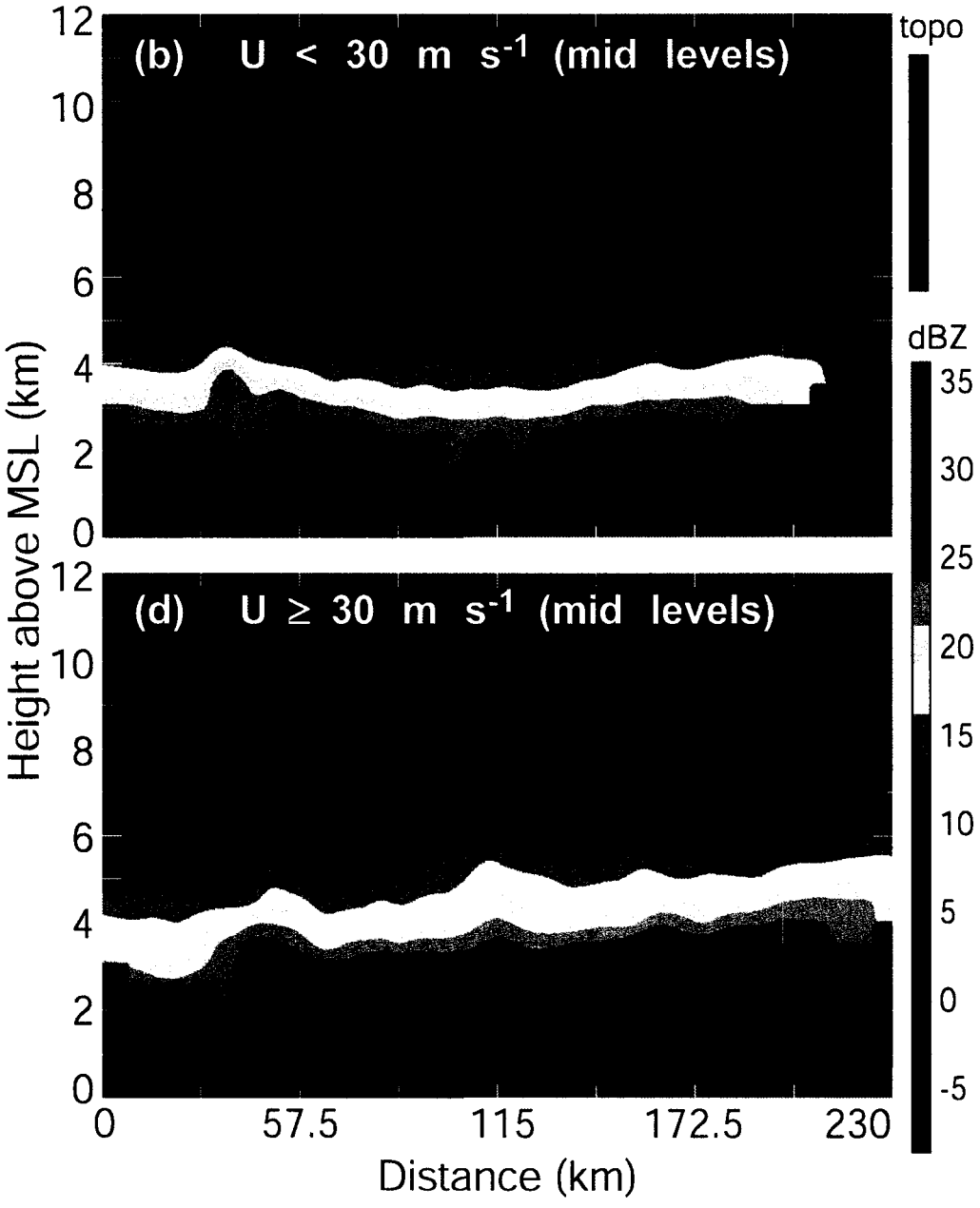

Figure 4.6. (continued)

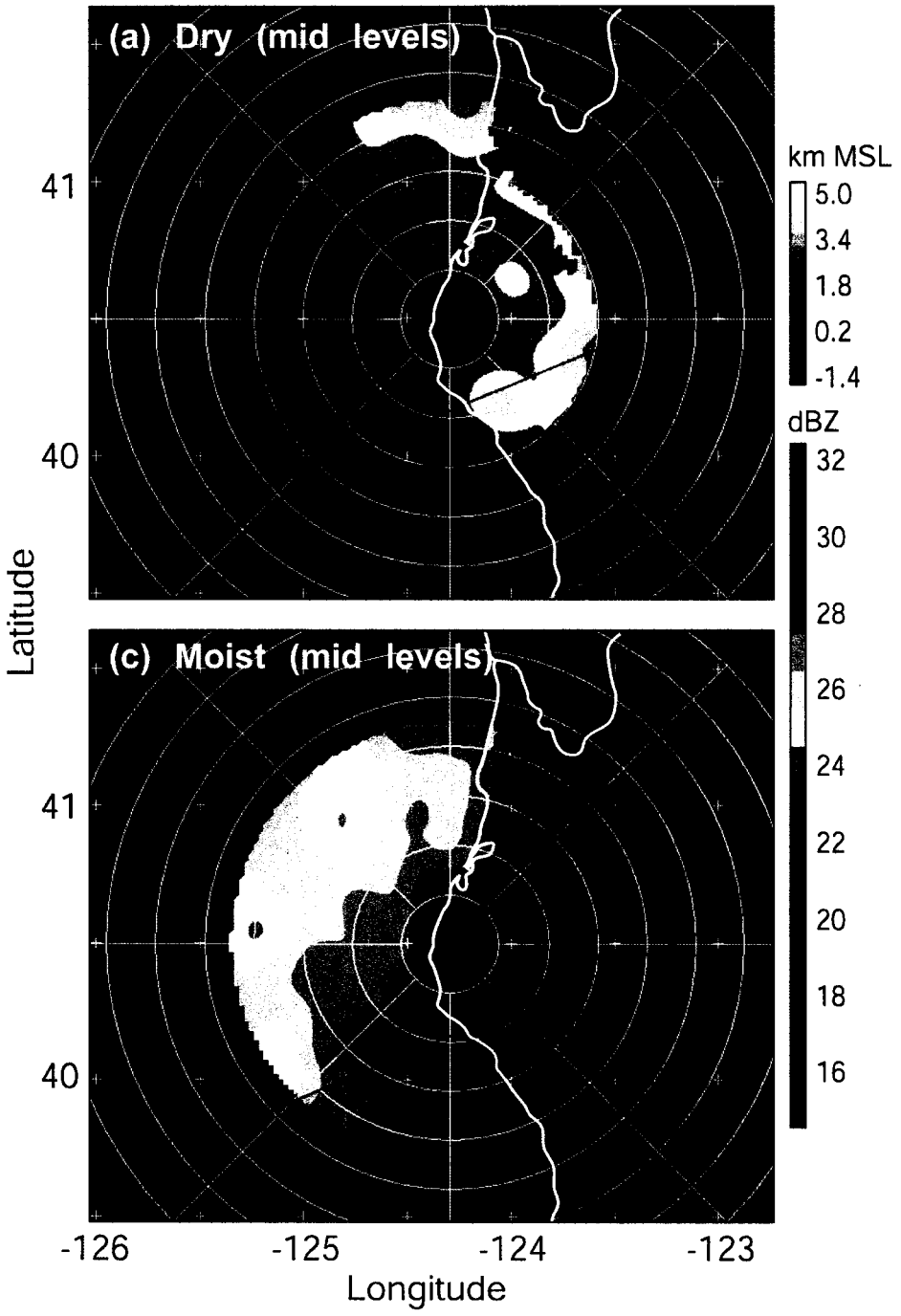

Figure 4.7. As in Fig. 4.6, with the exception that the mean reflectivity [dBZ] is depicted for the subset of hourly radar volumes during heavy rain events when the 700 – 500 mb layer-averaged dew-point depression was (a) at least 3°C and (c) less than 3°C. Panels (b) and (d) contain vertical cross sections respective to (a) and (c).

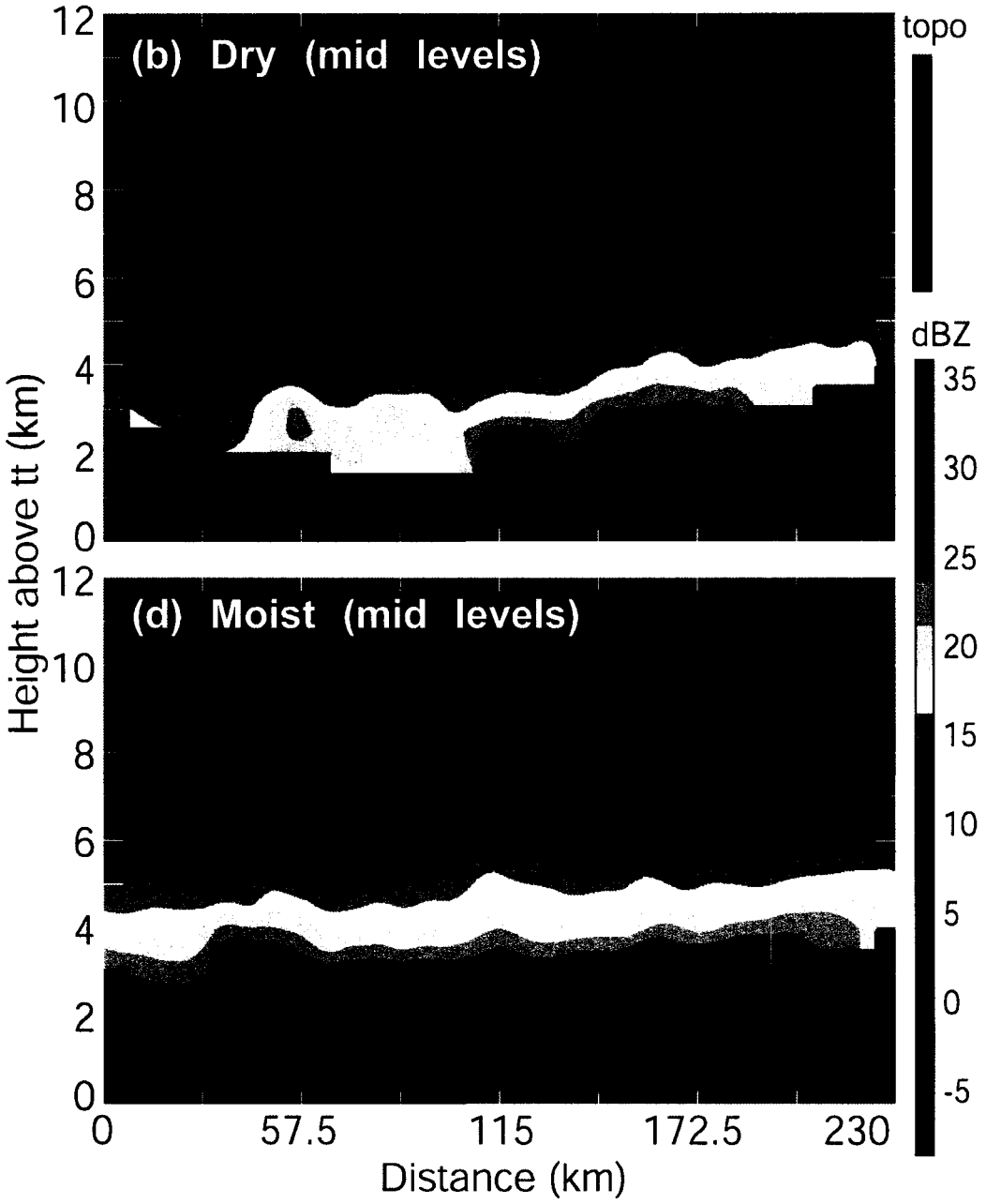

Figure 4.7. (continued)

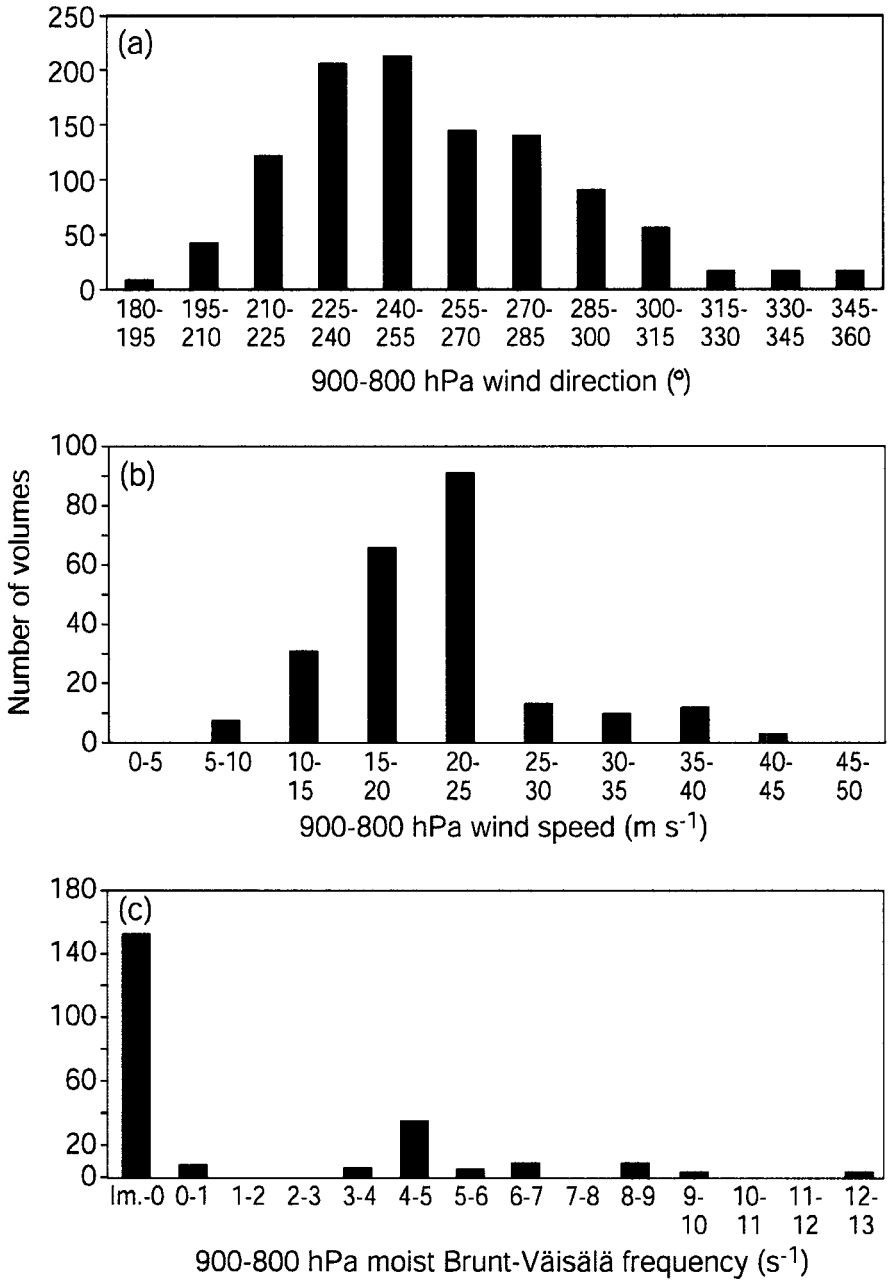

Figure 4.8. Histograms depicting the number of hourly WSR-88D volumes in the heavy rain radar archive vs. the Eta-derived layer-averaged 900 – 800 mb (a) wind direction [°], (b) wind speed [m s^{-1}], and (c) moist Brunt-Väisälä frequency [s^{-1}]. Wind speed and moist Brunt-Väisälä frequency are shown for only west-southwesterly events (225-270°) when the 0°C level was at least 2.5 km MSL.

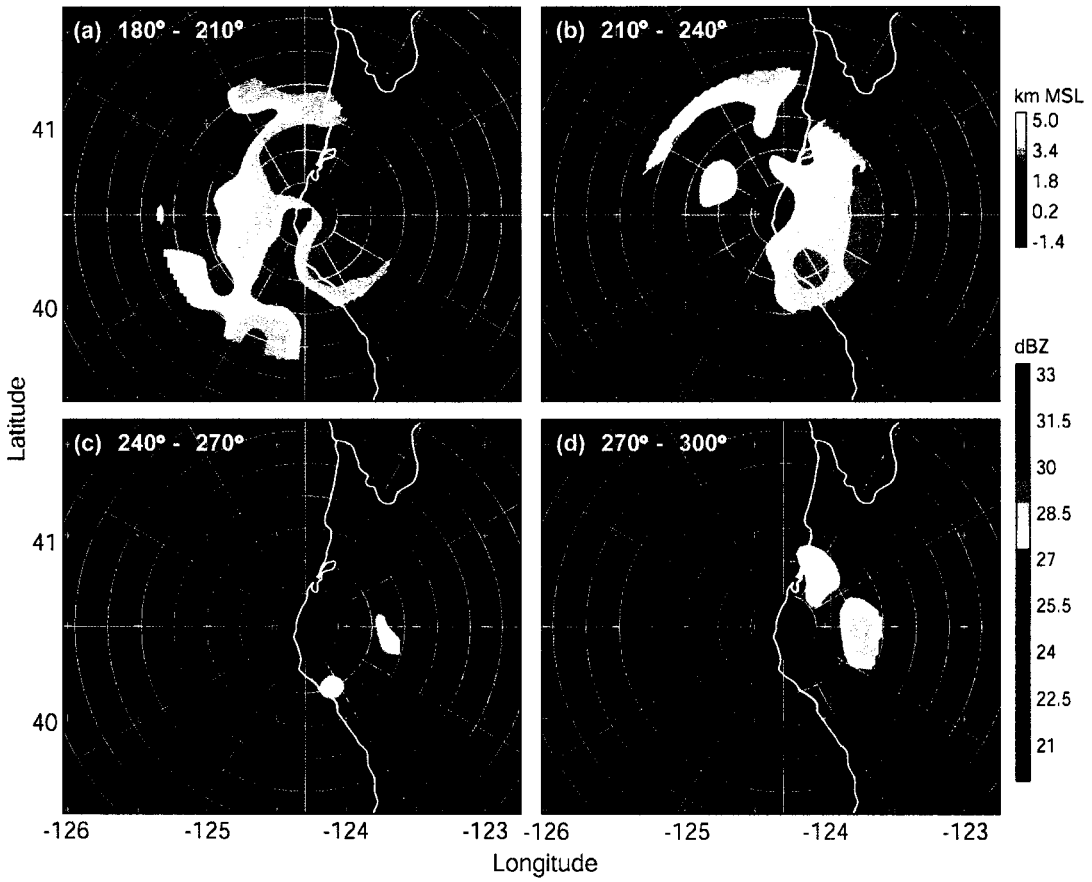

Figure 4.9. Superposed epoch analysis of mean hourly reflectivity [dBZ] at an altitude of 2.0 km MSL during heavy rain events when the 900 – 800 mb flow direction upstream was (a) south-southwesterly (180 – 210°); (b) southwesterly (210 – 240°); (c) west-southwesterly (240 – 270°); and (d) west-northwesterly (270 – 300°).

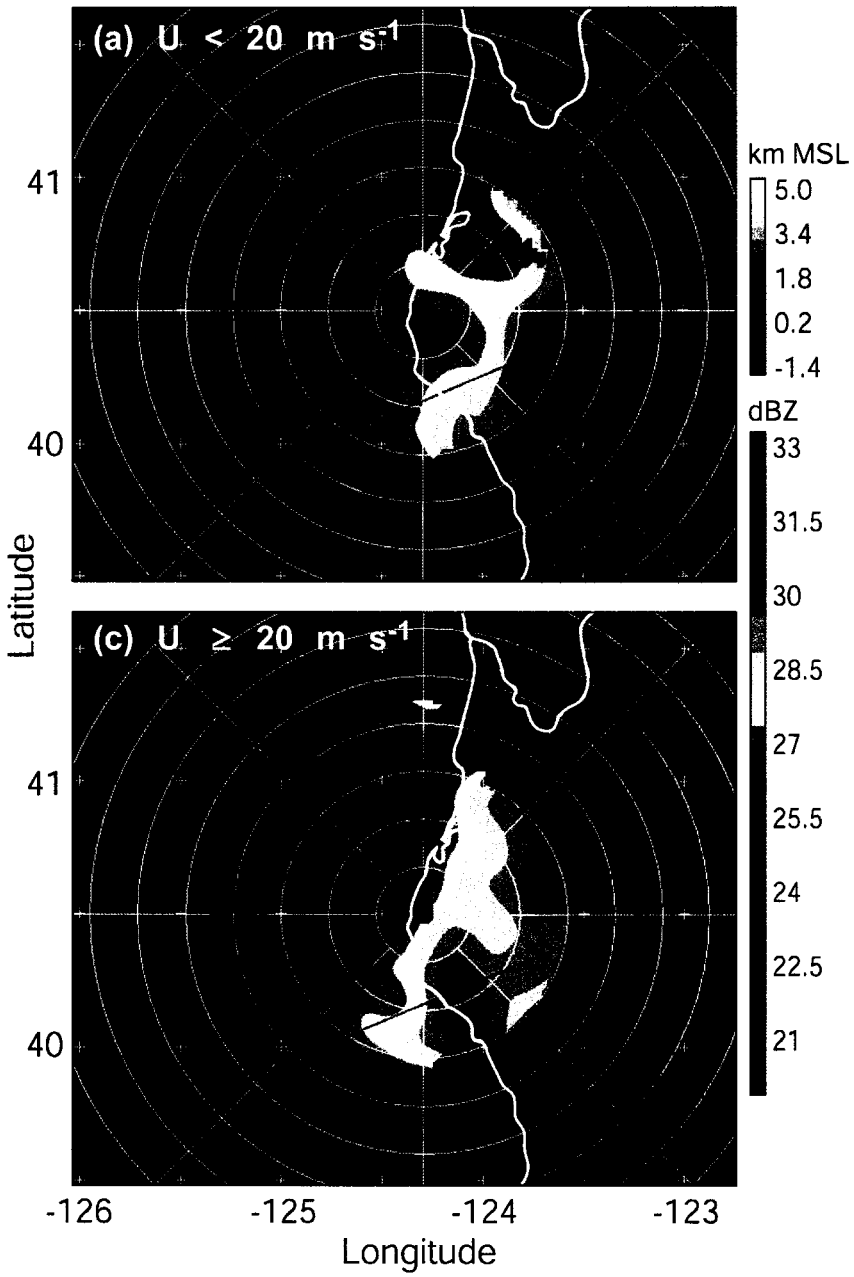

Figure 4.10. Of those hourly radar volumes whose 900 – 800 mb wind direction was west-southwesterly (between 225 and 270° azimuth) and the 0°C level was at least 2.5 km MSL, this analysis depicts the mean reflectivity [dBZ] at 2.0 km altitude during heavy rain events when the layer-averaged 900 – 800 mb wind speed was (a) < 20 m s^{-1} and (c) ≥20 m s^{-1}. Vertical cross-section plots from west-southwest to east-northeast along the red segments (a) and (c) are shown in (b) and (d) respectively, with the underlying terrain shaded green.

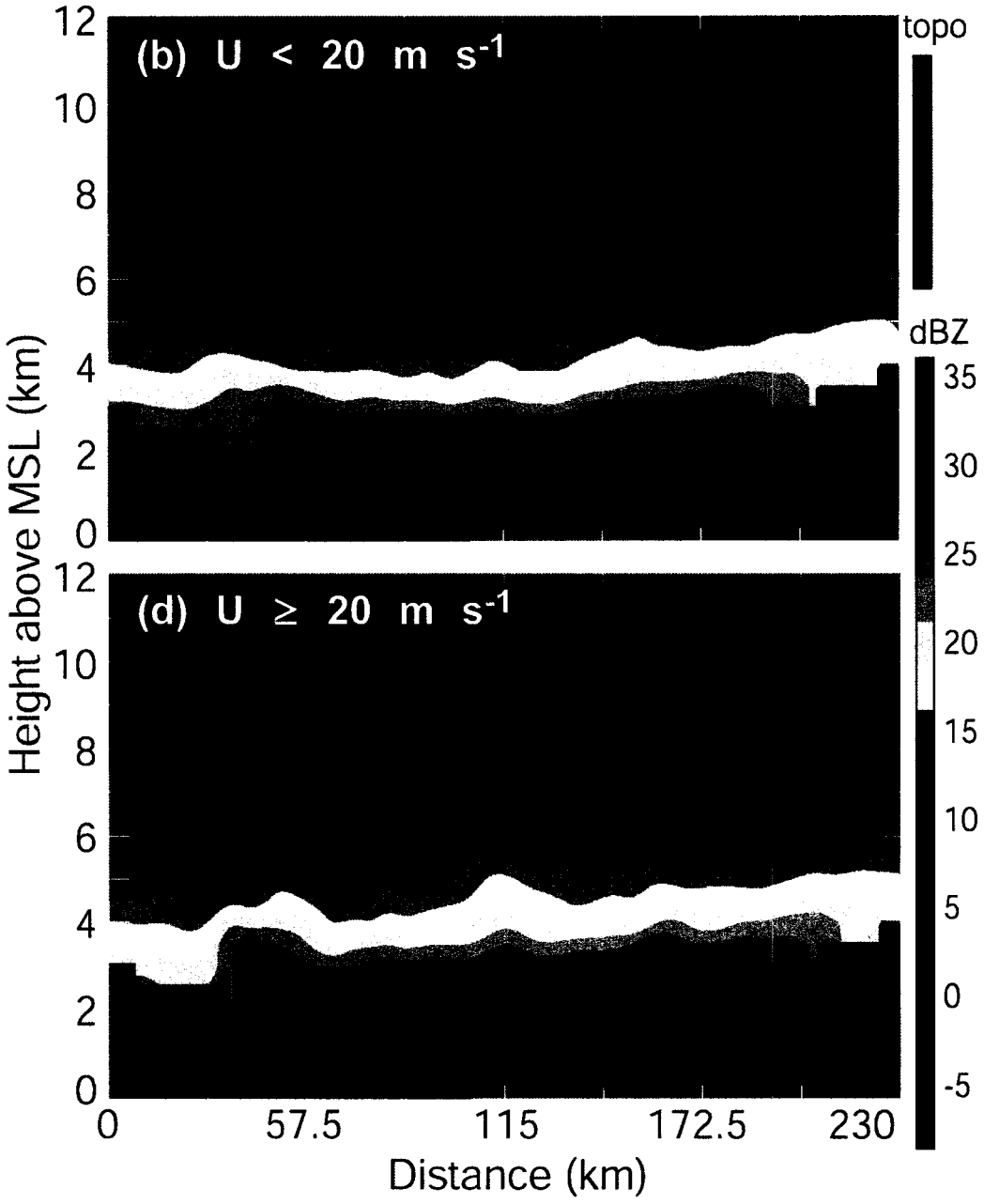

Figure 4.10. (continued)

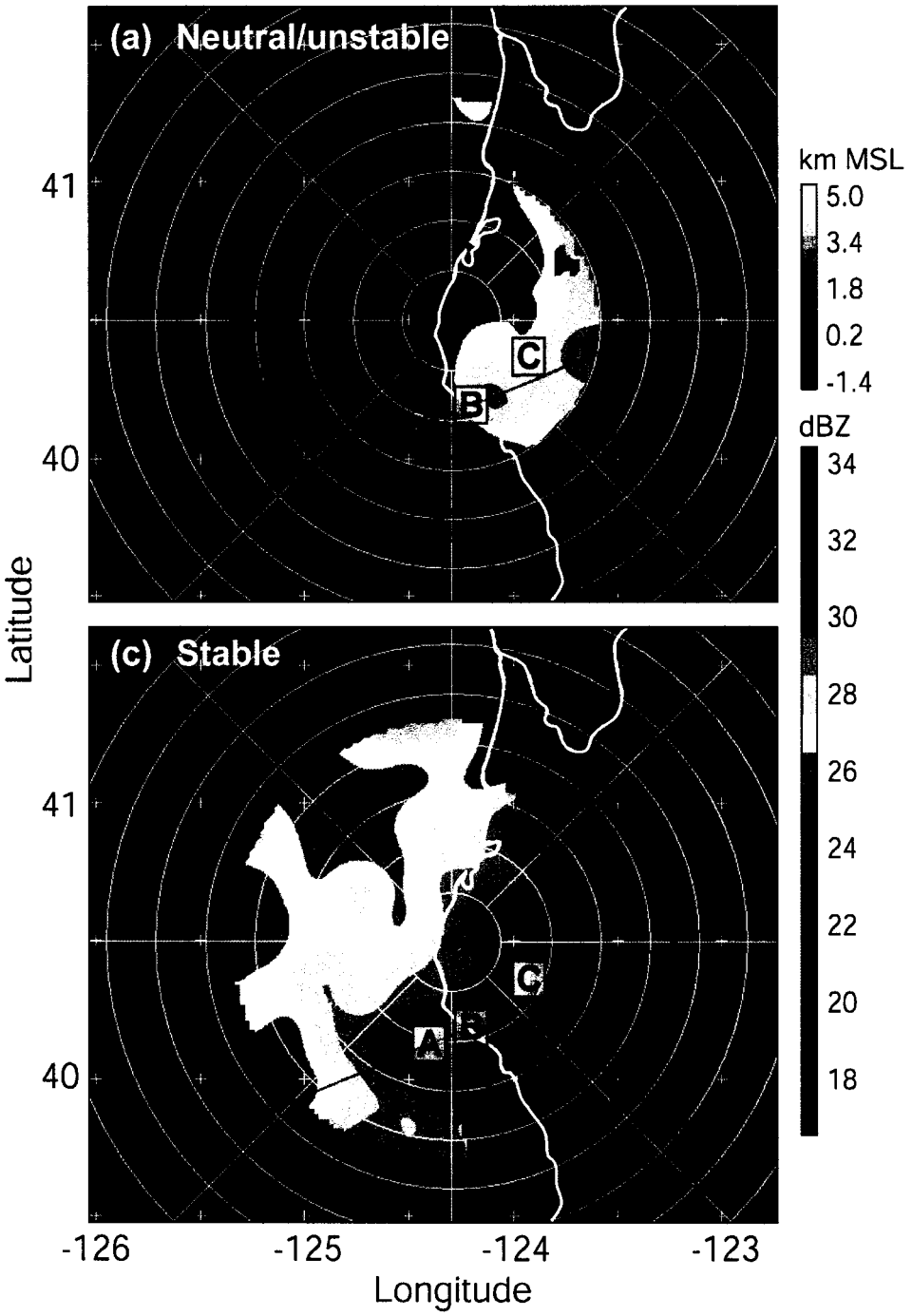

Figure 4.11. As in Fig. 4.10, except when the layer-averaged 900 – 800 mb moist Brunt-Väisälä frequency was (a) imaginary or zero, and (c) greater than zero. Respective vertical cross sections are shown in (b) and (d). Bins A – C were used to create the histograms in Fig. 4.12.

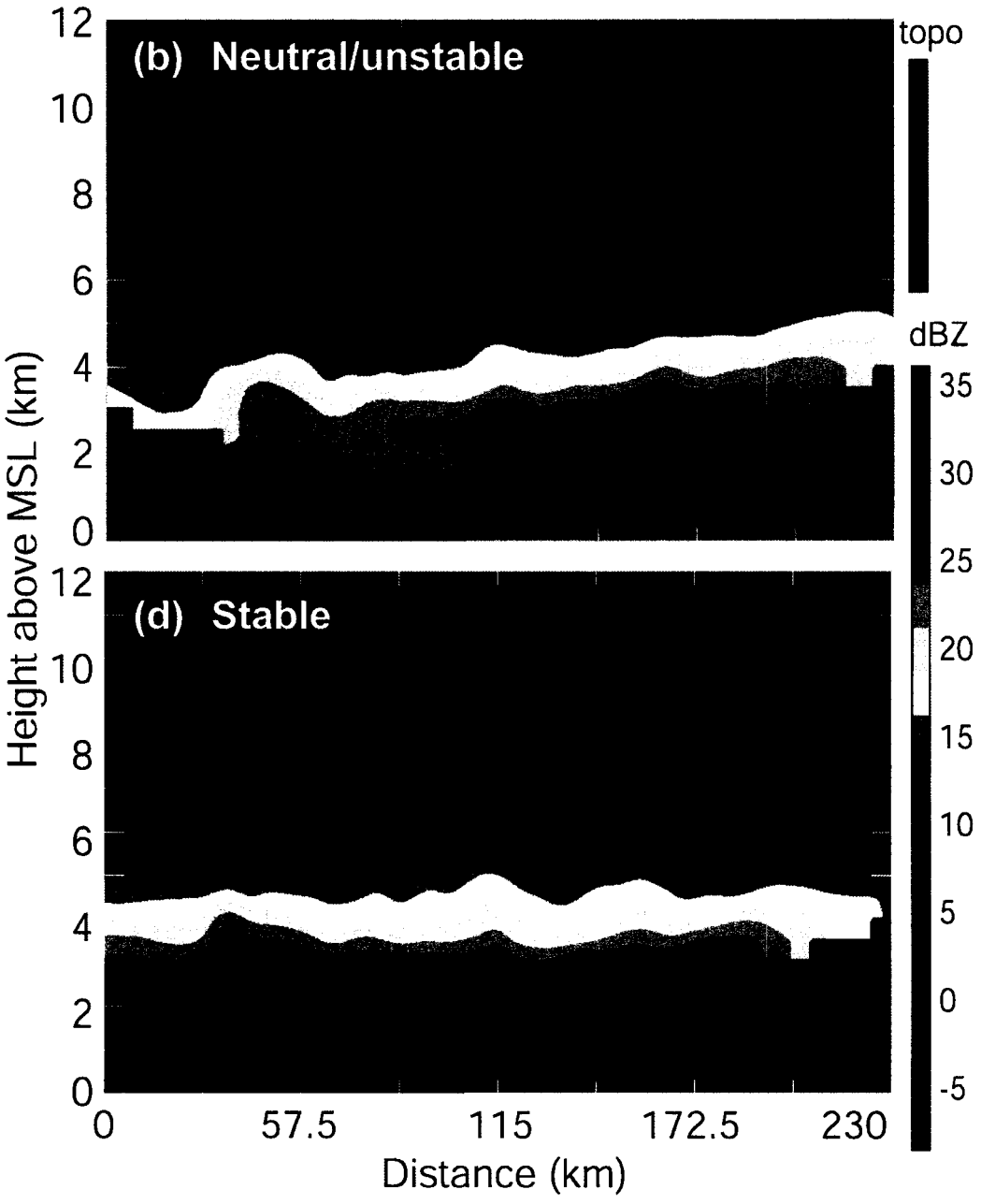

Figure 4.11. (continued)

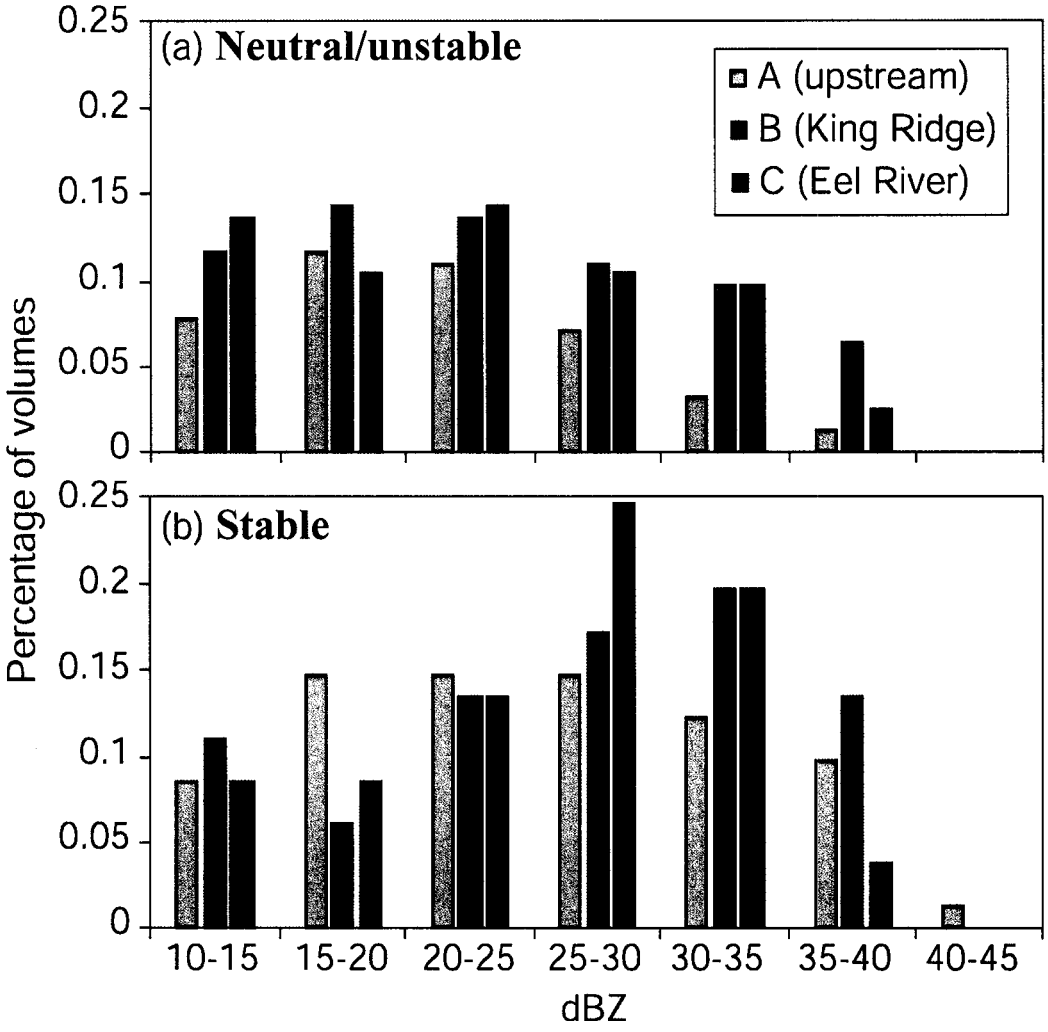

Figure 4.12. Histograms depicting the percentage of hourly radar volumes vs. mean reflectivity within bins A – C shown in Fig. 4.11 during heavy rain events when the moist Brunt-Väisälä frequency was (a) imaginary or zero, and (b) greater than zero. Bin locations were chosen as follows: (A) upstream from King Range [light gray], (B) over King Range [medium gray], and (C) downwind from King Range over the Eel River [dark gray].

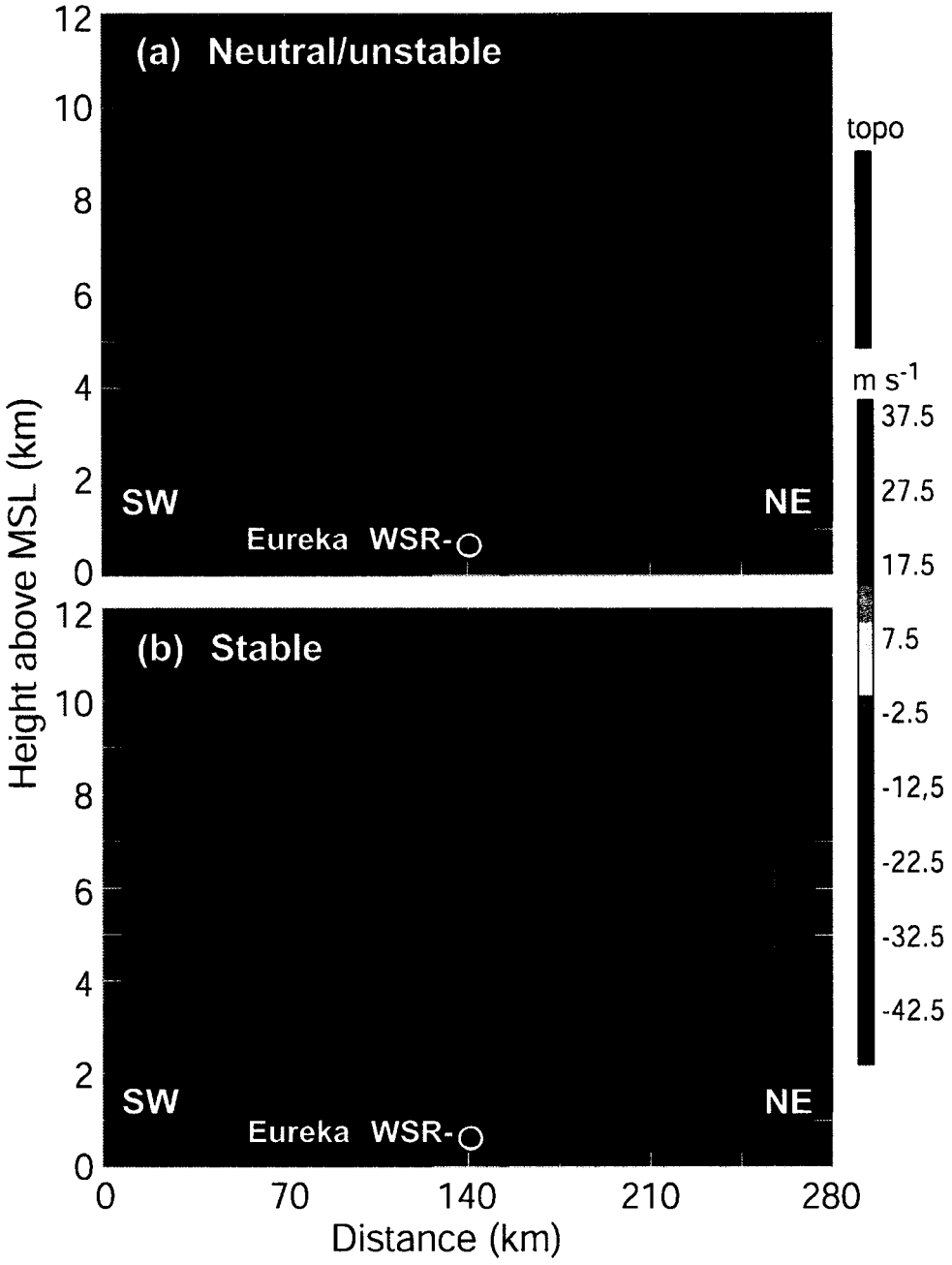

Figure 4.13. Vertical cross sections of mean hourly radial velocity [ms^{-1}] during (a) neutral/unstable and (b) stable heavy rain events (Analysis V) taken approximately parallel to the wind from 140 km southwest of the Eureka WSR-88D radar to 140 km northeast of the radar. The terrain is shaded green, and negative (positive) radial velocity indicates flow towards (away from) the radar location shown at 140-km distance and 767-m altitude (MSL).

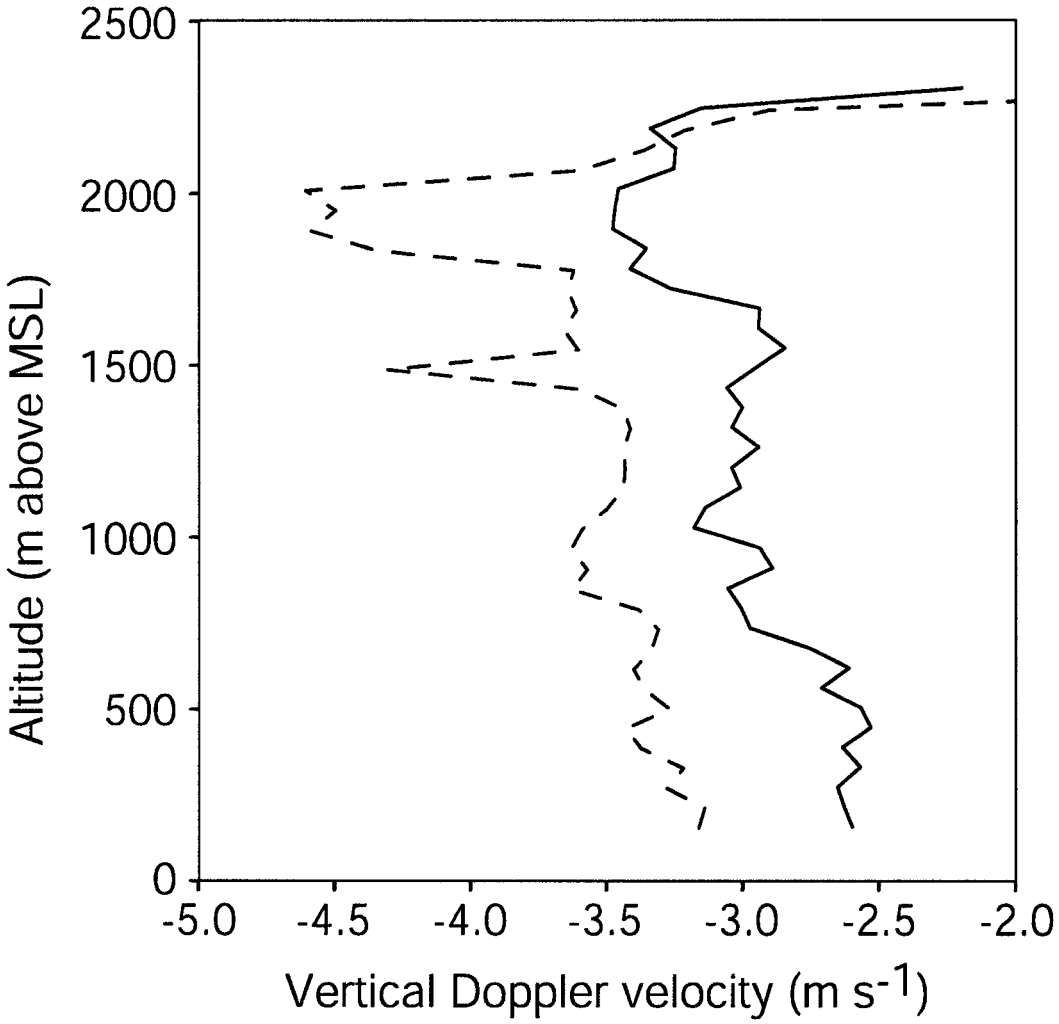

Figure 4.14. Mean ground-relative Doppler vertical velocity [ms^{-1}] obtained from a wind profiler located at Eureka, CA, amid absolutely stable (solid) and conditionally unstable or neutral (dashed) west-southwesterly flow in the 900 – 800 mb layer, during heavy rain events when the 0°C level was at least 2.5 km MSL.

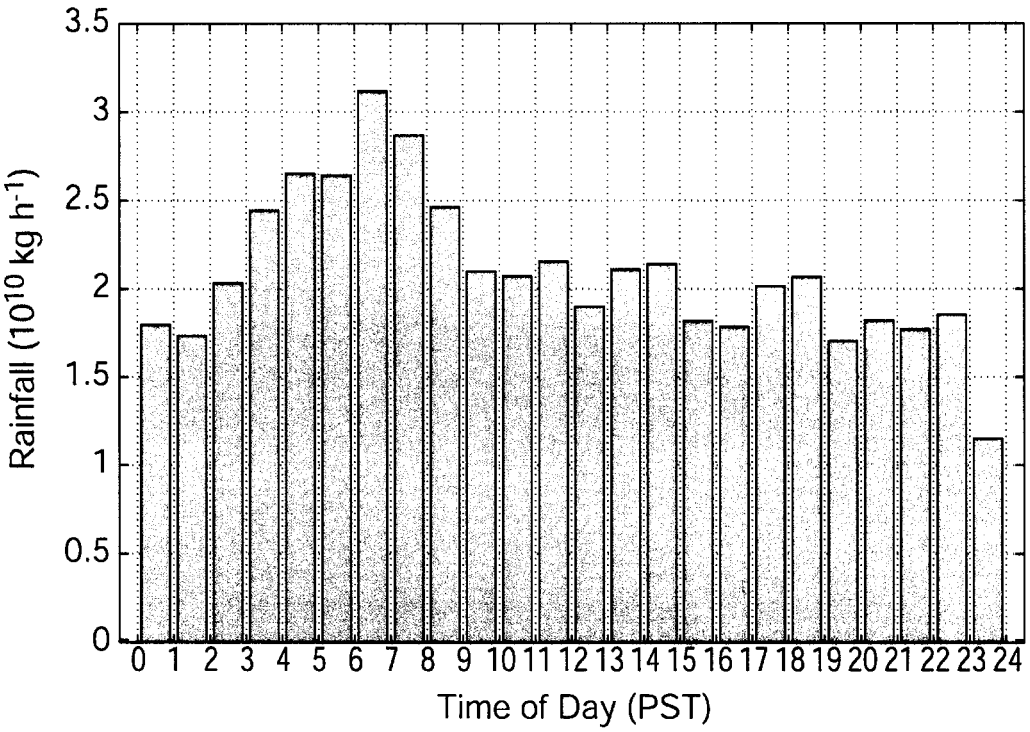

Figure 4.15. Average hourly rainfall observed over the entire radar domain of the Eureka WSR-88D at 2-km altitude (MSL) as a function of time of day during heavy rain events.

CHAPTER 5

CONCLUSIONS

5.1 Groundwork

This dissertation has laid groundwork for observational research in orographic precipitation (Ch. 2). Real-time radar data processing and three-dimensional terrain-based visualization have been achieved through the development of MountainZebra. This system makes radar data analysis more intuitive, because it enables the creation of horizontal and vertical cross-section displays of radar data and terrain in real time. This visualization technique has been used throughout Chapters 2 – 4 of this thesis and has been incorporated into other orographic precipitation studies (e.g., Medina and Houze 2003; Houze and Medina 2004). In addition, an efficient four-dimensional dealiasing (4DD) algorithm has been especially configured for unfolding turbulent radial velocity data in complex terrain at low Nyquist velocity. The 4DD scheme operated efficiently and effectively during the MAP SOP (Special Observing Period), and is now being tested operationally by NCAR in other climatic settings.

4DD and MountainZebra were deployed to MAP for real-time processing and visualization of radar data and terrain in real time. Moreover, flight track information was logged at the MAP POC (Project Operations Center), and included in the MountainZebra plots. The imagery was used to guide flight operations during MAP, and was made available to the scientific community in real time. The dis-

plays have been incorporated into MAP mission summaries. In addition, 4DD was used to prepare Monte Lema velocity data for multiple-Doppler syntheses of full-vector winds and reflectivity in real time. The achievement of real-time syntheses during MAP set the precedence for future meteorological field projects.

5.2 Comparative summary of observations

This work has revealed many similarities in the long-term fine-scale structure of orographic precipitation and airflow between the European Alps (Ch. 3) and mountains of Northern California (Ch. 4). In Europe, orographic lifting enhanced precipitation ahead of and over the windward slopes of the Alps. At finer scales, rainfall maxima occurred over the first pronounced terrain peaks on the windward side of the barrier when the flow was unblocked. In Northern California, precipitation was also enhanced over the broad windward slopes of the Coastal Range, and most strongly enhanced over the first steep terrain rise, the King Range, when the flow was unblocked. Evidence of upstream enhancement was also observed in both locations, within a Rossby radius from the barrier crest. In the California study, upstream enhancement began at a distance from the barrier crest corresponding to the Rossby radius for unsaturated air, but was more pronounced within the moist Rossby radius of the coast.

In both regimes, the strongest precipitation enhancement occurred when moist low-level airflow was directed nearly orthogonal to the terrain (south-south-westerly in northern California, south-southeasterly in the Lago Maggiore region of

the Alps). The wind turned clockwise with altitude above the boundary layer in both cases, indicating the prevalence of warm advection. In general, when the flow was stronger, the enhancement of precipitation over the windward slopes was greater. The stronger low-level flow also allowed hydrometeors to drift farther downstream before reaching the ground. In addition, stronger airflow and higher humidity at mid levels amid strong synoptic forcing strongly favors precipitation, as evidenced by the California study (Ch. 4).

These similarities between northern California and the European Alps can be generalized to other mountain climates. The greatest orographic enhancement is likely to occur when a strong flow of warm, moist air runs perpendicular to terrain. Enhancement begins upstream from a mountain barrier, intensifies over large-scale windward slopes, and maximizes over the first steep rise of the windward terrain. Orographic precipitation is therefore not always maximized over the highest terrain and is not well represented by mapping techniques that linearly regress precipitation with terrain elevation.

Coastal Northern California (Ch. 4) represents a more statically stable climatic regime, with shallower terrain than the European Alps (Ch. 3). These inherent differences explain an important distinction between the two studies. The California study investigated heavy precipitation when the airflow was strong and generally unblocked by the terrain. When the unblocked flow was *absolutely stable*, greater enhancement was observed upstream and over the windward slopes. One

possible explanation for this result is the presence of a blocked near-surface marine cold pool that lifted the overlapping unblocked flow at 900 – 800 mb. Results for the windward slopes of the Alps, however, indicate that unblocked and *conditionally unstable* airflow experienced the most enhancement. MAP field observations confirm these findings, and reveal that convective enhancement plays an important role in enhancing precipitation over the first steep terrain rise of the Alps (Socorro and Houze 2003; Yuter and Houze 2003). While shallow convective enhancement may be important to the precipitation climate of northern California, convective enhancement evidently plays a more important role in the Alps.

Nevertheless, both studies indicate that precipitation in any wind pattern, blocked or unblocked, is generally favored when the lower atmosphere is statically stable. Higher stability evidently conforms the airflow more closely to the terrain. Both studies had a pronounced diurnal pattern, with precipitation being greatest in the morning hours when the atmosphere was generally most humid and stable. For the Alps, drainage flow in deep Alpine river valleys during stable events converged with the larger-scale upslope flow over the Lago Maggiore region to enhance rainfall (Steiner et al. 2000). For California, the orographic response to static stability could have produced greater precipitation in the morning hours.

5.3 Future work

Multiple Doppler radar, polarimetric radar, and airborne observations obtained during the MAP project confirm the findings of Chapter 3 and enable con-

ceptualized microphysical explanations for orographic precipitation enhancement on the Mediterranean side of the Alps (Medina and Houze 2003; Yuter and Houze 2003; Houze and Medina 2004). However, more detailed observations are needed to confirm the results of Chapter 4 for the Northern California coast. The absence of observing systems over the Pacific Ocean warrants field research designed to better sample fine-scale low-level stability and flow responses upstream from the coast. More polarimetric radar and in-situ airborne measurements are needed to sample the microphysical processes and illuminate the growth mechanisms that produce West Coast upstream enhancement and the fine-scale enhancement over the King Range and South Fork Mountain.

Moreover, this dissertation work should be expanded to an investigation of orographic influences on deep convection. The data sets examined herein do not sample long-term patterns of deep convective rainfall over terrain. Further observational research is needed in regimes where deep convective precipitation is the norm. The techniques employed in this work could illuminate many of the roles that terrain plays in triggering, organizing, enhancing, and maintaining cumulonimbus cloud systems.

REFERENCES

Aebischer, U., and C. Schär, 1998: Low-level potential vorticity and cyclogenesis to the lee of the Alps. *J. Atmos. Sci.*, **55,** 186-207.

Alpert, P., 1986: Mesoscale indexing of the distribution of orographic precipitation over high mountains. *J. Appl. Meteorol.,* **25,** 532-545.

Austin, P. M., 1987: Relation between measured radar reflectivity and surface rainfall. *Mon. Wea. Rev.,* **115,** 1053-1070.

Banta, R. M., 1990: The role of mountain flows in making clouds. *Atmospheric Processes Over Complex Terrain,* W. Blumen, Ed., Amer. Meteor. Soc., 229-283.

Bargen, D. W., and R. C. Brown, 1980: Interactive radar velocity unfolding. *Preprints 19th Conf. on Radar Meteorology,* Miami, Amer. Meteor. Soc., 278-283.

Barnes, S. L., 1980: Report on a meeting to establish a common Doppler radar data exchange format. *Bull. Amer. Meteor. Soc.*, **61,** 1401-1404.

Bell, G. D., and L. F. Bosart, 1988: Appalachian cold air damming. *Mon. Wea. Rev.*, **116,** 137- 161.

Bergeron, T., 1968: Studies of the oreigenic effect on the areal fine structure of rainfall distribution. Meteorological Institute Uppsala Univ., Uppsala, Sweden, Report No. 6.

Bergen, W. R., and S. C. Albers, 1988: Two and three-dimensional dealiasing of Doppler radar velocities. *J. Atmos. Oceanic. Technol.,* **5,** 305-319.

Binder, P., P. Bougeault, A. Buzzi, H. C. Davies, D. Heimann, K. P. Hoinka, J. P Kuettner, D. Majewski, G. Mayr, C. Schär, R. B. Smith, R. Steinacker, H. Volkert, and C. D. Whiteman, 1995: Mesoscale Alpine Programme: Design proposal. Available upon request at MAP Data Centre, ETH Zürich, Switzerland, 65 pp.

Bougeault, P., P. Binder, A. Buzzi, R. Dirks, R. A. Houze, Jr., J. Kuettner, R. B. Smith, R. Steinacker, H. Volkert, et al., 2001: The MAP special observing period. *Bull. Amer. Meteor. Soc,* **82,** 433-462.

Bousquet, O., and B. F. Smull, 2001: Comparative study of two orographic precipitation events exhibiting significant upstream blocking during MAP. *The Mesoscale Alpine Programme Newsletter,* June, No. 15, 76-79.

Braun, S. A., R. A. Houze, Jr., and B. F. Smull, 1997: Airborne dual-Doppler observations of an intense frontal system approaching the Pacific northwest coast. *Mon. Wea. Rev.,* **125,** 3131-3156.

Browning, K. A., and R. Wexler, 1968: The determination of kinematic properties of a wind field using Doppler radar. *J. Appl. Meteor.,* **7,** 105-113.

Browning, K. A., 1979: Structure, mechanism and precipitation of orographically enhanced rain in Britain. *Global Atmos. Res. Programme,* World Meteor. Organ., Ser. No. 23, 88-114.

Browning, K. A., 1986: Conceptual models of precipitation systems. *Wea. Forecasting,* **1,** 23-41.

Buzzi, A., and A. Tibaldi, 1978: Cyclogenesis in the lee of the Alps: A case study. *Quart. J. Roy. Meteor. Soc.,* **104,** 271-287.

Buzzi, A., N. Tartaglione and P. Malguzzi, 1998: Numerical simulations of the 1994 Piedmont flood: Role of orography and moist processes. *Mon. Wea. Rev.,* **126,** 2369-2383.

Cain, D. E., and P. L. Smith, 1976: Operational adjustment of radar estimated rainfall with raingauge data: A statistical evaluation. Preprints, *17th Radar Meteorological Conf.*, Seattle, Amer. Meteor. Soc., 533-538.

Caracena, F., R. A. Maddox, L. R. Hoxit and C. F. Chappell, 1979: Mesoanalysis of the Big Thompson Storm. *Mon. Wea. Rev.*, **107,** 1-17.

Carruthers, D. J., and T. W. Choularton, 1983: A model of the feeder-seeder mechanism of orographic rain including stratification and winddrift effects. *Quart. J. Roy. Meteor. Soc.,* **109,** 575-588.

Chong, M., J.-F. Georgis, O. Bousquet, S. R. Brodzik, C. Burghart, S. Cosma, U. Germann, V. Gouget, R. A. Houze Jr., C. N. James, S. Prieur, R. Rotunno, F. Roux, J. Vivekanandan and Z.-X. Zeng, 2000: Real–time wind synthesis from Doppler-radar observations during the Mesoscale Alpine Programme. *Bulletin of the American Meteorological Society*, **81,** 12, 2953–2962.

Choularton, T. W., and S. J. Perry, 1986: A model of the orographic enhancement of snowfall by the seeder-feeder mechanism. *Quart. J. Roy. Meteor. Soc.,* **112,** 335-345.

Colle, Brian A., Clifford F. Mass, and Bradley F. Smull, 1999: An observational and numerical study of a cold front interacting with the Olympic Mountains during COAST IOP5. *Mon. Wea. Rev.*, **127,** 1310-1334.

Colle, B. A., B. F. Smull, and M.-J. Yang, 2002: Numerical simulations of a landfalling cold front observed during COAST: Rapid evolution and responsible mechanisms. *Mon. Wea. Rev.,* **130,** 1945-1966.

Corbet, J., C. Mueller, C. Burghart, K. Gould, and G. Granger, 1994: Zeb: software for integration, display, and management of diverse environmental datasets. *Bull. Amer. Meteor. Soc.,* **75,** 783-792.

Cotton, W. R., and R. A. Anthes, 1989: *Storm and Cloud Dynamics.* Academic Press, New York, 883 pp.

Crum, T. D., and R. L. Alberty, 1993: Recording, archiving, and using WSR-88D data. *Bull. Amer. Meteor. Soc.,* **74,** 645-653.

Daly, C., R. P. Neilson, and D. L. Phillips, 1994: A statistical-topographic model for mapping climatological precipitation over mountainous terrain. *J. Appl. Meteor.,* **33,** 140-158.

Davis, C. A., 1997: The modification of baroclinic waves by the Rocky Mountains. *J. Atmos. Sci.,* **54,** 848-868.

Doick, J. J., and A. R. Holt, 1995: Combined three-dimensional displays of weather radar data with terrain. Preprints, *27th Conf. on Radar Meteorology*, Vail, CO, Amer. Meteor. Soc., 371-372.

Doswell, C. A., C. Ramis, R. Romero and S. Alonso, 1998: A diagnostic study of three heavy precipitation episodes in the western Mediterranean region. *Wea. Forecasting*, **13,** 102-124.

Douglas, C. K. M. and J. Glasspoole, 1947: Meteorological conditions in heavy orographic rainfall. *Quart. J. Roy. Meteor. Soc.,* **73,** 11-38.

Doviak, R. J., and D. S. Zrnic, 1993: *Doppler Radar and Weather Observations.* 2nd ed. Academic Press, San Diego, 562 pp.

Doyle, J. D., 1997: The influence of mesoscale orography on a coastal jet and rainband. *Mon. Wea. Rev.,* **125,** 1465-1488.

Durran, D. R., and J. B. Klemp, 1982: On the effects of moisture on the Brunt-Väisälä frequency. *J. Atmos. Sci.,* **39,** 2152-2158.

Durran, D. R., 1986: Mountain waves. *Mesoscale Meteorology and Forecasting,* P. Ray, Ed., Amer. Meteor. Soc., 472-492.

Durran, D. R., 1990 : Mountain waves and downslope winds. *Atmospheric Processes over Complex Terrain* (W. Blumen, Ed.), American Meteorological Society, Boston, 59-81.

Eckland, W. L., D. A. Carter, and B. B. Balsley, 1988: A UHF wind profiler for the boundary layer: Brief description and initial results. *J. Atmos. Oceanic Technol.,* **5,** 432–441.

Eilts, M. D., and S. D. Smith, 1990: Efficient dealiasing of Doppler velocities using local environment constraints. *J. Atmos. Oceanic Technol.,* **7,** 118-128.

Elliott, R. D., and E. L. Hovind, 1964: On convection bands within Pacific Coast storms and their relation to storm structure. *J. Appl. Meteor.,* **3,** 143-154.

Ferretti, R., S. Low-Nam and R. Rotunno, 2000: Numerical simulations of the Piedmont flood of 4-6 November 1994. *Tellus*, **52A,** 162-180.

Frei, C., and C. Schär, 1998: A precipitation climatology of the Alps from high-resolution rain-gauge observations. *Int. J. Climatol.,* **18,** 873-900.

Georgis J. F., F. Roux, and P. H. Hildebrand, 2000: Observation of precipitating systems over complex orography with meteorological Doppler radars : A feasibility study. *Meteor. Atmos. Phys.,* **72,** 185-202.

Germann, U., 1999: Vertical wind profile by Doppler radars. *MAP Newsletter*, no. 11, 6-7. Available from Swiss Meteorological Institute, CH-8044 Zürich, Switzerland.

Goldreich, Y., and A. Freundlich, 1997: Rainfall anomaly over the lee side of Mount Carmel (Israel) and the associated wind field. *J. Appl. Meteor.,* **36,** 748-762.

Grossman, R. L., and D. R. Durran, 1984: Interaction of low-level flow with the western Ghat Mountains and offshore convection in the summer monsoon. *Mon. Wea. Rev.,* **112,** 652-672.

Gustavsson, T., M. Karlsson, J. Bogren, and S. Lindqvist, 1998: Development of temperature patterns during clear nights. *J. Appl. Meteor.,* **37,** 559-571.

Hennington, L., 1981: Reducing the effects of Doppler radar ambiguities. *J. Appl. Meteor.,* **20,** 1543-1546.

Henry, A. J., 1919: Increase of precipitation with altitude. *Mon. Wea. Rev.*, **47,** 33-41.

Hill, F. F., and K. A Browning, 1979: Persistence and orographic modulation of mesoscale precipitation areas in a potentially unstable warm sector. *Quart. J. Roy. Meteor. Soc.,* **105,** 57-70.

Hobbs, P. V., R. C. Easter and A. B. Fraser, 1973: A theoretical study of the flow of air and fallout of solid precipitation over mountainous terrain. Part II: Microphysics. *J. Atmos. Sci.*, **30,** 813-823.

Hobbs, P. V., 1975: The nature of winter clouds and precipitation in the Cascade Mountains and their modification by artificial seeding. Part I: Natural conditions. *J. Appl. Meteor.*, **14,** 783-804.

Hobbs, P. V., R. A. Houze, Jr., and T. J. Matejka, 1975: Dynamical and microphysical structure of an occluded frontal system and its modification by orography. *J. Atmos. Sci.*, **32,** 1542-1562.

Hobbs, P. V., T. J. Matejka, P. H. Herzegh, J. D. Locatelli, and R. A. Houze Jr., 1980: The mesoscale and microscale structure and organization of clouds and precipitation in midlatitude cyclones. I: A case study of a cold front. *J. Atmos. Sci.,* **37,** 568–596.

Holmboe, J., and H. Klieforth, 1957: Investigations of mountain lee waves and air flow over the Sierra Nevada. Final report, Contract AF 19 (604-728), 290 pp. [Tech Rep. 57, AF Cambridge Rese. Center, 204 pp.]

Houze, R. A., Jr., J. D. Locatelli, and P. V. Hobbs, 1976: Dynamics and cloud microphysics of the rainbands in an occluded frontal system. *J. Atmos. Sci.,* **33,** 1921-1936.

Houze, R. A., Jr., 1993: *Clouds Dynamics*. Academic Press, 573 pp.

Houze, R. A., Jr., J. Kuettner and R. B. Smith, 1998: Mesoscale Alpine Programme. U.S. overview document and experiment design. 101 pp. [Available from MAP U.S. Project Office, UCAR/JOSS, P.O. Box 3000, Boulder, CO 80307-3000.]

Houze, R. A., Jr., S. Medina and M. Steiner, 2000: Two cases of heavy rain on the Mediterranean side of the Alps in MAP. Preprints, *Ninth Conference on Mountain Meteorology*, Aspen, CO, Amer. Meteor. Soc., 1-5.

Houze, R. A., Jr., C. N. James, and S. Medina, 2001: Radar observations of precipitation and airflow on the Mediterranean side of the Alps: Autumn 1998 and 1999. *Quart. J. Roy. Meteor. Soc.,* **127,** 2537-2558.

Houze, R. A., Jr., S. Medina, and S. E. Yuter, 2001a: Orographic precipitation mechanisms: New data from the Mesoscale Alpine Programme. Preprints, *International Conference on Mesoscale Meteorology and Typhoons in East Asia*, Taipei, Taiwan, 26-28 September, 88-93.

Houze, R. A., and S. Medina, 2001: Alpine Precipitation Mechanisms in MAP IOP2b and 8. MAP Conf., Schliersee, Germany.

Houze, R. A., Jr., S. Brodzik, C. Schumacher, S. E. Yuter, and C. R. Williams, 2004: Uncertainties in oceanic radar rain maps at Kwajalein and implications for satellite validation. *J. Appl. Meteor.*, conditionally accepted.

Houze, R. A., Jr., and S. Medina, 2004: Turbulence as a mechanism for orographic precipitation enhancement. *J. Atmos. Sci.*, submitted.

James, C. N., S. R. Brodzik, H. Edmon, R. A. Houze, Jr. and S. E. Yuter, 2000: Radar data processing and visualization over complex terrain. *Wea. Forecasting,* **15,** 327-338.

James, C. N., and R. A. Houze, Jr., 2001: A real-time four-dimensional Doppler dealiasing scheme. *J. Atmos. Oceanic Technol.,* **18,** 1674-1683.

James, C. N., and R. A. Houze, Jr., 2004: Radar observations of precipitation enhancement by the coastal terrain of Northern California: October 1995 – March 1998. *Mon. Wea. Rev.*, in preparation.

Jing, Z., and G. Wiener, 1993: Two-dimensional dealiasing of Doppler velocities. *J. Atmos. Oceanic Technol.,* **10,** 798-808.

Joss, J., and L. Lee, 1995: The application of radar-gauge comparisons to operational precipitation profile corrections. *J. Appl. Meteor.,* **34,** 2612-2630.

Joss, J., B. Schädler, G. Galli, R. Cavalli, M. Boscacci, E. Held, G. D. Bruna, G. Kappenberger, V. Nespor, and R. Spiess, 1998: *Operational Use of Radar for Precipitation Measurements in Switzerland.* Final report, NRP 31, ETH Zürich, Switzerland, 108 pp.

Joss, J., and A. Waldvogel, 1990: Precipitation measurements and hydrology. *Radar in Meteorology*, Battan Memorial and 40th Anniversary Radar Meteorology Conference, (D. Atlas, Ed.), Amer. Meteor. Soc., 577-606.

Kappenberger, G., and J. Kerkmann, 1997: *Il Tempo in Montagna.* Zanichelli Editore S.p.A., Bologna, Italy, 255 pp.

Lilly, D. K., and D. R. Durran, 1983: Stably stratified moist airflow over mountainous terrain. *Proc. Sino-Am. Workshop Mountain Meteorol., 1st, 1982, Beijing* (E. R. Reiter, Z. Baozhen, and Q. Yongfu, Eds.), Science Press, Beijing and Am. Meteorol. Soc., Boston, pp. 569-608.

Lin, C. C., and J. P. Reilly, 1997: A site-specific model of radar terrain backscatter and shadowing. *Johns Hopkins APL Technical Digest*, **18,** 432-447.

Lionetti, M., 1996: The Italian floods of 4-6 November 1994. *Weather,* **1,** 18-27.

Longley, R. W., 1975: Precipitation in valleys. *Weather,* **30,** 294-300.

Majewski, D., 1991: The Europa-Modell of the Deutscher Wetterdienst. *Proc. ECMWF Seminar on Numerical Methods in Atmospheric Models,* Reading, England, European Centre for Medium-Range Weather Forecasts, Vol. 2, 147-191.

Marshall, J. S., and W. M. Palmer, 1948: The distribution of raindrops with size. *J. Meteor.*, **5,** 165-166.

Mass, C., 1981: Topographically forced convergence in western Washington State. *Mon. Wea. Rev.,* **109,** 1335-1347.

Mass, C. F., and G. K. Ferber, 1990: Surface pressure perturbations produced by an isolated mesoscale topographic barrier. Part I: General characteristics and dynamics. *Mon. Wea. Rev.*, **118,** 2579-2596.

McGinley, J., 1982: A diagnosis of Alpine lee cyclogenesis. *Mon. Wea. Rev.*, **110,** 1271-1287.

Medina, S., and R. A. Houze, Jr., 2003: Air motions and precipitation growth in Alpine storms. *Quart. J. Roy. Meteor. Soc.*, special MAP issue, **129**, 345-371.

Merritt, M. W., 1984: Automatic velocity dealiasing for real-time applications. *Proc. 22nd Conf. on Radar Meteorology,* Zürich, Amer. Meteor. Soc., 528-533.

Mohr, C. G., and R. L. Vaughan, 1979: An economical procedure for Cartesian interpolation and display of reflectivity factor data in three-dimensional space. *J. Appl. Meteor.,* **18,** 661-670.

Nagle, R. E., and S. M. Serebreny, 1962: Radar precipitation echo and satellite cloud observations of a maritime cyclone. *J. Appl.. Meteor.,* **1,** 279-295.

Neiman, P. J., F. M. Ralph, A. B. White, D. E. Kingsmill, and P. O. G. Persson, 2002: The statistical relationship between upslope flow and rainfall in California's coastal mountains: Observations during CALJET. *Mon. Wea. Rev.,* **130,** 1468-1492.

Neiman, P. J., P. O. G. Persson, F. M. Ralph, D. P. Jorgensen, A. B. White, and D. E. Kingsmill, 2004: Modification of fronts and precipitation by coastal blocking during an intense landfalling winter storm in Southern California: Observations during CALJET. *Mon. Wea. Rev.,* **132,** 242-273.

Parsons, D. B., and P. V. Hobbs, 1983: The mesoscale and microscale structure and organization of clouds and precipitation in midlatitude cyclones. IX: Some effects on orography and rainbands. *J. Atmos. Sci.,* **40,** 1930-1949.

Queney, P., 1948: The problem of airflow over mountains: A summary of theoretical results. *Bull. Amer. Meteor. Soc.,* **29,** 19-26.

Ralph, F. M., and Coauthors, 1999: The California Land-Falling Jets Experiment (CALJET): Objectives and design of a coastal atmosphere-ocean observing system deployed during a strong El Niño. Preprints, Third Symp. on Integrated Observing Systems, Dallas, TX, Amer. Meteor. Soc., 78-81.

Ralph, F. M., P. J. Neiman, D. E. Kingsmill, P. O. G. Persson, A. B. White, E. T. Strem, E. D. Andrews, and R. C. Antweiler, 2003: The impact of a prominent rain shadow on flooding in California's Santa Cruz Mountains: A CALJET case study and sensitivity to the ENSO Cycle. *J. of Hydrometeor.*, **4,** 1243–1264.

Ralph, F. M., P. J. Neiman, and G. A. Wick, 2004: Satellite and CALJET aircraft observations of atmospheric rivers over the eastern North Pacific Ocean during the winter of 1997/98. *Mon. Wea. Rev.,* accepted.

Ray, P., and Ziegler, C., 1977: Dealiasing first moment Doppler estimates. *J. Appl. Meteor.,* **16,** 563-564.

Reed, R. J., and E. E. Recker, 1971: Structure and properties of synoptic-scale wave disturbances in the equatorial western Pacific. *J. Atmos. Sci.,* **28,** 1117-1133.

Rhue, D. T., and M. H. Jain, 1995: A RISC-based WSR-88D interface and workstation. Preprints, *11th Intl. Conf. on Interactive Info. and Processing Systems for Meteorology, Oceanography, and Hydrology*, Dallas, Texas, Amer. Meteor. Soc., 235-239.

Richard, E., N. Chaumerliac, J. F. Mahfouf, and E. C. Nickerson, 1987: Numerical simulation of orographic enhancement of rain with a mesoscale model. *J. of Appl. Meteor.*, **26,** 661–669.

Rotunno, R., and R. Ferretti, 2001: Mechanisms of intense alpine rainfall. *J. Atmos. Sci.*, **58,** 1732-1749.

Schär, C., and D. R. Durran, 1997: Vortex formation and vortex shedding in continuously stratified flows past isolated topography. *J. Atmos. Sci.,* **54,** 534-554.

Shepard, D. S., 1984: Computer mapping: The SYMAP interpolation algorithm. *Spatial Statistics and Models* (Gaile, G. L. and Willmott, C. J., Eds.), Dordrecht, pp. 133-145.

Sinclair, M. R., D. S. Wratt, R. D. Henderson, and W. R. Gray, 1997: Factors affecting the distribution and spillover of precipitation in the southern Alps of New Zealand: A case study. *J. Appl. Meteor.,* **36,** 428-442.

Skamarock, W. C., M. L. Weisman, and J. B. Klemp, 1994: Three-dimensional evolution of simulated long-lived squall lines. *J. Atmos. Sci.,* **51,** 2563-2584.

Smith, R. B., 1979: The influence of mountains on the atmosphere. *Adv. Geophys.*, **21,** 87-230.

Smith, R. B., 1982: A differential advection model of orographic rain. *Mon. Wea. Rev.*, **110,** 306-309.

Spiegel, M. R., 1972: *Schaum's Outline of Theory and Problems of Statistics.* McGraw-Hill, 359 pp.

Steiner, M., J. A. Smith, B. F. Smull and R. A. Houze, Jr., 2000: Airflow within major river valleys on the south side of the Alps as observed during the MAP special observing period. Preprints, *Ninth Conference on Mountain Meteorology*, Aspen, CO, Amer. Meteor. Soc., 11-14.

Tibaldi, S., A. Buzzi, and A. Speranza, 1990: Orographic cyclogenesis. *Extratropical Cyclones,* (Newton, C., and E. O. Holopainen, Eds.), Amer. Meteor. Soc., Boston, 107-128.

Tripoli, G. J., and W. R. Cotton, 1989: Numerical study of an observed orogenic mesoscale convective system. Part I: simulated genesis and comparison with observations. *Mon. Wea. Rev.*, **117,** 273-304.

Westrick, K. J., C. F. Mass, and B. A. Colle, 1999: The limitations of the WSR-88D radar network for quantitative precipitation measurement over the coastal western United States. *Bull. Amer. Meteor. Soc.*, **80,** 2289-2298.

White, A. B., P. J. Neiman, F. M. Ralph, D. E. Kingsmill, and P. O. G. Persson, 2003: Coastal orographic rainfall processes observed by radar during the California Land-Falling Jets Experiment. *J. Hydrometeor.*, **4,** 264-282.

Whiteman, C. D., 1990: Observations of thermally developed wind systems in mountainous terrain. *Atmospheric Processes Over Complex Terrain,* W. Blumen, Ed., Amer. Meteor. Soc., 5-42.

Wilks, D. S., 1995: *Statistical Methods in the Atmospheric Sciences.* Academic Press, London, 467 pp.

Wilson, J., R. Carbone, H. Baynton, and R. Serafin, 1980: Operational application of meteorological Doppler radar. *Bull. Amer. Meteor. Soc.*, **61,** 1154-1168.

Yamada, Y., and M. Chong, 1999: VAD-based determination of the Nyquist interval number of Doppler velocity aliasing without wind information. *J. Meteor. Soc. Japan,* **77,** 447-457.

Yu, C.-K., and B. F. Smull, 2000: Airborne observations of a land-falling cold front upstream of steep coastal orography. *Mon. Wea. Rev.,* **128,** 1577-1603.

Yuter, S. E., and R. A. Houze, Jr., 2003: Microphysical modes of precipitation growth determined by S-band vertically pointing radar in orographic precipitation during MAP. *Quart. J. Roy. Meteor. Soc.*, special MAP issue, **129**, 455-476.

APPENDIX: CALCULATIONS PERFORMED ON RADAR DATA[10]

It has been shown that sampling over long time periods, such as the studies in this dissertation, greatly reduces the large uncertainties in radar reflectivity and rainfall estimates by removing the scatter of individual measurements (Joss and Waldvogel 1990; Cain and Smith 1976). However, temporal averaging may not cancel out long-term biases in calibration. For example, during the 2.5-yr period that the Eureka WSR-88D volumes were archived (Ch. 4), the reflectivity calibration offset could have approached an estimated 3 dBZ and affected the accuracy of the results. Nevertheless, exact quantitative estimates of reflectivity or precipitation rate are not required. Rather, it is the variability of the values in time, in space, and by meteorological epoch that are the focus of this work. Moreover, because the statistical analyses in this thesis incorporate volumes from throughout the long-term radar archives, qualitative differences between the various figures should not strongly reflect variations in radar calibration.

The mean reflectivity and radial velocity over all hourly volumes in an archive is obtained by simply averaging those fields at each grid point. Higher reflectivity is generally correlated with heavier rainfall, and in some of the horizontal figures rainfall rate was estimated using the Marshall and Palmer (1948) *Z-R* relation:

$$Z = 200R^{1.6} \qquad \text{(A1)}$$

[10] This section is adapted from Houze et al. (2001) and James and Houze (2004)

where Z is the equivalent reflectivity in $mm^6 m^{-3}$ and R is the rainfall rate in $mm\ h^{-1}$. Vertical cross sections are displayed in reflectivity units since rain rate has no meaning above the 0°C level. It is assumed that missing reflectivity indicates that no precipitation is occurring, whereas a similar assumption could not be made with missing radial velocity gates. Therefore, the mean reflectivity $\overline{Z}$, rain rate $\overline{R}$ and radial velocity $\bar{v}$ were computed as:

$$\overline{Z} = \frac{\sum_{i}^{N} Z_i}{N} \tag{A2}$$

$$\overline{R} = \frac{\sum_{i}^{N} R_i}{N} \tag{A3}$$

$$\bar{v} = \frac{\sum_{j}^{n} Z_j}{n} \tag{A4}$$

where N is the total number of volumes, and n ($\leq N$) is the number of volumes with available radial velocity values at the grid point in question. From (A2) and (A3), it is evident that maxima in the mean reflectivity and rain rate indicate regions where the precipitation was either more frequent, more intense or both. To remove some of this ambiguity, a third field called the precipitation frequency was calculated and defined as the percentage of the total volumes in which reflectivity $\geq$ 13 dBZ (~0.16 $mm\ h^{-1}$) was observed at each grid point.

In order to investigate the sensitivity of radial velocity or precipitation to a given variable, superposed epoch analyses (e.g. Reed and Recker 1971) or "composites" were performed. This analysis extracted all volumes from the archives whose time stamps (beginning time of data recorded in a volume) corresponded to *epochs*, defined by some specified condition. Then, the mean rainfall rate, reflectivity, radial velocity and standard deviations were computed at each grid point in the sample of extracted volumes.

To create some of the analyses in Chapter 3, the Student's t difference-of-means test was applied at each grid point to indicate the statistical significance of the sample mean over a given time period or epoch. An *a priori* confidence level of 95% rejects the null hypothesis that the sample mean at a given grid point did not differ significantly from the larger mean. Two-sided difference of means tests use the expression,

$$t = \frac{\bar{x}_1 - \bar{x}_2}{\sqrt{\left(\frac{1}{N_1} + \frac{1}{N_2}\right)\left(\frac{N_1 s_1^2 + N_2 s_2^2}{N_1 + N_2 - 2}\right)}} \qquad \text{(A5)}$$

(Spiegel 1972), where $\bar{x}_1, s_1$ and N_1 are the mean, standard deviation and number of volumes in the sample, and $\bar{x}_2, s_2$ and N_2 are the seasonal mean, standard deviation and total number of volumes in the archive. The null hypothesis is rejected in regions where $|t| > 1.96$, corresponding to a 95% confidence level.

The difference-of-means test requires that the volumes in the archive be mutually independent (Wilks 1995). To reduce the statistical dependence between radar samples, a 1-h time interval between successive volume scans was used. The 1-h time lag reduced the volume-to-volume autocorrelation at each gridpoint to an average of 0.3, with local autocorrelation minima less than 0.1 over the lower terrain and local maxima up to 0.6 in areas where persistent orographic uplift was observed. Because the autocorrelation was higher over the higher terrain, the difference-of-means statistics in these areas may have been quantitatively exaggerated in those regions. In addition, precipitation is a highly skewed quantity; however, the difference-of-means test does not require a Gaussian distribution as long as the sample sizes in all of the analyses are sufficiently large (Wilks 1995). The sample sizes in this work are large enough to meet this condition.

VITA

Curtis Neal James

Education

1995 B.S. with honors, University of Arizona
Major: Atmospheric Science, Minor: Physics/Mathematics

2004 Ph.D., University of Washington
Atmospheric Sciences

Professional Employment

1993-95 Meteorological Technician, National Weather Service, Tucson, AZ

1995-99 Research Assistant/Teaching Assistant/Lead Teaching Assistant, Atmospheric Sciences Department, University of Washington, Seattle, WA

Present Affiliation

Assistant Professor (2000 – present)
Meteorology Department
Embry-Riddle Aeronautical University
Address: 3700 Willow Creek Rd.
Prescott, AZ 86301-3720
E-mail: Curtis.James@erau.edu
Phone: 928-777-6655

Field Program Experience

1999 MAP (Mesoscale Alpine Programme), European Alps, radar scientist and algorithm developer

Awards

1994	American Meteorological Society Dr. Pedro Grau Scholarship
1995	Outstanding Senior Award, Atmospheric Sciences, University of Arizona
2002	Outstanding Faculty Award, College of Aviation, Embry-Riddle Aeronautical University
2002&04	Who's Who Among America's Teachers

Publications

James, C., S. Brodzik, H. Edmon, R. A. Houze, Jr., and S. E. Yuter, 1999: MountainZebra: Real-time archival and 4-D visualization of radar volumes over complex terrain. Preprints, *COST-75 Final International Seminar on "Advanced Weather Radar Systems,"* Locarno, Switzerland, 297-306.

Chong, M., J.-F. Georgis, O. Bousquet, S. R. Brodzik, C. Burghart, S. Cosma, U. Germann, V. Gouget, R. A. Houze, Jr., C. N. James, S. Prieur, R. Rotunno, F. Roux, J. Vivekanandan, and Z.-X. Zeng, 2000: Real-time wind synthesis from Doppler radar observations during the Mesoscale Alpine Programme. *Bull. Amer. Meteor. Soc.,* **81,** 2953-2962.

James, C. N., S. R. Brodzik, H. Edmon, R. A. Houze, Jr., and S. E. Yuter, 2000: Radar data processing and visualization over complex terrain. *Wea. Forecasting,* **15,** 327-338.

Houze, R. A., Jr., C. N. James, and S. Medina, 2001: Radar observations of precipitation and airflow on the Mediterranean side of the Alps: Autumn 1998 and 1999. *Quart. J. Roy. Meteor. Soc.,* **127,** 2537-2558.

James, C. N., and R. A. Houze, Jr., 2001: A real-time four-dimensional Doppler dealiasing scheme. *J. Atmos. Oceanic Technol.,* **18,** 1674-1683.

James, C. N., and R. A. Houze, Jr., 2004: Radar observations of precipitation enhancement by the coastal terrain of Northern California: October 1995 – March 1998. *Mon. Wea. Rev.*, in preparation.